Self-Potential and electromagnetic monitoring during fluid injection into magmatic rocks

Doctoral Thesis

submitted by Nadine Vanessa Haaf

A thesis submitted in fulfillment of the requirements
for the degree of Dr. rer nat
at the
Department of Material and Earth Sciences
Technische Universität Darmstadt
Darmstadt 2022

TECHNISCHE
UNIVERSITÄT
DARMSTADT

Supervisor Prof. Dr. Eva Schill
Co-supervisor Prof. Dr. Ingo Sass

Date of submission: November 9, 2021
Date of oral examination: March 4, 2022

Haaf, Nadine: Self-Potential and electromagnetic monitoring during fluid injection into magmatic rocks
Darmstadt, Technische Universität Darmstadt
Year thesis published in TUprints: 2022
Date of viva voce: 04.03.2022

Board of examiners

Head:	Prof. Dr. Christoph Schüth
Supervisor:	Prof. Dr. Eva Schill
Co-supervisor:	Prof Dr. Ingo Sass
Examiner:	Prof. Dr. Andreas Henk
Examiner	Prof. Dr. Guy Marquis

Declaration of Authorship

I hereby declare that the presented dissertation is based on original research and is the result of my own work. I certify that this dissertation contains no material which has been accepted for the award of any other degree in my name, in any university or other tertiary institution and, to the best of my knowledge and belief, contains no material previously published or written by another person, except where due reference has been made in the text.

Signed:

Date:

"Nothing in life is to be forced, it is only to be understood. Now is the time to understand more, so that we may fear less."

Marie Curie

Kurzfassung

Auch heute noch stellt die induzierte Seismizität eine große Herausforderung bei der massiven hydraulischen Stimulation in der Geothermie dar. Es gibt verschiedene Ansätze, um damit umzugehen: z. B. angepasste Ampelsysteme für die Echtzeitüberwachung der hydraulischen Parameter und der induzierten Seismizität oder die Erprobung neuer Injektionsprotokolle wie z. B. Fatigue Hydraulic Fracturing. Durch die Verringerung der Stärke und Anzahl seismischer Ereignisse wird das seismische Signal abgeschwächt, was wiederum die seismische Überwachung selbst beeinträchtigt. Daher sind neue Überwachungstechniken von großem Interesse. Jüngste Studien haben gezeigt, dass elektrische und elektromagnetische Überwachungsmessungen im Zusammenhang mit hydraulischen Injektionsversuchen erfolgreich eingesetzt werden können.

Diese Arbeit enthält Datensätze von zwei verschiedenen Injektionsversuchen auf der Reservoir- und der Meterskala, um mögliche elektrokinetische oder seismoelektrische Effekte zu untersuchen und die Beobachtungen aus anderen Injektionsversuchen, wie z. B. Rittershoffen, zu reproduzieren. Die Experimente auf der Reservoirskala wurden elektromagnetisch mit magnetotellurischen (MT) Daten überwacht. Die Ergebnisse dieser Studie zeigen einen zeitlichen Zusammenhang zwischen abnehmendem scheinbaren Widerstand in den Periodenbereichen von 0.15 - 1 s und 4 - 8 s und (i) der Aktivität des geomagnetischen Feldes, (ii) den Flüssigkeitsverlusten bis zu 60 L/s sowie (iii) mechanischen Prozessen, die vor Clustern der induzierten Seismizität auftreten. Vor diesem Hintergrund bleibt die volle physikalische Bedeutung der scheinbaren Widerstandsänderungen eine Frage der Debatte. Es sei darauf hingewiesen, dass die Vorwärtsmodellierung der Auswirkungen des injizierten Wasservolumens die beobachteten Widerstandsänderungen nicht erklären konnte.

Bei den Experimenten zum Hydraulic Fracturing (HF) im unterirdischen Labormaßstab, HF2 (konventionell) und HF3 (Fatigue Hydraulic Fracturing), wurden das Eigenpotential (SP) und die elektromagnetische Strahlung (EMR) eingesetzt. Änderungen des SP wurden bei beiden Experimenten mit einer zeitlichen Verzögerung in den Nahfeldsensoren (etwa 50 - 70 m Abstand vom Experiment) beobachtet. In den Fernfeldsensoren (etwa 150 - 200 m vom Experiment entfernt) werden solche Veränderungen jedoch nur während des HF2-Experiments beobachtet. Außerdem wird das Hintergrundsignal etwa 45 Minuten nach der letzten Druckentlastung erreicht. Im Allgemeinen sind die Minima und Maxima, die sich aus den unterschiedlichen Elektrodenabständen zwischen den einzelnen Injektionsschritten ergeben, in Phase. Im Gegensatz dazu sind nach Abschluss der beiden Experimente HF2 und HF3 die größten Minima und Maxima durch eine deutliche Phasenverschiebung gekennzeichnet. Darüber hinaus zeigen die Ergebnisse während der Shut-in-Phasen eine inverse Korrelation zwischen Druckabfall und steigenden EMR-Amplituden während HF2 und HF3.

Zusammenfassend kann gesagt werden, dass die Ziele dieser Arbeit erreicht wurden, indem (i) ein neuer MT-Datensatz für die Fluidinjektion in eine andere Gesteinsart, nämlich Basalt, bereitgestellt wurde, (ii) die Skalenlücke zwischen SP- und elektromagnetischen (EM) Datensätzen durch die

Überwachung von Injektionstests auf der Meterskala geschlossen wurde und (iii) Vorläufer seismischer Ereignisse unter kontrollierbaren Bedingungen angezeigt wurden. Es bleiben jedoch noch einige Fragen offen, z. B. ob die Beobachtungen der Vorläufer in anderen Experimenten und im unterirdischen Labormaßstab verifiziert werden können. Und nicht zuletzt, ob die vermutete Verbindung zwischen Druck und EM- oder SP-Signal mit dem Flüssigkeitsfluss in den Mikrofrakturen oder nur mit dem Druck zusammenhängt.

Abstract

Still today, induced seismicity is a major challenge during massive hydraulic stimulation in geothermal energy. Several approaches have been made to deal with it: e.g., adapted traffic light systems for real-time monitoring of hydraulic parameters and induced seismicity or testing new injection protocols such as fatigue hydraulic fracturing. In reducing the magnitudes and number of seismic events, the seismic signal is weakened, affecting the seismic monitoring itself again. Therefore, new monitoring techniques are of major interest. Recent studies showed the successful application of electric and electromagnetic monitoring surveys in the context of hydraulic injection experiments.

This thesis includes data sets from two different injection experiments at the reservoir- and the mine-scale to investigate possible electrokinetic or seismoelectric effects and to reproduce the observations from other injection experiments, such as Rittershoffen. The experiments at reservoir-scale were electromagnetically monitored using magnetotelluric (MT) data. The results of this study show a temporal relation between decreasing apparent resistivity in the period ranges of 0.15-1 s and 4-8 s and (i) the geomagnetic field activity, (ii) the fluid losses up to 60 L/s, as well as (iii) mechanic processes occurring before induced seismicity. Against this background, the full physical meaning of the apparent resistivity changes remains a matter of debate. Note that forward modeling of the effect of the injected water volume could not explain the observed resistivity changes.

Hydraulic fracturing (HF) experiments at underground lab scale, HF2 (conventional) and HF3 (fatigue hydraulic fracturing), were self-potential (SP) and electromagnetic radiation (EMR) monitored. Changes in SP have been observed with a temporal delay in both experiments in the near-field sensors (about 50 - 70 m distance from the experiment). However, in the far-field sensors (about 150 - 200 m from the experiment), such changes are observed only during the HF2 experiment. Furthermore, the background signal is reached about 45 minutes after the last pressure release. Generally, minima and maxima obtained from different electrode offsets between the individual injection steps are in phase. In contrast, after completing the two experiments, HF2 and HF3, the major minima and maxima are characterized by a significant phase shift. In addition, during shut-in phases, the results show an inverse correlation between pressure drop and increasing EMR amplitudes during HF2 and HF3.

In conclusion, the objectives of this thesis have been achieved by (i) providing a new magnetotelluric monitoring data set of fluid injection in a different rock type, i.e., basalt, (ii) filling the scale-gap of SP and electromagnetic (EM) data sets by monitoring underground-lab scale injection tests, and (iii) indicating precursor of seismic events under controllable condition. However, some open questions remain, such as if the precursor observations are verified in other experiments and on underground lab- or lab-scale. And last but not least, is the supposed link between pressure and EM or SP signal linked to fluid flow on micro-fractures or only to pressure.

Acknowledgements

This dissertation would not have been possible without the support of many people, whom I would like to thank at this point. My special thanks go to:

- Prof. Dr. Eva Schill, my first supervisor to have the chance to do my Ph.D. in Karlsruhe and Darmstadt. Her motivation and support helped me go through every difficulty in the research; giving me the opportunity to do lots of fieldwork in Iceland, France, and Mexico.
- Prof. Dr. Ingo Sass, my second supervisor, for giving me feedback and helpful ideas throughout my Ph.D.
- the GFZ especially PD Dr. Arno Zang for organizing the hydraulic fracturing experiments in the Äspö hard rock laboratory. Peter Niemz, Dr. Günther Zimmermann, and Dr. Sebastian von Specht for helping with the acoustic emission and the hydraulic data. Prof. Dr. Oliver Ritter for providing us with MT data from the Wittstock Remote MT station.
- HS ORKA for providing access to the site and providing me the data of RN-15/IDDP-2.
- Steinþór Níelsson, Stephan Audunn Stefansson, Ragna Karlsdóttir and Knútur Árnason from the Iceland Geosurvey (ISOR) for their conceptual and logistical support before and during the surveys.
- Dr. Yassine Abdelfettah for support in MT fieldwork, processing of MT data and obtaining the Äspö datasets.
- Dr. Anne Neska for her advice and support for the MT data processing.
- Dr. Emmanuel Gaucher and Rike Köpke for the seismic data.
- the working group Geothermal Science and Technology at the TU Darmstadt for giving me feedback and helpful suggestions in the Geophysics meeting.
- the Geoenergy group at INE for many discussions, feedback, and support in the last years. Special thanks to my office colleagues Natalia Cornejo and Katharina Schätzler.
- my colleagues and the Ph.D. students at INE for a warm-hearted atmosphere and lots of joyful lunch and coffee, tea, and cake breaks.
- Dr. Wiebke Mörbe for corrections and proofreading.
- to my family and friends for their patience and support in the last years.
- This thesis is dedicated to my late grandma. Thank you for always supporting and encouraging me. We miss you.

Contents

List of Figures

List of Tables

List of Abbreviations

AE	**A**coustic **E**mission
EGS	**E**nhanced **G**eothermal **S**ystem
EM	**E**lectro**M**agnetic
EMR	**E**lectro**M**agnetic **R**adiation
FHF	**F**atigue **H**ydraulic **F**racturing
HF	**H**ydraulic **F**racturing
HRL	**H**ard **R**ock **L**aboratory
LS	**L**east **S**quare
MD	**M**easured **D**epth
MF	**M**ain **F**rac
MT	**M**agneto**T**elluric
RF	**R**e **F**rac
SP	**S**elf-**P**otential
TVD	**T**rue **V**ertical **D**epth

Physical Constants

Avogadro's number	$\mathrm{N} = 6.02214076 \cdot 10^{23} \ \mathrm{mol}^{-1}$
dielectric permittivity of free space	$\mu_0 = 8\,85 \cdot 10^{-14} \ \mathrm{A\,s\,V^{-1}\,m^{-1}}$
magnetic permeability of free space	$\epsilon_0 = 4 \cdot \pi \cdot 10^{-7} \ \mathrm{V\,s\,A^{-1}\,m^{-1}}$
Molar gas constant	$\mathrm{R} = 8.3144598 \ \mathrm{J\,mol^{-1}\,K^{-1}}$
Speed of Light	$c_0 = 2.99792458 \cdot 10^8 \ \mathrm{m\,s^{-1}}$
Unit charge	$\mathrm{e} = 1.602176634 \cdot 10^{-19} \ \mathrm{C}$

List of Symbols

Symbol	Name	Unit
B	magnetic induction	T
C	salt concentration	$\mathrm{mol\,L^{-1}}$
D	electric displacement	$\mathrm{Cm^2}$
D_L	dispersion coefficient	$\mathrm{m^2\,s^{-1}}$
E	electric field	$\mathrm{V\,m^{-1}}$
I	electric current	A
H	magnetic intensity	$\mathrm{A\,m^{-1}}$
j	current density	$\mathrm{Am^{-2}}$
k	complex wave number	$\mathrm{m^{-1}}$
q	electric charge	C
r_0	average frontal position of injected fluid	m
T	temperature	K
u	ionic mobility	$\mathrm{m^2\,s^{-1}\,V^{-1}}$
ΔV	electric potential difference	V
$\epsilon = \epsilon_0\,\epsilon_r$	dielectric permittivity	$\mathrm{A\,s\,V^{-1}\,m^{-1}}$
λ	wave length	m
μ_r	magnetic permeability	$\mathrm{V\,s\,A^{-1}\,m^{-1}}$
ρ	electric resistivity	Ωm
σ	conductivity	$\mathrm{S\,m^{-1}}$
ϕ_P	porosity	%
ψ	electric potential	V
ω	angular frequency	Hz

Chapter 1

Introduction

It is well-known that fluid injection into the underground can lead to induced seismicity or even trigger earthquakes (Charléty et al. 2007; Edwards et al. 2015). Moreover, fluids are also one of the crucial elements in the formation of natural and/or large earthquakes (Deichmann et al. 2006; Hubbert and Rubey 1959). Therefore, earthquakes can reach a high level of hazard to human beings and their living environment with the respective financial consequences. For example, the Tohoku earthquake in 2011 resulted in damages equal to about 210 billion US$ (Allmann et al. 2019).

Forecasting earthquakes in space and time has therefore been a goal for decades. However, still today, it is limited to the calculation of the probability that a significant earthquake will occur in a specific area within a certain number of years (Kagan and Knopoff 1976, 1977). One possibility to overcome this barrier can be precursor phenomena. In the 1980-ties, observed gas emissions such as Radon were considered a short-term precursor due to its radioactive behavior and short half-life (Cicerone et al. 2009; D'Incecco et al. 2021). Thus changes in the radon concentrations can be monitored with a very good time resolution. In the last decades, temporal electric, magnetic or electromagnetic (EM) anomalies have been investigated for their potential as a precursor. The link between seismic deformation and spatial changes in the distribution of electric charges in a medium is called seismo-electric coupling.

They are generated when seismic waves travel through porous media (Gharibi et al. 2004; Revil and Jardani 2013). Two types of electrical disturbances are observed when a seismic wave travels through the porous material. First, the seismic wave propagation generates electrical current due to the displacement of the electrical diffusive layer. The seismic and the coseismic electrical signals have the same speed. The amplitudes of the coseismic electromagnetic signals are controlled by the properties of the porous material and by the properties of the pore fluid/solid interface (Gharibi et al. 2004). In addition to the co-seismic signals, a second phenomenon is generated when a seismic wave moves through a sharp interface characterized by a change in electrical or mechanical properties (Gharibi et al. 2004). The mechanical energy is converted into EM energy producing a dipolar EM excitation.

Note that electrokinetic phenomena, i.e. spatial changes in the distribution of electric charges linked to fluid flow, may also explain temporal electric anomalies (Pritchett and Ishido 2005). Since fluids take a crucial part in earthquake mechanics, a distinction of the two effects is challenging.

The seismo-electric coupling refers to the contemporary interaction between seismic deformation and EM anomalies. For qualification as a precursor, a temporal shift to the period before the earthquake occurs is necessary. This can occur during a fore-shock period or by EM emissions already in the a-seismic deformation period before the earthquake. The latter has been demonstrated in laboratory experiments by Freund (2011).

Freund (2011) discovered that minerals in common crustal rocks contain previously overlooked defects (peroxy links), releasing electronic charge carriers when subjected to stress. These highly mobile carriers can outflow the stressed rock and constitute an electric current generating magnetic field variations and low-frequency EM emissions. The situation is similar to that in a battery. Freund (2011) showed that when the battery circuit is closed during loading experiments, the outflow of charge carriers is possible generating current with magnitudes from nano to pico Ampère. By arriving at Earth's surface, the air can be ionized, and the generation of perturbation in the ionosphere might be possible (Freund 2011).

Field observations also reveal electric, magnetic, or EM activity before major earthquakes. In this context, Ohta et al. (2013) observed an increase in the magnetic field intensity on all three field components five days before the main-shock as mentioned above of the Tohoku earthquake on March 11, 2011 in the frequency range of 0.1 - 24 Hz. Note, the fore-shocks were observed only two days before the main-shock (Hirose et al. 2011). A summary of observed changes in the electric, magnetic, and EM fields in connection to earthquakes reveals a median emission frequency range of 3 - 10 kHz (Petraki et al. 2015). Precursors are not only needed to forecast large-scale earthquakes but also helpful down to reservoir scale. On this scale, induced seismicity is a major issue, in particular, during fluid injection.

In some cases, such as the Pohang project in Korea (Grigoli et al. 2018; Kim et al. 2018), injection even triggered earthquakes of magnitudes up to 5.5 (Frohlich 2012; Häring et al. 2008; Smith et al. 2000). Such examples led to the development of mitigation approaches to reduce the seismic risk, particularly for geothermal engineering. Along with the successful reduction of induced seismicity in a number of events and magnitude in engineered geothermal systems (EGS, e.g., Schill et al. (2017)), the need for alternative monitoring techniques raises.

Most recent developments point to super-computing, including millions of possible scenarios based on forecasting underground processes by statistical approaches (Driesner et al. 2020). As mentioned above, EM methods are based on observations from natural earthquakes and offer an experimental approach.

In this thesis, two EM methods at different frequency ranges, namely magnetotellurics (MT, 0.01 - 10 Hz) and electromagnetic radiation (EMR, 35 - 50 kHz) and electric self-potential (SP, 1 Hz), are employed.

MT measures time variations in Earth's natural electric and magnetic to determine the electrical conductivity of the Earth's subsurface down to great depths. MT is a standard tool for geothermal exploration and has recently been increasingly used for monitoring purposes. One of the first successful applications of the MT method as a monitoring tool was conducted by Peacock et al. (2013, 2012). At Paralana 2 borehole (South Australia), a volume

of 3'100 m^3 of saline water at up to 60 L/s and up to 62 MPa was injected into meta-sediments at 3'680 m depth (Peacock et al. 2013, 2012). A second injection took place with 36'500 m^3 volume at 53 L/s and up to 48 MPa into the Habanero-4 well . The obtained MT results showed an order of a few percent but still significant changes in MT responses (Didana et al. 2017, 2016). Mapping phase tensor residuals reveal temporal and spatial changes generated by a growing body at depth, indicating directional reservoir evolution (Peacock et al. 2013, 2012).

The first long-term MT monitoring of a hydraulic stimulation occurred in the EGS Rittershoffen (Abdelfettah et al. 2018). The MT monitoring covered production and injection experiments (flow rates up to 28 L/s (GRT1) and 42 L/s (GRT2) into the doublet (Abdelfettah et al. 2018; Baujard et al. 2017). The results reveal resistivity decreases from about 1 to 0.1 Ωm in the components with a preferential direction sub-parallel to the minimum horizontal stress (Shmin) and perpendicular to the expected fracture propagation direction (Abdelfettah et al. 2018). Note that this effect is observed during the injection but not during production.

Marquis et al. (2002) and Darnet et al. (2004) report significant increases in electric self-potential (SP) during the fluid injection into the EGS reservoir at Soultz-sous-Forêts, France. Darnet et al. (2006) stated that electrokinetic phenomena dominated the observed signals. Moreover, the second increase in self-potential is observed during the so-called shut-in phase followed by a slow SP decay due to fluid flow even weeks after the injection ended. Schoenball et al. (2014) observed a change in the stress regime during the injection: the transitional normal faulting-strike slip regime changes to a predominantly normal faulting one during injection and changes back after the injection (Schoenball et al. 2014). The authors observed more released energy than seismically observed during stimulation and figured that it could be a strong indicator for large-scale aseismic deformation during hydraulic stimulation.

At laboratory scale, the role of SP in the characterization of the stimulation process was investigated by Hu et al. (2020). During a laboratory EGS stimulation, the authors fractured a granite block with a 30 cm edge length. They revealed a significant correlation between the pressure drop and the increases in the SP amplitude (Hu and Ghassemi 2020). These coupling effects are generated by electrokinetic effects as described during the injection in Soultz (Hu et al. 2020).

All these observations raise the issue of a better understanding of electrokinetic and seismo-electric effects and their (major?) role in the mechanical response of the reservoir to hydraulic stimulation.

This thesis aims to understand the interaction between hydraulic, mechanical, and electric, magnetic, and electromagnetic processes. It monitors and analyses possible electrokinetic and seismo-electric effects in different experimental settings in the context of possible precursors of earthquakes and induced seismicity. The data were acquired during two different projects in a reservoir- and underground laboratory environment, respectively:

- The Horizon2020 project DEEPEGS (Deployment of deep enhanced geothermal systems for sustainable energy business) aimed to demonstrate deep

enhanced geothermal systems in general and the stimulation technologies in geothermal reservoirs in particular. MT data were acquired at the geothermal well RN-15/IDDP-2, located on the Reykjanes peninsular (SW Iceland). MT monitoring covered the drilling period and subsequent stimulation.

- EMR and SP data were acquired in the framework of the Helmholtz program research at the Äspö Hard Rock Laboratory (Sweden) during hydraulic fracturing experiments. The project concerns the testing of conventional hydraulic fracturing as well as so-called fatigue hydraulic fracturing.

This thesis is composed of seven chapters, including this introduction. The second chapter deals with the geophysical methods used for this thesis. Chapter three gives a brief overview of the experimental setup and data acquisition, followed by chapter four about the theoretical background of the data processing, including noise in electromagnetic data. Chapter five analyses the results of the MT monitoring of the deepening of the geothermal well RN-15/IDDP-2 and chapter six of the SP and EMR monitoring of the hydraulic fracturing experiments at the Äspö hard rock laboratory (HRL). The thesis finish with a discussion and conclusion in the last chapter. Results of this thesis have already been published in two publications as follows:

- Haaf, N. and E. Schill (2019). "Processing of magnetotelluric data for monitoring changes in electric resistivity during drilling operation." In: PROCEEDINGS,44th Workshop on Geothermal Reservoir Engineering 44 (see Haaf and Schill (2019)).

- Haaf, N. and E. Schill (2021). "Noise" during long-term continuous magnetotelluric monitoring of RN-15/IDDP-2 well engineering (Reykjanes peninsular, Iceland): A geogenic origin?" In: Geothermics 96, p. 102192 (see Haaf and Schill (2021)).

The first paper includes the adapted processing scheme of this thesis and is included in chapter four. The latter contributed to chapters three, four, and five.

Chapter 2

Theoretical background of the geophysical methods

This chapter introduces electric resistivity as physical quantity and the factors controlling it. The second part deals with the elementary EM theory on which MT is based. In addition, the EMR method is introduced, and in the last part, the SP method is explained.

2.1 Electric resistivity

The electric resistivity ρ or its inverse the electric conductivity σ describes the transport of electric charges in material. Figure 2.1 gives an overview of different rock types and their resistivity values from very low values for massive sulphides up to 10'000 Ωm (e.g., limestone). The electric resistivity of a rock depends not only on the host rocks but also on the pore fluid properties. Which kind of conduction mechanism dominates depends among other things on the salinity of the pore fluid.

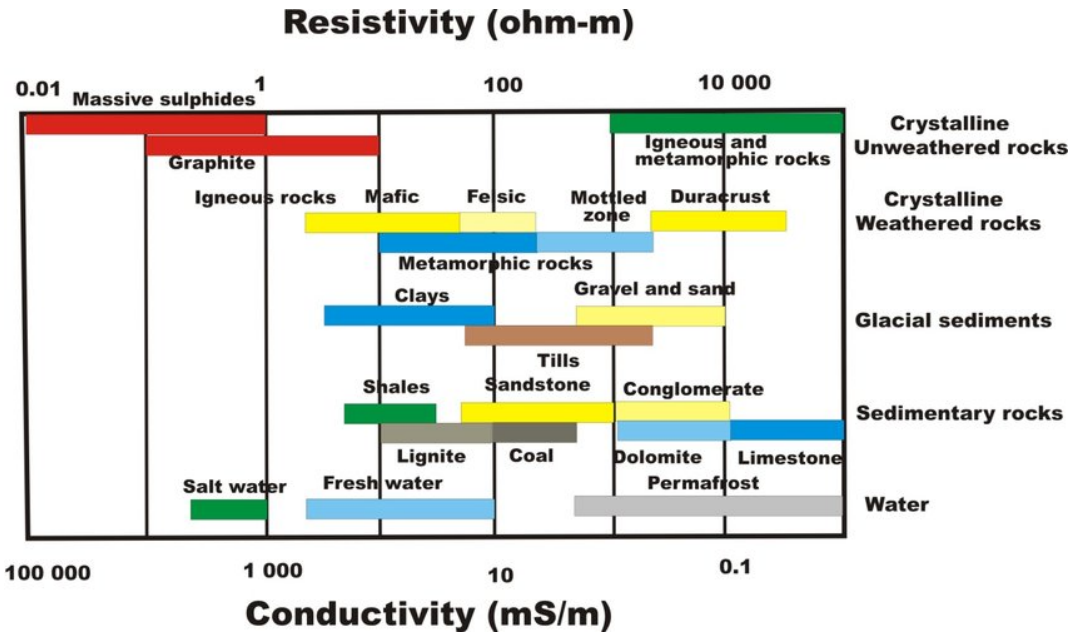

FIGURE 2.1: Overview of resistivity/conductivity values for different rock types (Best 2015).

Hersir and Árnason (2010) summarizes the three main contributions to the conduction mechanisms as: the pore fluid conduction by dissolved ions in the pore fluid. The surface conduction by absorbed ions on the pore surface and the mineral conduction in alteration minerals. The conduction in the rock matrix is generally negligible (Hersir and Árnason 2010). Figure 2.2 illustrates the different conduction mechanisms.

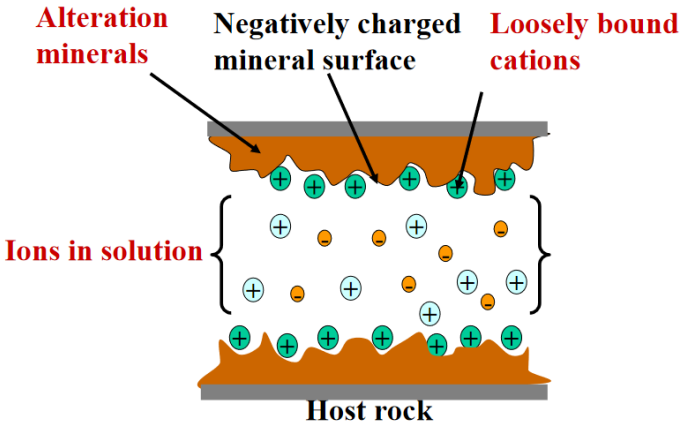

FIGURE 2.2: Overview of the conduction mechanisms (Hersir and Árnason 2010).

2.1.1 Factors affecting the resistivity

The resistivity of a rock depends on (Hersir and Árnason 2010; Simpson and Bahr 2005):

- porosity
- amount of water (saturation)
- salinity of the water
- temperature
- water-rock interaction and alteration
- pressure
- steam content in water

In most rocks near the Earth's surface, conduction is dominated by pore fluid conduction in aqueous solution of common salts. They are distributed in the pores of the rock and/or at the interface between rock and water. The rock matrix itself is usually an insulator (Hersir and Árnason 2010).

Archie (1942) introduced an empirical formula to estimate the conductivity of porous rock, the so-called *Archie's law*. The conductivity varies with the volume and the arrangement of the pores and even with the conductivity and amount of the contained water (Telford et al. 1990). The equation is as follows

$$F = \frac{\rho_e}{\rho_f} = \frac{a}{\phi_p^m} \tag{2.1}$$

where ϕ_p is the fractional pore volume (porosity), ρ_e is the bulk resistivity, ρ_f is resistivity of the water saturating the pores, m is the cementation factor ($1.3 \leq m \leq 2.5$) and the ratio ρ_e/ρ_f is the formation factor F.

Due to a variety of salts in the groundwater solution, the equivalent salinity is defined as the salinity of a NaCl solution with the same resistivity as the particular solution (Hersir and Árnason 2010). The mobility of ions is consistent without large variation; hence the equivalent salinity is close to the true salinity. Figure 2.3a shows the almost linear relationship between the conductivity and the salinity of electrolytes. Increasing mobility of dissolved ions contributes to reducing resistivity with increasing temperature (Figure 2.3b). But above 300 °C, electrolyte resistivity starts to increase with temperature, because a decrease of the dielectric permittivity of water results in a decrease in the number of dissociated ions in the water (Suriyaarachchi 2012).

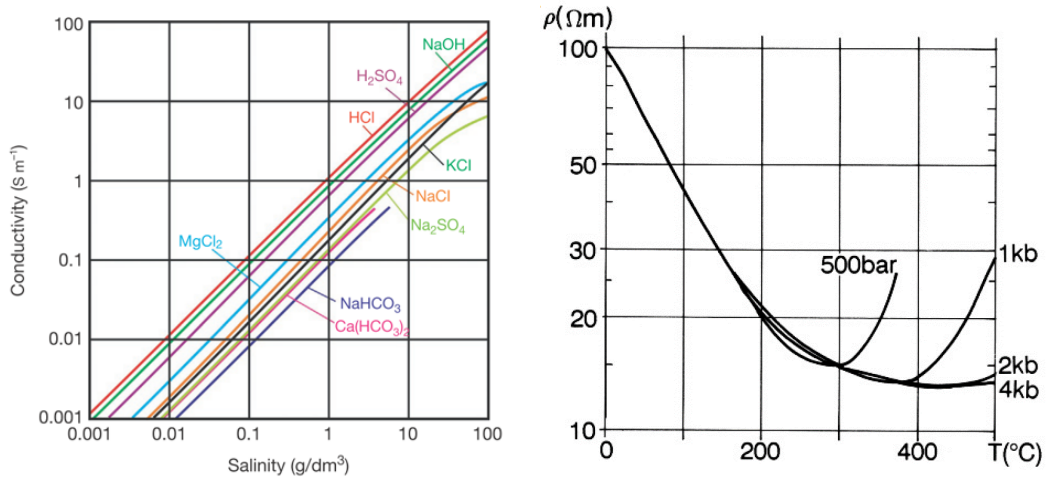

(A) (B)

FIGURE 2.3: Variations of resistivity of (a) NaCl solutions from measurements by Glover (2015), modified after Keller and Frischknecht (1966) and (b) as a function of temperature at different pressures by Suriyaarachchi (2012), modified after (Quist and Marshall 1968).

Figure 2.4 shows the relationship between the bulk resistivity and the pore fluid resistivity for different porosity and temperatures for rocks in the uppermost kilometer of the Icelandic crust outside the volcanic zone. The model developed by Flóvenz et al. (1985) includes both electrolytic and mineral conduction.

Archie's law applies for pore fluid resistivities less than 2 Ωm. Thus, the dominant conductivity is pore fluid conductivity. For rocks with resistivities larger than 2 Ωm, the bulk resistivity is mainly dependent on porosity and temperature. Thus, the dominant conductivity is mineral and/or surface conductivity (Flóvenz et al. 1985).

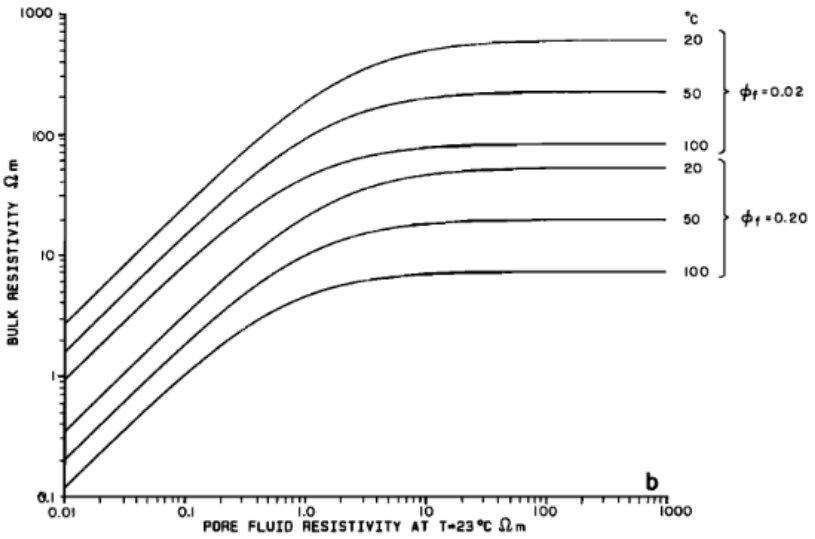

FIGURE 2.4: Bulk resistivity as a function of pore fluid resistivity for different values of porosity and temperature (Flóvenz et al. 1985).

2.1.2 Alteration minerals and resistivity structure in Iceland

The examples in this section showed that low resistivity values are not only due to the presence of fluids. It is possible that in high-temperature geothermal systems, alteration minerals can cause an even higher reduction of resistivity than fluid flow. The water-rock interaction and the chemical transport by geothermal fluids produces different minerals (Hersir and Árnason 2010). Alteration minerals depend on type of primary minerals and chemical composition of geothermal fluid, temperature, porosity and permeability (Arnason et al. 2000). Particular clay minerals are only formed in certain temperature ranges as shown in Figure 2.5. Below 200 °C zeolites and smectite are formed, chlorite is formed at temperatures of 230 - 250 °C, and epidote is formed at even higher temperatures (> 250 °C) (Hersir and Árnason 2010).

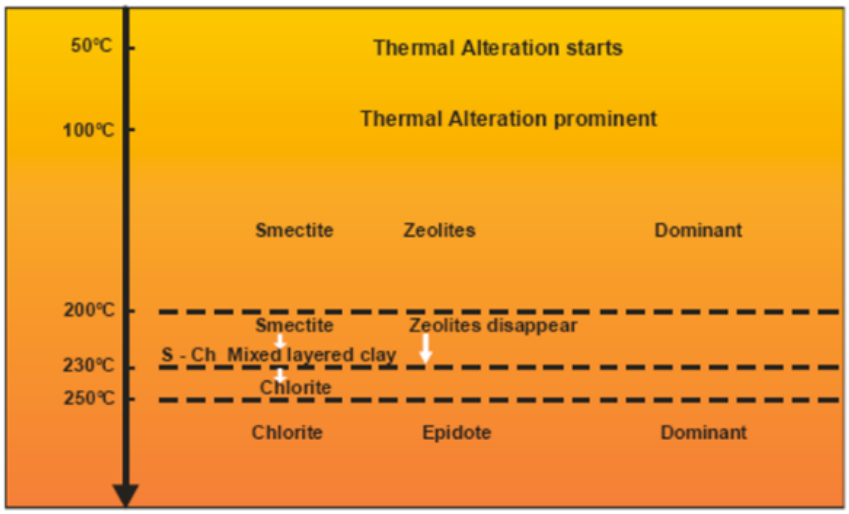

FIGURE 2.5: Alteration mineralogy and their corresponding temperature (Hersir and Árnason 2010).

Figure 2.6 shows a modified version of the main resistivity structure of the basaltic crust in Iceland and the processes involved based on in-situ measurements and laboratory data (Flóvenz et al. 2005). The uppermost part is unaltered with relatively high resistivity values depending on the pore fluid salinity. Below this, the zeolite-smectite zone starts with strongly reduced resistivity and dominant mineral conduction. Resistivity decreases further with increasing depth, partially due to increased temperature and increased alteration (Flóvenz et al. 2005). When the mixed layer clay zone entered, the resistivity increases again, likely due to strongly reduced cation exchange capacity of the clay minerals (Flóvenz et al. 2005). The transition from the smectite to mixed clays seems to happen at a temperature close to 230 °C (see Figure 2.5). At even greater depths the resistivity is considered to decrease slowly due to increasing temperature in the reservoir. For temperatures > 300 °C an increase in resistivity is expected (see Figure 2.3b).

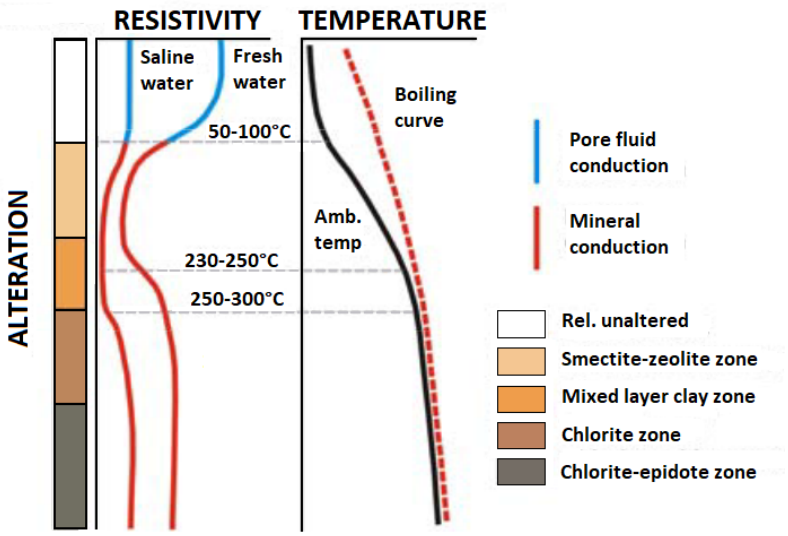

FIGURE 2.6: Summarized resistivity structure for the basaltic crust in Iceland (Flóvenz et al. 2005).

2.2 Magnetotelluric method

The passive geophysical method MT measures earth natural electromagnetic field variation to obtain information about the subsurface conductivity structure. Three magnetic components, B_x, B_y and B_z, and two electric components, E_x and E_y, are installed, whereas the indices x indicate the North-South, y the East-West and z the vertical directions.

2.2.1 Origin and characteristics of MT fields

There are two sources for the MT signal shown in Figure 2.7 (Simpson and Bahr 2005). For frequency larger than 1 Hz, the global lightning activity creates energy traveling around the globe in a wave-guide between Earth's surface and the ionosphere. Part of this energy penetrates the subsurface.

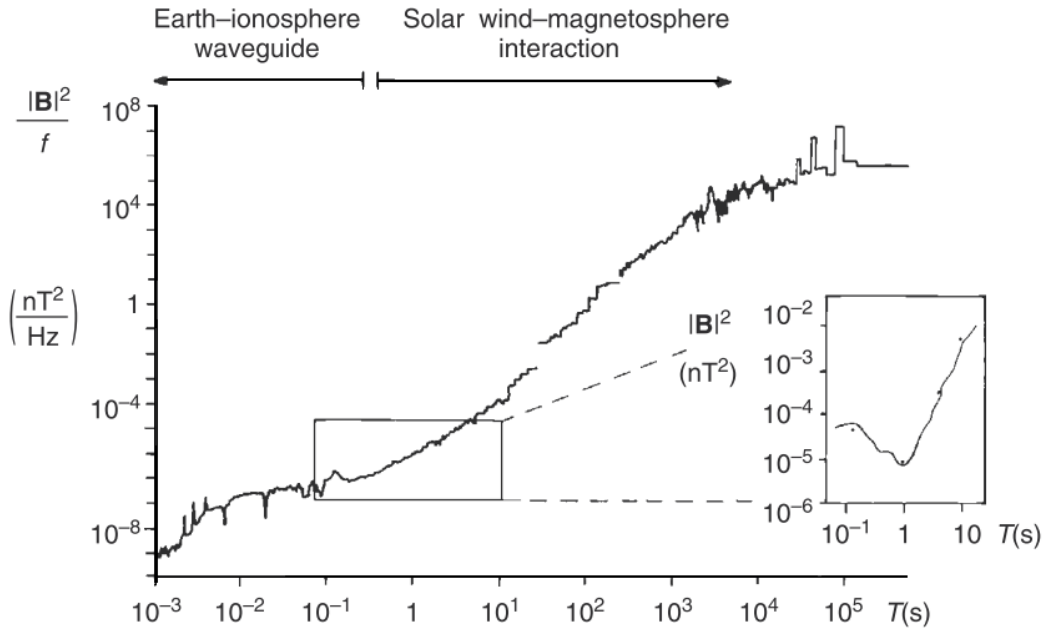

FIGURE 2.7: Power spectrum of natural magnetic variations of the MT source field with $1/f$ spectra (Simpson and Bahr 2005).

Frequencies smaller than 1 Hz are caused by the solar wind's emission of ion stream disturbing Earth's magnetic field. Low-frequency electromagnetic energy is produced and penetrates the Earth. Both sources produce time-varying EM waves, which cause small but measurable variations in magnetic and electric fields. At about 1 Hz, the power spectrum has a minimum, which is shown in the detailed Figure in the period range from 0.1 - 10 s in Figure 2.7. Consequently, the signal is sensitive to EM noise, which reduces the quality of estimation of the MT responses in that interval, the so-called *dead band*.

2.2.2 Elementary EM theory

The table on pages xxvii and xxix lists physical constants and physical quantities with symbols, names, and units, respectively. The notation in this chapter is as follows: scalars are written in lowercase letters, vectors in lowercase bold letters, and matrices in bold capital letters. **Exceptions** are the known physical quantities: $\mathbf{E}, \mathbf{B}, \mathbf{D}, \mathbf{H}$. They are as matrices in bold, capital characters.
Three assumptions (Chave and Jones 2012; Simpson and Bahr 2005) are made to adapt the general wave equation theory to the MT context:

- all EM fields are treated as conservative and analytic away from their sources,
- passive EM source fields treated as uniform, plane-polarized EM waves impinging on the Earth at near vertical incidence and
- frequencies are so low that displacement currents are negligible.

Maxwell's equations describe the properties and the propagation of electromagnetic waves. They are a set of uncoupled, linear, first-order differential equations. The following derivation of the Telegrapher's equation follows Ward and Hohmann (1988) and start with Maxwell's equations in differential form:

- **Faraday's law** :

$$\nabla \times \mathbf{E} = -\frac{\partial \mathbf{B}}{\partial t} \tag{2.2}$$

  Faraday's law of induction states that an induced electric field is proportional to the negative rate of change of magnetic flux.

- **Ampère's law** :

$$\nabla \times \mathbf{H} = \frac{\partial \mathbf{D}}{\partial t} + \mathbf{j} \tag{2.3}$$

  Ampère's law shows that a generated magnetic field is proportional to the total electric current in the region.

- **Coulomb's law** :

$$\nabla \cdot \mathbf{D} = q \tag{2.4}$$

  Coulomb's law states that an electric charge is the source of an electric field.

- **Gauss law for magnetic fields** :

$$\nabla \cdot \mathbf{B} = 0 \tag{2.5}$$

  Gauss law for magnetic fields states the non-existence of magnetic monopoles.

The divergence of current density is equivalent to rate of accumulation of charge density

$$\nabla \cdot \mathbf{J} = -\frac{\partial Q}{\partial t} = -\frac{\partial}{\partial t}(\nabla \cdot \mathbf{D}). \tag{2.6}$$

The relations between magnetic field and flux are

$$\mathbf{B} = \mu_r \mathbf{H}. \tag{2.7}$$

If we assume a homogeneous isotropic media we express the material equations together with Ohm's law, as

$$\mathbf{B} = \mu \mathbf{H} \qquad \mathbf{D} = \varepsilon \mathbf{E} \qquad \mathbf{J} = \sigma \mathbf{E}. \tag{2.8}$$

We assume that in regions of finite conductivity charges do not accumulate during current flow, thus

$$\nabla \cdot \mathbf{J} = 0 \qquad \nabla \cdot \mathbf{D} = \varepsilon \nabla \cdot \mathbf{E} = 0. \tag{2.9}$$

Applying the curl to equations 2.2 and 2.3 and substituting the constitutive equations for **B**, **D** and **J** gives:

$$\nabla \times \nabla \times \mathbf{E} = -\mu \left(\frac{\partial}{\partial t} \right) (\nabla \times \mathbf{H}) \tag{2.10}$$

$$\nabla \times \nabla \times \mathbf{H} = \sigma \nabla \times \mathbf{E} + \varepsilon \left(\frac{\partial}{\partial t} \right) (\nabla \times \mathbf{E}) . \tag{2.11}$$

Applying the vector identity

$$\nabla \times \nabla \times \mathbf{F} = \nabla(\nabla \cdot \mathbf{F}) - \nabla^2 \mathbf{F} \tag{2.12}$$

to equations 2.11 and 2.10 with $\mathbf{F} \in [\mathbf{E}, \mathbf{H}]$. Substituting of $\nabla \times \mathbf{E}$ and $\nabla \times \mathbf{H}$ with 2.2 and 2.3 and considering the material equations leads to the **Telegraphers equations** :

$$\nabla^2 \mathbf{E} - \mu\varepsilon \frac{\partial^2 \mathbf{E}}{\partial t^2} - \mu\sigma \frac{\partial \mathbf{E}}{\partial t} = 0 \tag{2.13}$$

$$\nabla^2 \mathbf{H} - \mu\varepsilon \frac{\partial^2 \mathbf{H}}{\partial t^2} - \mu\sigma \frac{\partial \mathbf{H}}{\partial t} = 0 \tag{2.14}$$

The Telegrapher's equations are a set of two uncoupled wave equations describing the propagation of electric and magnetic fields in the time-domain in an isotropic medium. A solution would be a simple sinus wave.

A sinusoidal time variation:

$$\mathbf{F}(\mathbf{t}) = \mathbf{F}_0 \exp^{i\omega t - \mathbf{kr}} \qquad \frac{\partial \mathbf{F}(\mathbf{t})}{\partial t} = i\omega \mathbf{F} \tag{2.15}$$

where F_0 is the amplitude and the wave number $k = 1/\lambda$ (wave length λ). k points in the moving direction of the wave and fulfills the equations 2.13 and 2.14. Thus, the equations 2.13 and 2.14 are simplified to

$$\nabla^2 \mathbf{E} + \underbrace{(\mu\varepsilon\omega^2}_{\substack{\text{displacement} \\ \text{currents}}} - \underbrace{i\mu\sigma\omega)}_{\substack{\text{conduction} \\ \text{currents}}} \mathbf{E} = 0 \tag{2.16}$$

$$\nabla^2 \mathbf{H} + \underbrace{(\mu\varepsilon\omega^2}_{\substack{\text{displacement} \\ \text{currents}}} - \underbrace{i\mu\sigma\omega)}_{\substack{\text{conduction} \\ \text{currents}}} \mathbf{H} = 0. \tag{2.17}$$

The second and the third term on the left side of the equation describe the displacement and the conduction currents, respectively. The electromagnetic **Helmholtz equations** describe the propagation of electric and magnetic field vectors in an isotropic homogeneous medium.

In induction studies, the displacement current is generally neglected. That is justified within the conductor because the conduction current σE exceeds the displacement current even in the case of shortest periods (0.001 s) and highest resistivities (10^5 Ωm) by a factor of 100 (Weidelt 1972). Therefore, the quasi-static approximation is valid:

$$\omega^2 \mu\varepsilon << \omega\mu\sigma \Leftrightarrow \frac{\sigma}{\omega\varepsilon} >> 1. \tag{2.18}$$

Subsequently, the Helmholtz and the Telegrapher's equations are reduced to the **Diffusion equations**:

$$\nabla^2 \mathbf{F} = i\mu\sigma\omega \mathbf{F}. \tag{2.19}$$

The diffusion equations are second order, linear differential equations. Therefore, the imaginary wave number is given by:

$$\kappa = \sqrt{-i\mu\sigma\omega} = (1-i)\sqrt{\frac{\mu\sigma\omega}{2}} \tag{2.20}$$

with the help of equation 2.15 and 2.19.

The solution is a damped wave with a damping factor of $-i\sqrt{\frac{\mu\sigma\omega}{2}}$ of the wave number. The depth z at which the amplitude of the wave drops by a factor of $\frac{1}{e}$ is the so-called *skin depth*:

$$\delta_{FD} = \frac{1}{Im(\kappa)} = \sqrt{\frac{2}{\mu\sigma\omega}}. \tag{2.21}$$

2.2.3 MT Parameter and their representation

The time series of the horizontal components are linearly related in the frequency domain by the impedance tensor **Z**:

$$\begin{pmatrix} E_x \\ E_y \end{pmatrix} = \begin{pmatrix} Z_{xx} & Z_{xy} \\ Z_{yx} & Z_{yy} \end{pmatrix} \begin{pmatrix} B_x \\ B_y \end{pmatrix}. \tag{2.22}$$

The impedance tensor **Z** is complex. The apparent resistivity and the phase are calculated from its components:

$$\rho_{a,ij} = \frac{\mu_0}{\omega}||Z_{ij}||^2 \tag{2.23}$$

and

$$\phi_{ij} = \arctan\left(\frac{\Im(Z_{ij})}{\Re(Z_{ij})}\right). \tag{2.24}$$

with i,j for x and y, respectively. The apparent resistivity and the corresponding phase are the so-called *transfer functions*. The *apparent resistivity* is the average resistivity of an equivalent uniform half-space.

Caldwell et al. (2004) introduced the phase tensor as a physical quantity independent from galvanic distortion effects:

$$\Phi = \mathbf{X}^{-1}\mathbf{Y} \tag{2.25}$$

The phase tensor is the product of the real **X** and the imaginary part **Y** of the impedance tensor. It is a second rank tensor and, thus, is defined by a direction and three independent scalar coordinate invariants. For example, Caldwell et al. (2004) used the maximum Φ_{max} and minimum Φ_{min} tensor values as the major and minor axis of an ellipse, respectively, and the skew angle β to depict the phase tensor in an elliptical shape as shown in Figure 2.8.

The skew angle β is defined as:

$$\beta = \frac{1}{2}\arctan\left(\frac{\Phi_{xy} - \Phi_{yx}}{\Phi_{xx} + \Phi_{yy}}\right). \tag{2.26}$$

The angle α reflects the tensor dependency to the coordinate system with $\alpha - \beta$ defining the orientation of the major axis. α is defined as:

$$\alpha = \frac{1}{2}\arctan\left(\frac{\Phi_{xy} + \Phi_{yx}}{\Phi_{xx} - \Phi_{yy}}\right). \tag{2.27}$$

The phase tensor can now be written as

$$\Phi = \mathbf{R}^T(\alpha - \beta)\begin{pmatrix} \Phi_{max} & 0 \\ 0 & \Phi_{min} \end{pmatrix}\mathbf{R}(\alpha + \beta) \tag{2.28}$$

where as $\mathrm{R}(\alpha + \beta)$ is the rotation matrix:

$$\mathbf{R}(\alpha + \beta) = \begin{pmatrix} \cos(\alpha + \beta) & \sin(\alpha + \beta) \\ -\sin(\alpha + \beta) & \cos(\alpha + \beta) \end{pmatrix}. \tag{2.29}$$

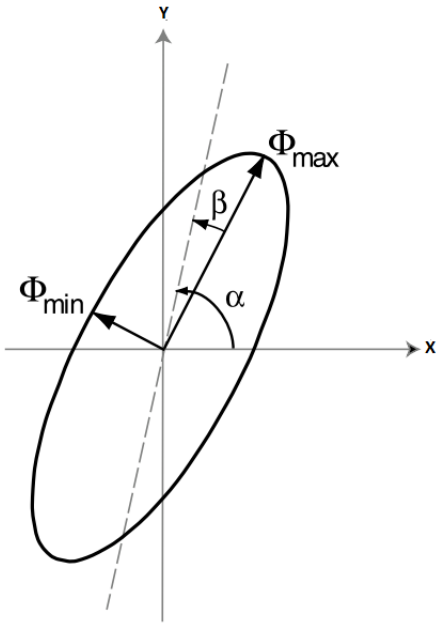

FIGURE 2.8: The phase tensor with its invariants Φ_{max}, Φ_{min}, β and the angle α (Caldwell et al. 2004).

Peacock et al. (2012) introduced the phase tensor residual, providing information about geoelectric strike transformation during the injection and gradients in resistivity structure. The phase tensor is calculated between the pre-injection MT parameter minus subsequent 24-hour blocks in percent change.

$$\Delta\Phi_{0j} = \mathbf{I} - (\Phi_0^{-1}\Phi_j). \tag{2.30}$$

with Φ_0 as the phase tensor pre-injection, the phase tensor of a 24 hour block, Φ_j and the unity matrix **I**.

1D

For a 1D subsurface structure the main diagonal elements of the impedance tensor are zero whereas the off-diagonal elements have an opposite sign.

$$Z_{xx} = Z_{yy} = 0 \qquad Z_{xy} = -Z_{yx}. \tag{2.31}$$

The phase tensor has only one single coordinate invariant and thus, the shape of a circle. In a homogeneous half-space case the apparent resistivity represents the real resistivity and a phase of $\phi = 45°$. For a two-layered model the phase is $\phi > 45°$ if the top layer is less conductive than the bottom layer ($\sigma_1 < \sigma_2$) and the phase will be $\phi < 45°$ for $\sigma_1 > \sigma_2$.

2D

In the 2D case, the conductivity varies in vertical and in one horizontal direction. Assuming that the strike direction is sub-parallel to the x-axis, $\sigma = \sigma(y, z)$ the Maxwell equations are decoupled into two sets of equations with independent polarization (Chave and Jones 2012).

The so-called E-polarization (TE mode) has an electric component, **E**, pointing in the strike direction, and a magnetic one, **B**, lying in the plane orthogonal to the strike. For the B-polarization (TM mode) it is vice versa: **B** is in strike direction and **E** in the plane orthogonal to the strike (Chave and Jones 2012).

The impedance tensor main diagonal elements are equal to zero and the off-diagonal impedance elements are different.

$$Z_{xx} = Z_{yy} = 0 \qquad Z_{xy} \neq Z_{yx} \neq 0. \tag{2.32}$$

The phase tensor can be expressed as an ellipse with the maximum principal axis pointing parallel or perpendicular to the regional strike direction.

3D

In the 3D case all four impedance tensor elements are non-equal and non-zero.

$$Z_{xx} \neq Z_{yy} \neq 0 \qquad Z_{xy} \neq Z_{yx} \neq 0. \tag{2.33}$$

The conductivity varies in all three directions. The phase tensor is non-symmetric leading to a skew angle which significantly deviates from zero (Caldwell et al. 2004).

2.3 Electromagnetic radiation method

Earth's natural transient EM fields are detectable in a wide frequency spectrum and with very different energies (see Figure 2.9). Electromagnetic radiation (EMR) emission covers the electromagnetic spectrum in the frequency

range from 1 kHz to 50 MHz. A portable measuring device adapted to the natural EM signals in this frequency range was developed to record the mechanical stress state of Earth's crust via measured EM emissions (Lichtenberger 2006). The so-called *Cerescope* uses directional antennas for measurements that may be evaluated to determine the directions of recently active stresses and the regional stress field.

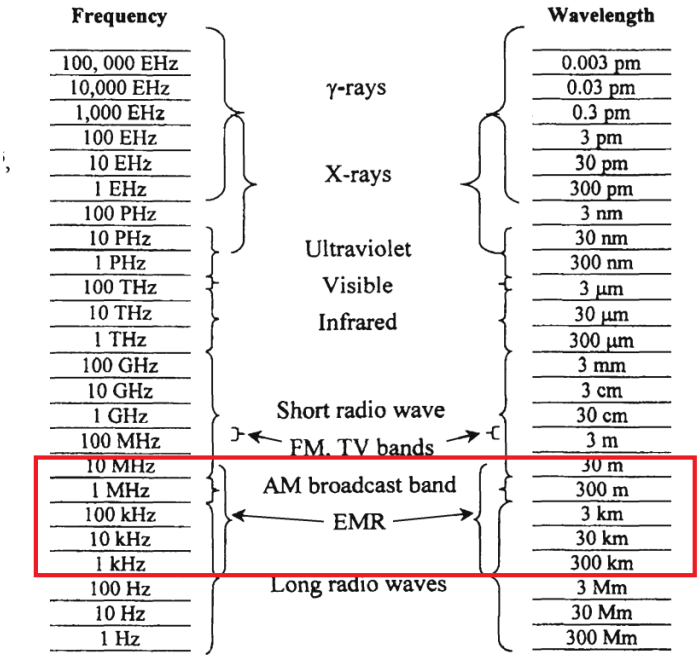

FIGURE 2.9: The electromagnetic spectrum from radio waves to the γ rays. The EMR signals are marked in the red rectangle between 1 kHz to 50 MHz (Rabinovitch et al. 2000).

2.3.1 History of EMR

Urusovskaya (1969) was the first one detecting EMR emission during the loading of rock salt samples. During specimen failure, he detected EM pulses. The next milestone in EMR research was the observation (e.g., Gold et al. 1975; Golovin and Shibkov 1986a,b) that the creation of new microcracks stimulates excitation of EMR. Various EMR aspects were investigated for fracture in many different materials like ice (e.g. Petrenko 1993) and single crystals (Gold et al. 1975; Khatiashvili 1984). Frid (1997a,b, 2000) and Frid (2001) observed EMR anomalies before rockburst and gas outbursts, whereby A. Rabinovitch et al. (2002) investigated EMR induced by explosions. During the seventies and eighties, numerous studies showed an increase in EMR magnitude hours till days before an earthquake and decreased shortly before or at the moment of the earthquake (e.g., Gershenzon et al. 1987; Morgunov 1985). In this context, a summary of electric, magnetic and EM emissions as pre-earthquake precursors is given in Petraki et al. (2015). To conclude, EMR is associated with fractures on multi-scale lengths and related to various applications. Several models failed to explain the EMR phenomena until a careful laboratory investigation of rock failure was performed by the group of Rabinovitch (A. Rabinovitch et al. 1995, 2000, 2003).

2.3.2 EMR model

Bahat et al. (2005) and Frid et al. (2003) introduced a comprehensive model of EMR emission mechanism from cracks as shown in Figure 2.10.

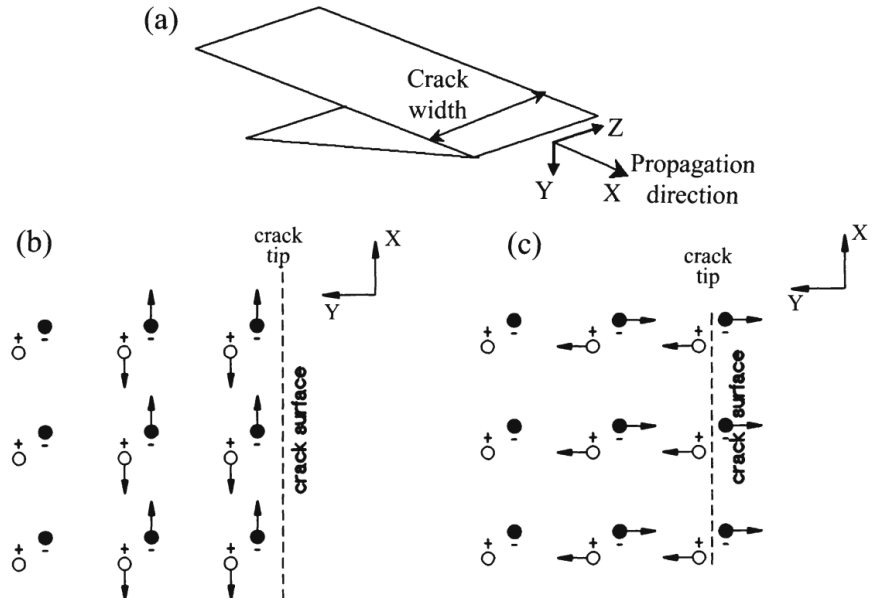

FIGURE 2.10: (a) Schematic sketch of crack propagation model with (b) longitudinal and (c) transversal charge separation. Crack surface lays in x-z-plane with cracks propagating in x-direction (Frid et al. 2003).

In this model, an oscillation of charge carriers causes EMR emissions due to the released energy through crack growth. Breaking of atomic bonds at the crack tip excite atoms along crack walls. They start to move to non-equilibrium positions relative to their steady-state ones and to oscillate around them (Bahat et al. 2005). Oscillating atoms move closer to each other on lines and connect to atoms around them (Bahat et al. 2005). Consequently, the latter participate in the oscillation parallel and perpendicular to crack growth direction too. The positive charges move together in a diametrically opposite phase to the negative ones; thus, the oscillations behave like surface optical waves and decay exponentially into the material (Bahat et al. 2005). The orientation of the resulting oscillating dipole is perpendicular and parallel to the crack walls. Consequently, the emission of longitudinal and transversal EMR waves can be explained by that model (Bahat et al. 2005). Polarization can also occur along the crack tip; therefore, EMR emissions are possible perpendicular to the crack propagation direction.

2.4 Self-potential method

Self-potential is a passive geophysical method to measure the electric potential difference between two points on the surface using a voltmeter and non-polarizing electrodes. Man-made disturbances of the environment, such as buried electric cables or waste disposal sites, can contribute to the SP signal.

Further sources are coupling effects of natural origins, such as electrochemical or electrokinetic effects. In addition to these two possible sources, Darnet et al. (2004) also considers electrothermal effects as the third coupling effect for inducing SP signals.

Revil and Jardani (2013) introduced the seismo-electric coupling as another effect extending the electrokinetic theory to the frequency domain (see section 2.4.3).

2.4.1 The electric double layer

The basic idea of the SP source signal is the electric double layer, as shown in Figure 2.11. A pore water-mineral interface causes a charge separation due to chemical reactions between fluid and solid. The resulting negative charged mineral surface attracts the counterions(+) and repels the coions(-) (Revil and Jardani 2013). They form a diffusive layer with a high amount of counterions and a lack of coions. Besides, the stern layer is formed by sorbed ions on the mineral surface (the o-Plane) and the inner electrical diffusive layer (the d-Plane). The diffusive layer extends from the d-Plane into the pores (Revil and Jardani 2013).

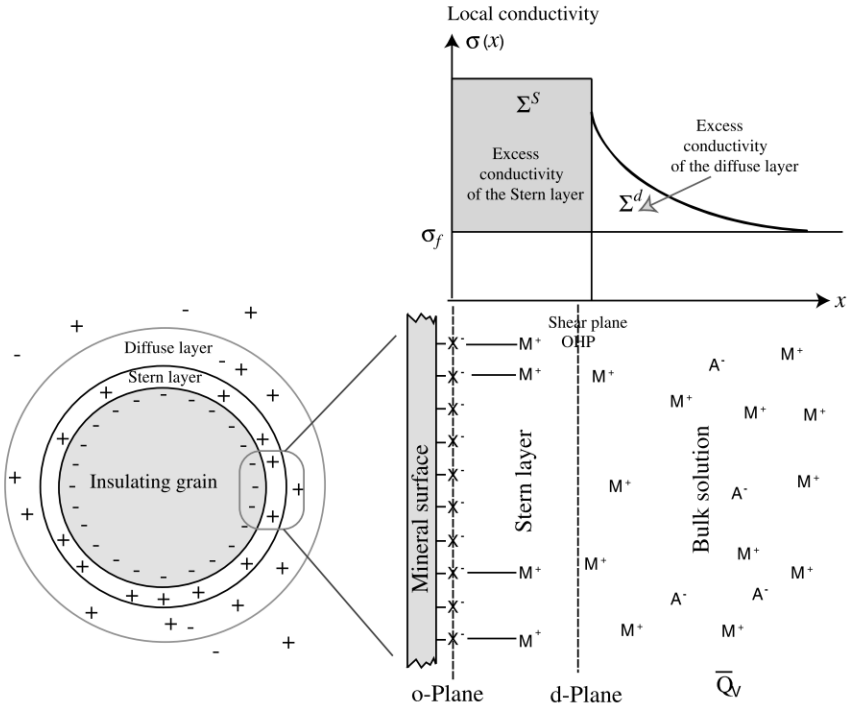

FIGURE 2.11: Sketch of an electric double layer after Revil and Florsch (2010). The stern layer is embedded between o- and the d-plane, the charged mineral surface and the outer diffusive layer, respectively.

Moving fluid with charge carriers will cause a current and, therefore, an electric potential regarding Ohm's law. The electric double layer consists of the stern and the electric diffusive layer. The local conductivity $\sigma(x)$ depends on the local distance x from the charged mineral surface. The Stern layer is responsible for the excess conductivity Σ^S and the diffuse layer for the excess surface conductivity Σ^d. The volumetric charge density $\bar{Q}_V$ of the pore water

corresponds to the (total) charge of the diffuse layer per unit pore volume (in coulombs (Cm^{-3}) (Revil and Jardani 2013).

2.4.2 Poisson equation

This subsection describes the fundamental equation to interpret self-potential signals in the quasi-static regime of the Maxwell equations following Revil and Jardani (2013). The total macroscopic electric current density **J** represents the flux of electrical charges: it is defined as the amount of electrical charge passing per cross-sectional surface area of the porous material per unit time (Am^{-2}). The total macroscopic current density includes the conduction current (described by Ohm's law) and a source current density and is as follows

$$\mathbf{J} = \sigma \mathbf{E} + \mathbf{J}_s \tag{2.34}$$

where **E** is defined as $E = -\nabla\psi$.

Furthermore, a continuity equation for the current density is needed to obtain a field equation for the electrostatic potential ψ. It is defined as

$$\nabla \cdot \mathbf{J} = 0. \tag{2.35}$$

The total current density is conservative meaning that there is no storage of electric charges in a control volume.

Combining both equations 2.34 and 2.35 to an elliptic Poisson-type equation

$$\nabla(\sigma \nabla\psi) = \nabla \cdot \mathbf{J}_s. \tag{2.36}$$

where the self-potential field ψ is the solution. Equation 2.36 states that a source term creates an electric potential distribution in accordance to the divergence of a source current density (Revil and Jardani 2013).

2.4.3 Contributions to the SP Source signal

Electrothermal coupling

Electrothermal signals are driven by temperature differences along with a rock sample, which generates a voltage gradient. Differential thermal diffusion is caused by ions in pore fluid and by electrons and donor ions in the rock matrix (Revil and Jardani 2013).

Electrokinetic coupling

Electrokinetic effects are generated by underground fluid circulation through pores and fractures. Darnet et al. (2004) suggests that electrokinetic coupling effects act as the primary source of subsurface currents in the ground connected to the existence of the electric double layer. Electrokinetic effects can cause rapid temporal changes in self-potential during operation-induced changes in underground flow (Pritchett and Ishido 2005). Also, changes in temperature and composition are relatively slow compared to electrokinetic effects (Ishido and Pritchett 2000).

Electrochemical coupling

Electrochemical effects can play a role in generation SP signals when the ionic concentration differs with location. The ions tend to diffuse through an electrolyte to equalize the concentration. Subsequently, diffusion is driven by the generated voltage gradient. Hu et al. (2020) states that the electrochemical coupling seems to have a significant impact on the SP signal when the concentration contrast between the injected fluid and the pore fluid is large enough.

The electric difference potential ΔV_{EC} generated by the diffusion of a NaCl concentration gradient ΔC can be written as (Maineult et al. 2005)

$$\Delta_{EC} = \phi_P \frac{RT}{Ne} \frac{u_{CL} - u_{Na}}{u_{CL} + u_{Na}} \frac{\Delta C}{C}. \tag{2.37}$$

ϕ_P is the porosity, R is the molar gas constant (J mol^{-1} K^{-1}), T is the absolute temperature (K), u_{CL} and u_{Na} are the ionic mobilities of Cl^- and Na^+ (m^2 s^{-1} V^{-1}). C is the salt concentration (mol L^{-1}), N is Avogadro's number (mol^{-1}) and e the absolute unit charge (C).

The NaCL concentration profiles during injection can be modelled using equation 2.38.

$$C(r,t) = C_0 + \left(\frac{C_1 - C_0}{2}\right) erfc\left[\frac{r - r_0}{2\sqrt{(D_L t)}}\right] \tag{2.38}$$

where C_0 is the initial concentration (mol L^{-1}) and C_1 the concentration of the injected fluid. *erfc* is the complementary error function, r is the distance to the well, r_0 is the average frontal position of the injected water (m) and D_L as dispersion coefficient ($m^2 s^{-1}$). Subsequently, the associated electrochemical potentials to equation 2.38 can be computed by using equation 2.37 (Darnet et al. 2004). Further information can be found in the Appendix B.3.

Seismo-electric coupling

The seismo-electric phenomenon describes the coupling between electromagnetic and seismic disturbances in a porous media (Revil and Jardani 2013). It is an extension of the electrokinetic theory to the frequency domain. Two types of electrical disturbances are observed when a seismic wave travels through the porous material. The seismic wave propagation generates electrical current due to the displacement of the electrical diffusive layer as shown in Figure 2.12. All waves, the seismic and the co-seismic electrical signals, have the same speed. The amplitudes of the co-seismic electromagnetic signals are controlled by the properties of the porous material and by the properties of the pore fluid/solid interface (Gharibi et al. 2004).

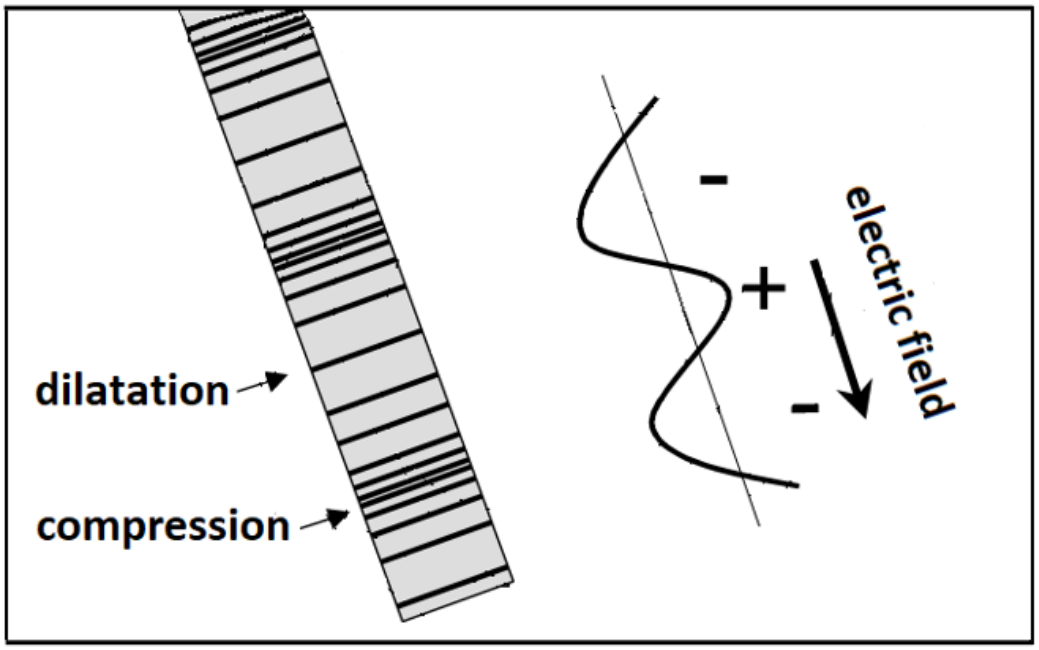

FIGURE 2.12: Compression seismic wave and its associated seismo-electric response in a homogeneous fluid-saturated porous medium, modified after Gharibi et al. (2004).

In addition to the co-seismic signals, a second phenomenon is generated when a seismic wave moves through a sharp interface characterized by a change in electrical or mechanical properties (Gharibi et al. 2004). A fraction of the mechanical energy is converted into EM energy producing a dipolar EM excitation (see Fig. 2.13). The EM disturbances diffuse very quickly and can be recorded by electrodes or antennas (Revil and Jardani 2013).

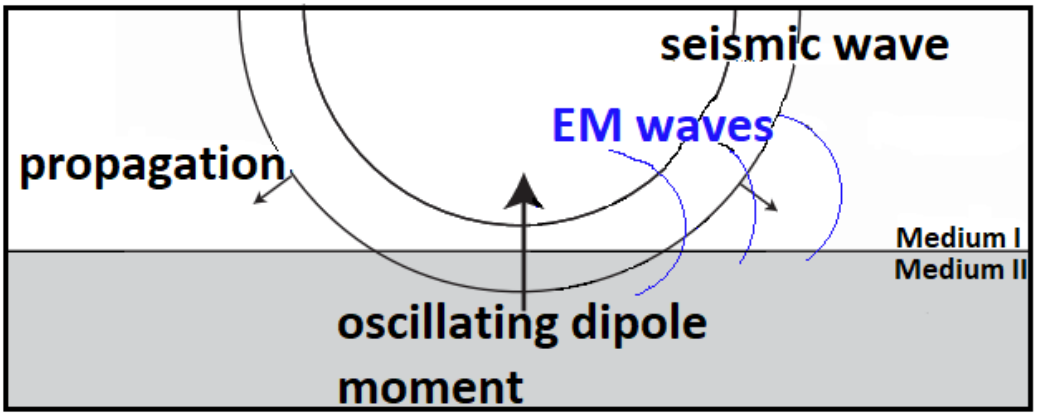

FIGURE 2.13: Time-varying electric dipole generated at the interface and its EM radiation, modified after Gharibi et al. (2004).

2.5 Summary

The electric resistivity was introduced at the beginning of the chapter and the factors controlling it. Moreover, the three methods of this thesis, MT, SP, and EMR, are introduced. MT is a passive electromagnetic method with a source

signal caused by variation in Earth's magnetic and electric fields by lightning and solar wind interactions. The EMR method is introduced as a second EM method in this thesis. The history of the EMR signals and a possible model explaining them are introduced and discussed. The last method, SP, is an electric method to measure the electric potential differences. The electric double layer as the basic idea of SP signals is introduced.

Chapter 3

Survey areas and data acquisition

The first part of this chapter introduces the experimental setup of the MT survey and the drilling of the well RN-15/IDDP-2. The second part of the chapter deals with the experimental setup in the Äspö HRL and the hydraulic fracturing procedure

3.1 RN-15/IDDP-2 in Reykjanes, Iceland

In 2004 the well RN-15 was drilled by the Icelandic company HS Orka to a depth of 2509 m. After the encounter of magma in the Icelandic deep drilling project (Elders et al. 2014), it was decided in the framework of Iceland deep drilling 2 to drill a well in Reykjanes. Thus, in 2016 and with the support of the European Union in the Horizon2020 project DEEPEGS (see DEEPEGS Office Reykjavik (2016)) the drilling of RN-15 continued from August 2016 until the end of January 2017. Since then, the well is known by the name RN-15/IDDP-2.

3.1.1 MT Experimental setup

A first field campaign took place in September 2016 to test eight stations to identify an optimal location for a continuous MT monitoring station concerning the station's expected electric noise and accessibility. A temporary remote station was operated in the region Höfuðborgarsvæðið, 20 km South of Reykjavik during this period. This remote station cannot be accessed during the Icelandic winter period when the target depth of the well was reached, and the main stimulation of the well occurred. For practical operation and maintenance regarding power supply, access to the station, data transfer, and for reasons of data comparability, the two continuous monitoring stations, GUN and RAH, were selected close to seismic stations.

Both stations are shown in Figure 3.1. The GUN station represents the main monitoring site. It is located about 750 m SE of the wellhead of RN-15/IDDP-2 well and beeline about 1 km to the E of the bottom of the well. The second MT station RAH was planned to operate as a second continuous monitoring station with the potential of being a local remote reference with a distance of 5 km from the wellhead (Haaf and Schill 2019).

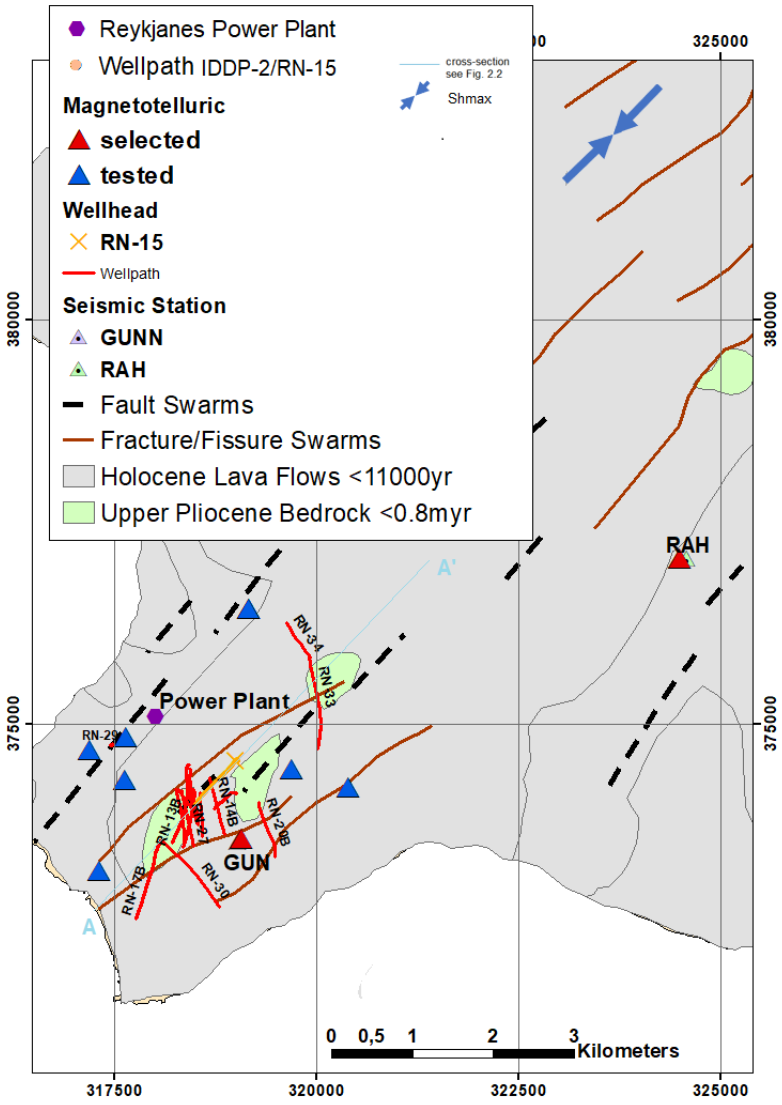

FIGURE 3.1: Geological map of the Reykjanes peninsula with the MT test (blue triangles) and monitoring stations (red triangles) and the Wellhead of RN15 (black cross) (Haaf and Schill 2021).

Both stations were deployed with a controlling unit ADU07e from Metronix Inc. (Elektronik GmbH 2019) to measure orthogonal and time-dependent components of the Earth's magnetic field and the corresponding electric response. The time series were measured by two horizontal electric components, E_x and E_y, and three magnetic components, H_x, H_y, and H_z. An exemplary MT site is shown in Figure 3.2. The three MFS07e coils were aligned perpendicular in north-south, east-west, and vertical directions, respectively. The electric horizontal dipoles were aligned with the horizontal magnetic coils in N-S and E-W direction, and non-polarizable electrodes were used. The coils and the cables were buried 10 cm deep to protect them from the weather.

At GUN, the continuous MT monitoring was carried out between November 30, 2016, and July 21, 2017. The sampling frequency was 512 Hz, and the

data was saved in 24-hour blocks. Due to continuing bad data quality after mid of December 2016, the measurements at RAH were stopped in May 2017. In total, the MT monitoring covers the last third of the drilling period of the RN-15/IDDP-2 well and the stimulation of the well. Due to a failure of the data logger, continuous data coverage lags at GUN during the workdays 117 - 119, 145 - 152, 155, 158, 161, and 164.

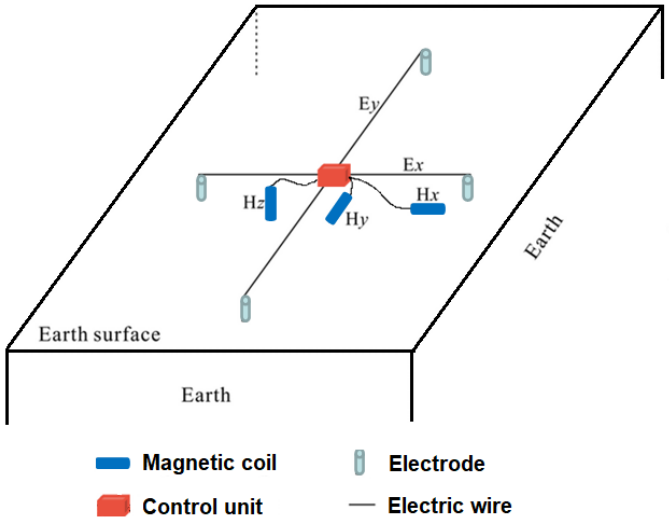

FIGURE 3.2: Exemplary field setup of a MT station with four deployed electrodes and three magnetic coils and the controlling unit, ADU07e, in the center.

3.1.2 Geophysical setting before drilling

Figure 3.3 shows a cross-section from earlier 3D MT modeling studies in the area of the Reykjanes geothermal reservoir (Karlsdóttir and Vilhjálmsson 2016). The model reveals a typical resistivity structure of a high-temperature geothermal system with a low resistive cap layer of up to 2 km thickness. In the vicinity of the well, vertical conductive structures indicate at a dyke swarm or a sheeted dyke complex as a heat source (G. Friðleifsson et al. 2014). The Reykjanes geothermal field is predominately covered by subaerial basaltic lavas and by hyaloclastite (Khodayar et al. 2017). The hyaloclastite date from the last glaciation and appears as ridges, rising from the surrounding rugged but relatively flat-lying lavas. The basaltic lavas are postglacial with an age of 12'500 years (Khodayar et al. 2017). The youngest lavas from the crater rows in the western part of the geothermal field are from the 13th century (Khodayar et al. 2017).

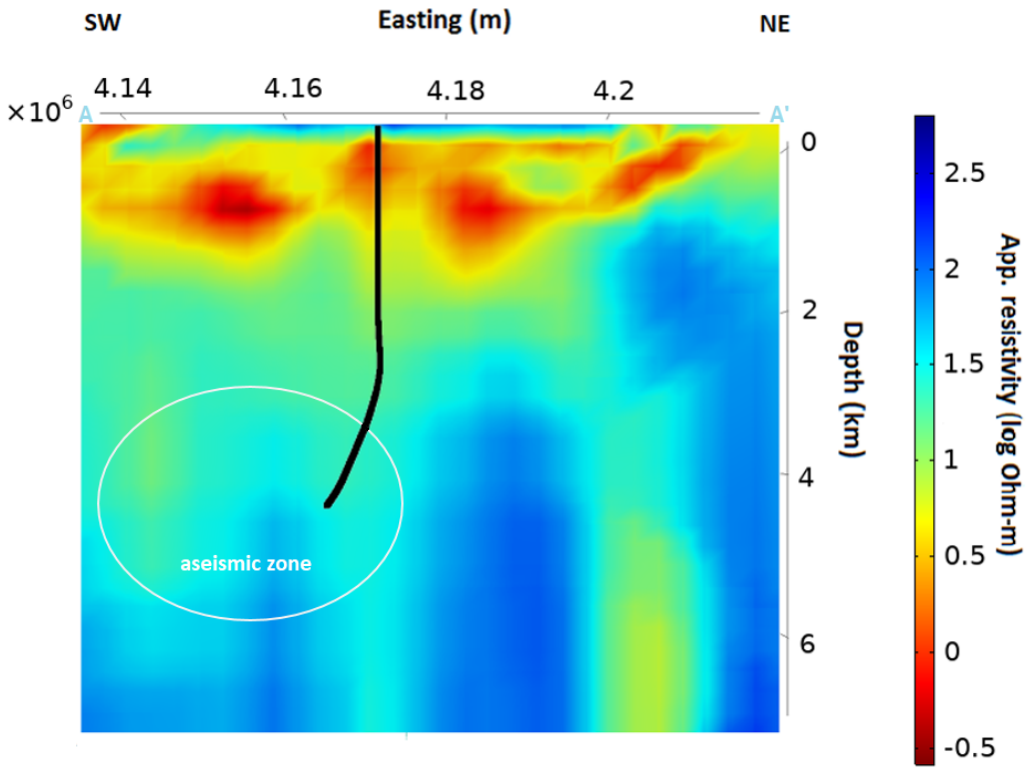

FIGURE 3.3: Cross-section of the 3D Inversion model by Karlsdóttir and Vilhjálmsson (2016) from Southwest to Northeast. The well path (marked in black) is not drawn true to scale (Haaf and Schill 2021). The white outlined area marks the aseismic gap.

Since 2013, the Iceland Geo Survey, ISOR, operated a dense seismic network around the Reykjanes geothermal field and recorded a total amount of 4850 earthquakes (Guðnason et al. 2015). The RN-15/IDDP-2 is extended into an aseismic zone with a vertical extension of 3 - 6 km depth (Figure 3.4). Guðnason et al. (2015) suggested that high temperatures close to the brittle-ductile boundary for normal strain rates could explain the lack of seismic activity. However, seismic activation of this zone at about 3 km depth is revealed by fluid injection into the well RN-33/34. Moreover, this zone has been seismically activated at a depth of about 3 - 4.5 km during the drilling operation of RN-15/IDDP-2 starting in August 2016. Both activation are illustrated in Figure 3.4 displaying two clusters of seismic events at the bottom of the two wells. Both wells are located within the epicenters of the 1680 earthquakes on the Reykjanes peninsular between December 2015 and November 2016 (Guðnason et al. 2015).

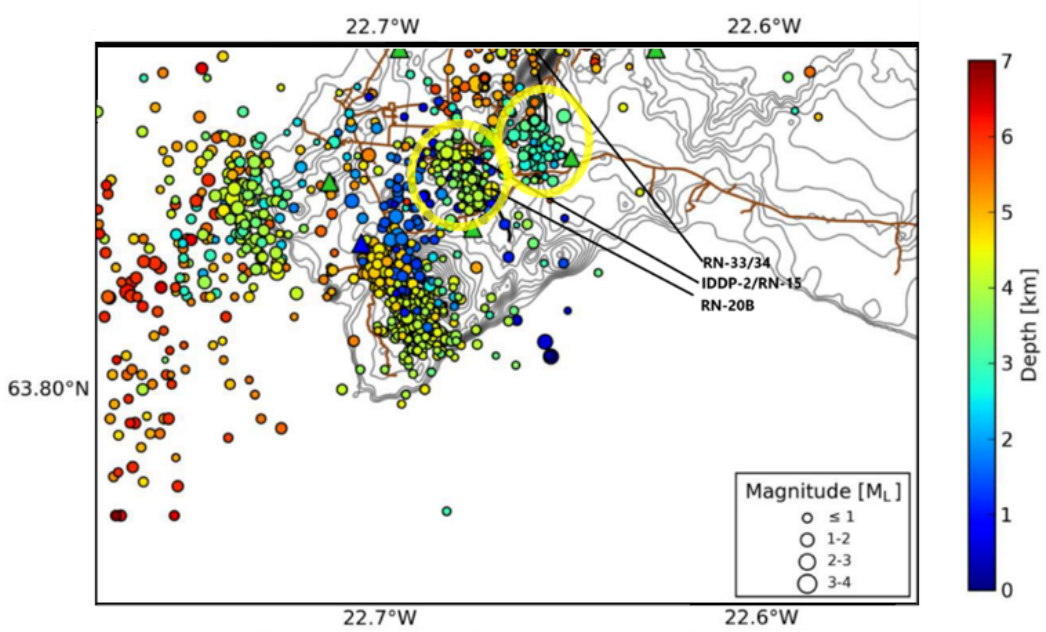

FIGURE 3.4: The location of Earthquakes from December 2015 until November 2016. The size and color of circles describe the magnitude and depth of earthquakes, respectively. Seismic network stations are marked with green triangles. The yellow circles marks the previous aseismic gap. Yellow crosses mark wellheads of the injection wells and of RN-15/IDDP-2. The black lines show their trajectories, modified after (Guðnason et al. 2016).

No increase in seismicity was observed during injection into well RN-20b. Similar results are in the vicinity of RN-34, whereas seismicity increased in deeper depths after injection stopped, but these events are not considered as induced ones (Guðnason et al. 2016). The injection into RN-33 between March and November possibly induced 84 earthquakes, mostly between 2.5 to 3.5 km depth. These depths are considered to be too shallow to activate the aseismic gap. Therefore, it is assumed that mainly the deep drilling operations at RN-15/IDDP-2 activated the former aseismic gap (Guðnason et al. 2016).

3.1.3 Drilling of geothermal well RN-15/IDDP-2

The deepening of RN-15/IDDP-2 was divided into three phases. The daily drill progress is shown in Figure 3.5. Phase 3 covers the drilling from 2'509 m down to 3'000 m, Phase 4 from 3'000 to 4'626 m, and phase 5 was drilled with a 6" drill bit from 4'626 to its final depth of 4'659 m. A steel casing was cemented firmly into the surrounding formation. Phase 3 finished with a production casing down to 2'941.4 m. During phase 3, circulation losses took place and continued in the other phases. Phase 4 had minor circulation loss at the beginning, which grew to total circulation loss throughout the drilling. Cementing jobs were stopped below 3'180 m, so no drill cuttings returned to the surface below that depth (see 3.9). Thus, it was blind drilling below 3'200 m until the final depth of 4'659 m. Phase 4 was completed with a 7" liner from 2'880.2 m down to 4'600 m and a sacrificial casing from the surface to

2'941 m. The bottom of the well has a vertical depth of 4.5 km and is situated 738 m southwest of the wellhead. The kick-off point is down at 2'750 m, where the well deviates in 220-degree SW direction with an inclination angle of 40 degrees (as seen in Figure 3.3). The well design can be found in the Appendix A.

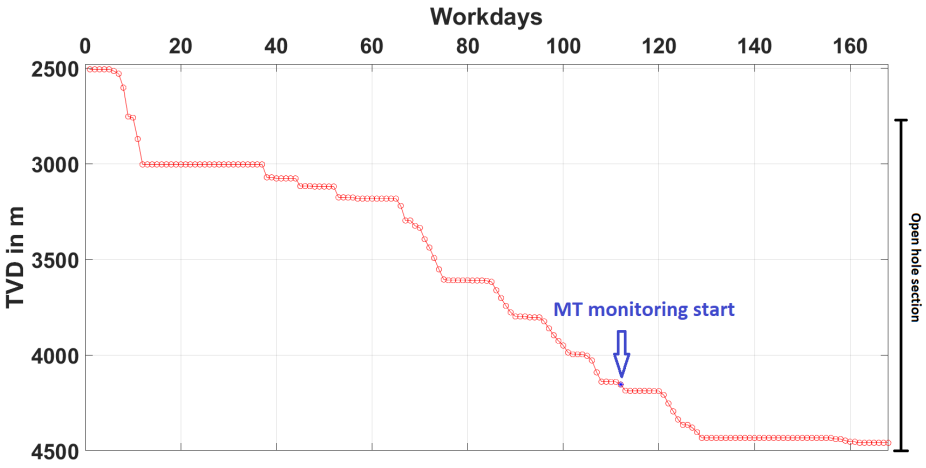

FIGURE 3.5: Daily drill progress (TVD = true vertical depth) along the workdays. Arrow marks the start of the MT monitoring (Haaf and Schill 2021).

Hydraulic and seismic observations during drilling and stimulation

Hydraulic and seismic observations during MT monitoring are summarized in Figure 3.6. Drilling took place on the workdays 112 - 163 and hydraulic stimulation on the workdays 164 - 169. The injection rates vary between 15 - 54 L/s until workday 116 (drilling and reaming down to a measured depth (MD) of 4'310 m). The next section, down to 4'537 m MD is drilled at injection rates of 0 - 40 L/s during workdays 121 - 126. The well reaches 4'626 m MD and fluid is injected with 15 - 54 L/s followed by 58 L/s between workdays 127 - 129. During logging (workdays 135 - 140), injection rates of 15-54 L/s are used. The final section is drilled down to 4'659 m MD at increasing injection rate ranges from a few L/s to 30 L/s to 20 - 40 L/s (workdays 155 - 164).

During drilling, total or nearly total fluid losses occurred during the workdays 113 - 114, 122 - 125, and 128 - 132. The latter two are linked to the occurrence of induced seismicity with magnitudes up to M = 1.7. The number of seismic events in 24-hour windows distinguishes between windows with two or more events with a magnitude M > 1 (red in Figure 3.6) and windows with one or less events of this size (green in Figure 3.6).

Pressurization and thermal cycling were performed to improve the well injectivity. The injection rates were raised in short steps to 110 - 115 L/s using rig pumps and then decreased to zero for a quick warm-up. The injectivity of the well improved from 1.7 L/s/bar at the end of the drilling to 2.9 L/s/bar during the stimulation to final 3.1 L/s/bar at the end of this stimulation stage (Sigurðsson 2018).

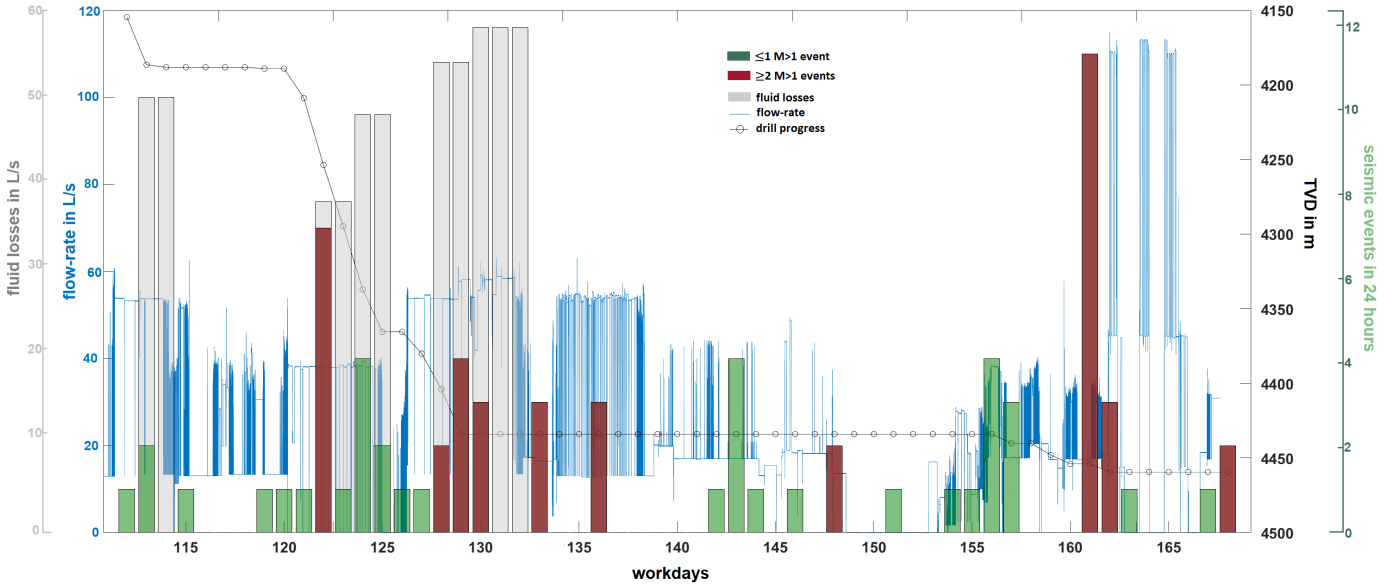

FIGURE 3.6: Injection rates into RN15/IDDP-2 (blue lines), total or nearly total fluid losses in 24-hour windows (grey bars), and induced seismicity in 24-hour windows (green and red bars, modified after Gaucher, pers. comm.) during the MT monitoring from 30/11/2016-26/01/2017 (Haaf and Schill 2021).

Note that all experiments were carried out using freshwater at a conductivity of 15'120 μS/cm from groundwater well at a distance of about > 1.5 km from the drill site. This translates to a fluid resistivity of about 0.66 Ωm. In case the injected volume would be large enough to cause any effect on the bulk resistivity, injection into the present matrix with a resistivity of 10 - 100 Ωm (Figure 3.3) would result in a no or an only a slight change in the decrease in resistivity.

The maximum seismic activity during the MT monitoring period is reached on workday 161 with eleven events followed by seven events on workday 122, both days with at least two events with M > 1. On workday 122 drilling was resumed at injection rates up to 40 L/s. The next period of important seismicity started on workday 128 and lasted until 136. This phase corresponds to comparatively high injection rates of up to 58 L/s and moreover relatively high lower limits of up to > 40 L/s. During the period of maximum seismic activity, injection reach a local maximum of 40 L/s. Interestingly, during the hydraulic stimulation significant seismic activity occurs only at the beginning of the third of three injection cycles. During the entire drilling period (August 2016 to January 2017), a number of 357 earthquakes with magnitudes between 0.5 to 2.02 occurred in the depth range of 2 - 5 km close to the borehole (see Figure 3.4). The increasing depths of the hypocenters are attributed to the drilling progress.

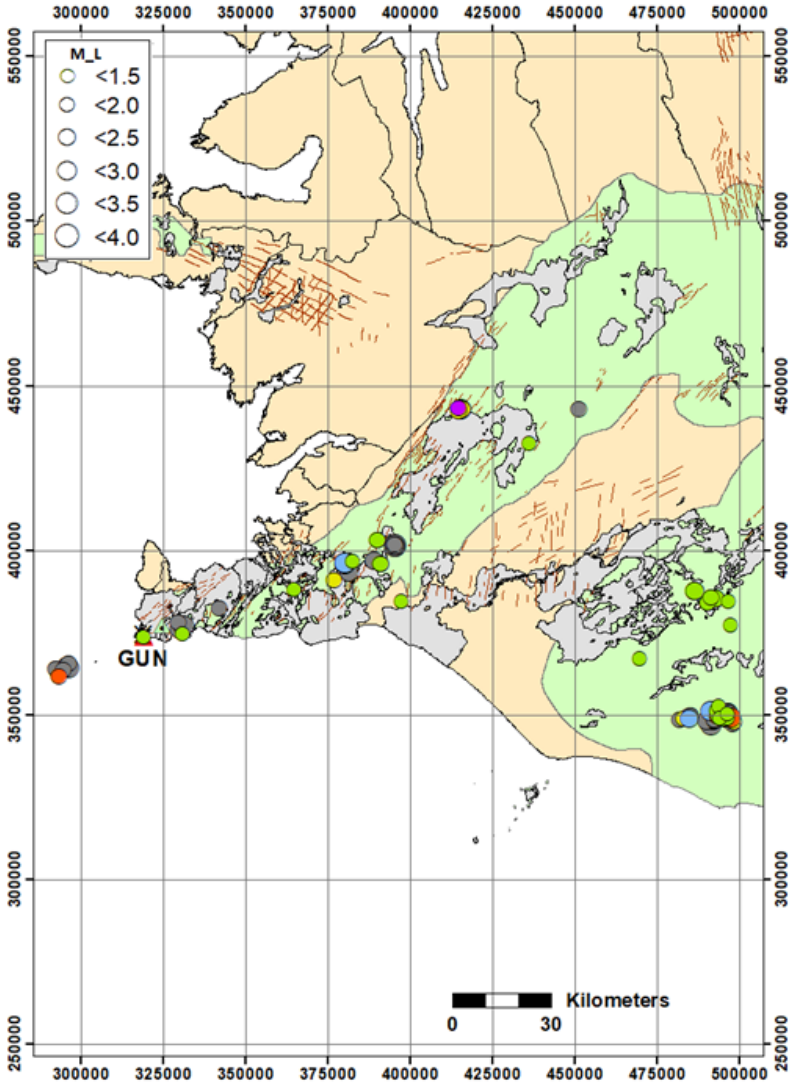

FIGURE 3.7: Local and regional seismicity on the Reykjanes peninsular (ML>1.66) during the MT monitoring period 30/11/2016-26/01/2017 and seismic events with ML < 4.0 from the SIL network (Icelandic Meteorological Office 2017). The events of case 1 are plotted in yellow, case 2 in blue, case 3 in violet, case 4 in orange, case 5 in green and all events not related to the cases in grey. The size of the circles corresponds to the magnitude ranges (Haaf and Schill 2021).

In Figure 3.7, an overview is provided of the local (see Figure 3.6) and the regional seismicity in Iceland (Icelandic Meteorological Office 2017). During the MT monitoring period, regional seismicity in SW-Iceland reveals seismic events with magnitudes of up to $M_L = 3.6$. Note, that the events are clustered in workday intervals in Figure 3.7. This step provides a better basis for the following sections and discussion. Case 1 includes the workdays 157-163 in yellow, case 2 112-115 in blue, case 3 133 - 137 in violet, case 4 126 - 130 in orange, case 5 136 - 143 in green and all event outside of these intervals are plotted as grey circles. The magnitude defines the size of the circles. Several

regional events exceed the local magnitude of $M_L = 1.7$ (see Figure 3.6).

Temperature and pressure profile

A temperature and pressure log was accomplished on workday 146 (January 3rd, 2017), in the 7″ liner down to 4'560 m. The results are displayed in Figure 3.8. During logging down in the well, the pumping rate was changed from 15 to 35 L/s at 500 m, and to 40 L/s at 682.5 m depth. Feed zones can be located in a depth of 3'400 m, 4'200 m, 4'375 m, and 4'550 m. Down near bottom (4'560 m), the temperature reached 426 °C degrees and a pressure of 340 bar. The critical point of fresh water occurs at 373.946 °C degree and 220.64 bar (Wagner and Pruß 2002). The reservoir fluids currently produced from the Reykjanes field have a salinity of seawater, which has a critical point of 406 °C degree at 298 bar (Bischoff and Rosenbauer 1988). Therefore, the conditions at well bottom of RN-15/IDDP-2 reached the super-critical level (Friðleifsson et al. 2017).

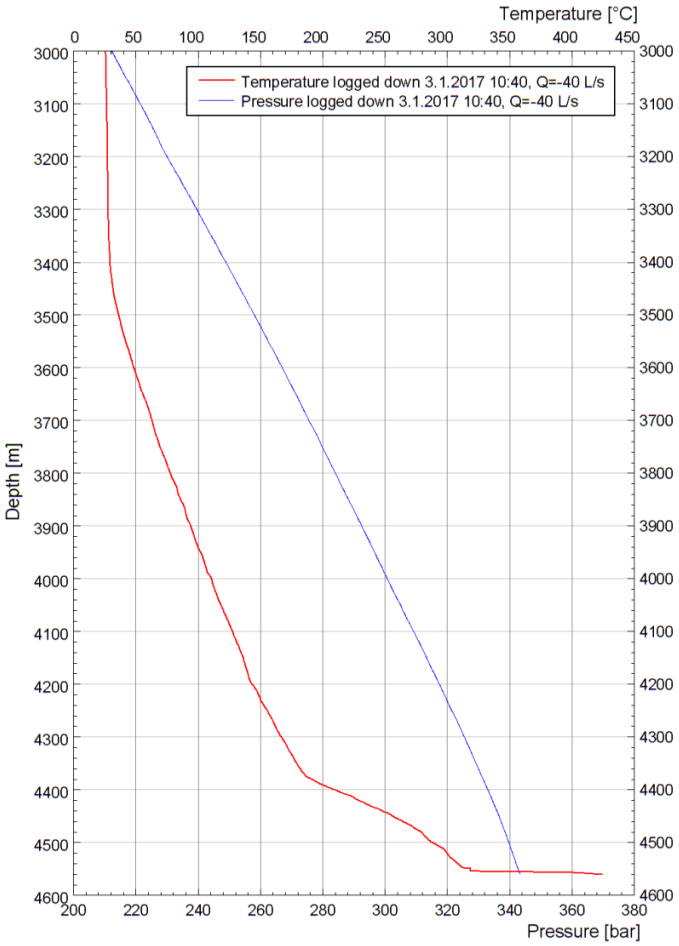

FIGURE 3.8: Temperature and pressure logging on 3 January in 7″ liner (Weisenberger et al. 2017).

Lithology and Alteration

An overview of the distribution of alteration minerals and the lithology in well RN-15 is presented in Figure 3.9 for the depth range from 800 m to 2'507 m on the left side and from 3'000 m to well bottom on the right side.

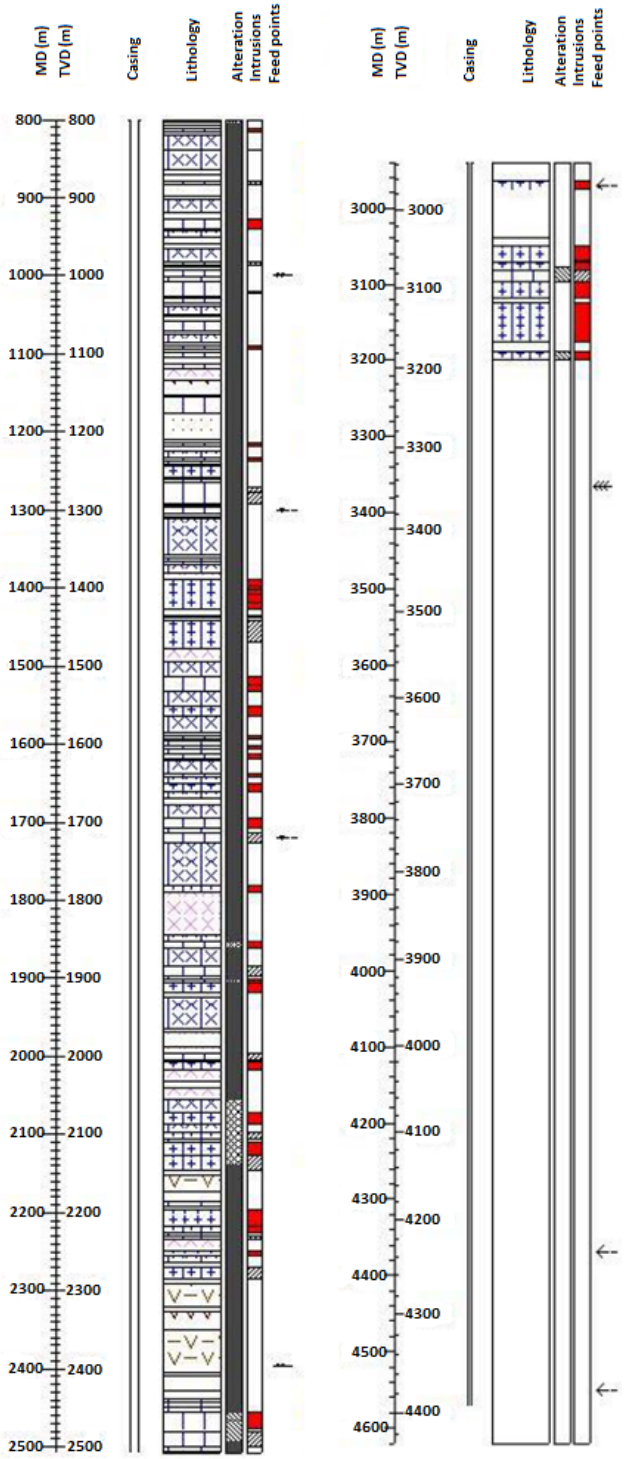

FIGURE 3.9: Lithology and alteration information from 800-2500 m and from 3000-4600 m of RN-15/IDDP-2, modified after Weisenberger et al. (2017).

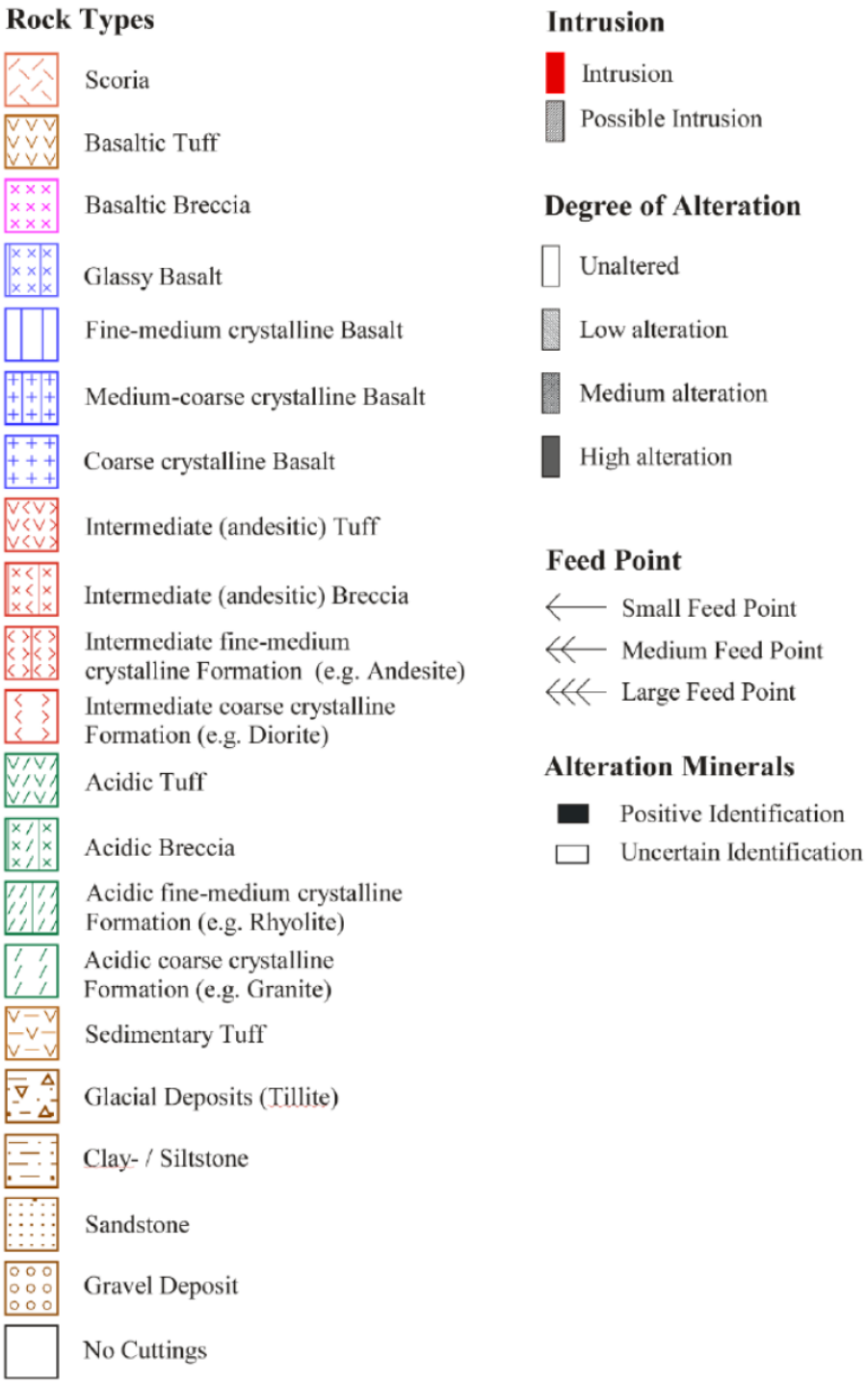

FIGURE 3.10: Legend of lithology and alteration shown in Figure 3.9 (Weisenberger et al. 2017).

The corresponding legend is shown in Figure 3.10. The information about alteration and lithology of the well RN-15/IDDP-2 are summarized from the drilling reports, (Weisenberger et al. 2017), which were kindly provided from the Icelandic GeoSurvey ISOR within the project partners.
No information about the alteration minerals and the lithology is available within the continuation of phase 3 of drilling (2'509 - 3'000 m). Due to the

total loss of circulation during the drilling of well RN-15/IDDP-2, no drill cuttings were retrieved below 3'200 m. The lithology is mainly based on fine-to medium-grained and medium-to coarse-grained basalt (Weisenberger et al. 2017). In between layers are mostly basalt and sedimentary tuff, glassy basalt, and basalt breccia.

A regular progressive hydrothermal alteration with increasing depth was noticed in well RN-15/IDDP-2 (Weisenberger et al. 2017). It has a typical mineral assemblage with low-temperature minerals, like fine-grained clay (smectite) and zeolites, at shallower depths. High-temperature minerals, like epidote and coarse-grained clay (chlorite), appear at deeper levels in the well (Weisenberger et al. 2017).

Geological information below 3'200 m depths is solely based on the retrieved core runs (see Table 3.1). Although a total of 13 core runs were carried out, the minimal core recovery, cannot provide representative information about the deeper lithology (Friðleifsson et al. 2017). The core runs only cover in total 27.31 m.

TABLE 3.1: Overview of the core runs in RN-15/IDDP-2 (Friðleifsson et al. 2017).

Core run	Start	Coring interval (m)	Cored length (m)	Drilling time (h)	ROP ($m\,h^{-1}$)	Core recovered (m)
1	18/09/2016	3068.7–3074.1	5.4	7.12	0.8	
2	04/10/2016	3177.6–3179.0	1.4	2	0.7	
3	30/10/2016	3648.0–3648.9	0.9	5	0.2	0.52
4	02/11/2016	3648.9–3650.7	1.8	10.25	0.2	
5	11/11/2016	3865.5–3869.8	4.3	8.5	0.6	3.85
6	12/11/2016	3869.8–3870.2	0.4	2.5	0.2	0.15
7	22/11/2016	4089.5–4090.6	1.1	2.25	0.5	0.13
8	28/11/2016	4254.6–4255.3	0.7	5.5	0.1	0.28
9	06/12/2016	4308.7–4309.9	1.2	3	0.4	
10	07/12/2016	4309.9–4311.2	1.3	8.25	0.2	0.22
11	16/01/2017	4634.2–4642.8	8.6	1.25	6.9	7.58
12	17/01/2017	4642.8–4652.0	9.2	1	9.2	9
13	19/01/2017	4652.0–4659.0	7	0.75	9.3	5.58
Total			43.3			27.31
					Core recovery about	63 %

Table 3.2 gives an overview at which depth the minerals first appear. The production casing was extended into the geothermal reservoir, where an excess of epidote was noticed in the cores. Epidote and chlorite were not found in cores deeper than core 5. Calcic-plagioclase and hornblende were discovered in deeper cores. In addition, biotite was found in core 8 and 11 at depths of 4'255 m and deeper. Biotite is usual found in high temperature alteration of intermediate to felsic rocks, whereby biotite alteration is unusual in low K tholeiitic basalts (Friðleifsson et al. 2017). A detailled analysis of the the core runs can be found in Weisenberger et al. (2017) and Friðleifsson et al. (2017).

TABLE 3.2: Overview of the alteration minerals and their first appearance (Jónsson et al. 2010).

Alteration mineral	Depth (m)
Quartz	650
Epidote	710
Wollastonite	928
Actinolite	1560
Garnet	1378
Biotite	4255
Calcite disappearance	1000
Epidote disappearance	3869

Supercritical conditions at well bottom of RN-15/IDDP-2

Friðleifsson et al. (2017) confirmed that the well reached supercritical conditions at the bottom of the well with a measured temperature of 427 °C and a pressure of 340 bar (see Figure 3.8). The critical points for water are temperatures > 374 °C and pressures > 221 bar and for seawater > 406 °C and pressures > 298 bar (see Figure 3.11), since the production fluid from the Reykjanes geothermal field is seawater modified by reactions with basalt at high-temperatures (Fridriksson et al. 2015).

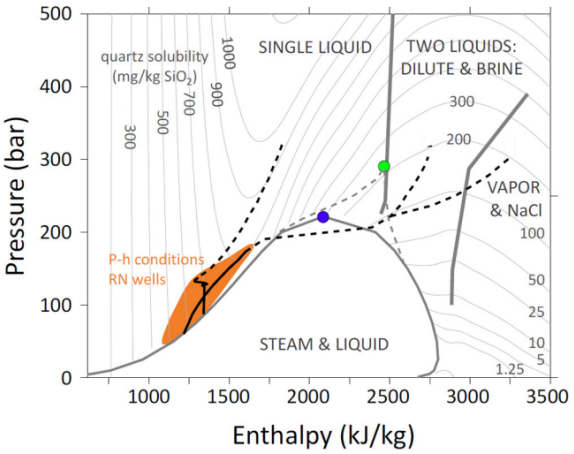

FIGURE 3.11: Phase diagram for H_2O in terms of pressure and enthalpy with superimposed quartz solubility as gray contour lines. The labeled phase fields are for pure water. The phase fields for a 3.5 % NaCl-H2O system (Reykjanes fluids approximates seawater) would have similar shape and pass through the critical point for seawater (single liquid, dilute fluid/brine, and vapor/solid NaCl). The critical points for pure water and seawater are the blue and the green symbols, respectively. The brown shaded area represents the pressure-enthalpy regime found in the geothermal reservoir feeding the existing production wells at Reykjanes, modified after Friðleifsson et al. (2020).

The temperature profiles (Figure 3.12) are based on measurements during a weeklong heat-up interval (23.-29.5.2017), on estimated formation temperature (black) by Hokstad and Tanavasuu-Milkeviciene (2017), on pre-drilling temperature estimate (violet) by Fridriksson et al. (2015) and a boiling point with depth (BPD, green) curve for seawater assuming a water table at 450 m depth. The star symbols indicate formation temperatures based on Horner plot estimates from warm-up temperature logs. The temperature log shown in Figure 3.8 is also included in Figure 3.12.

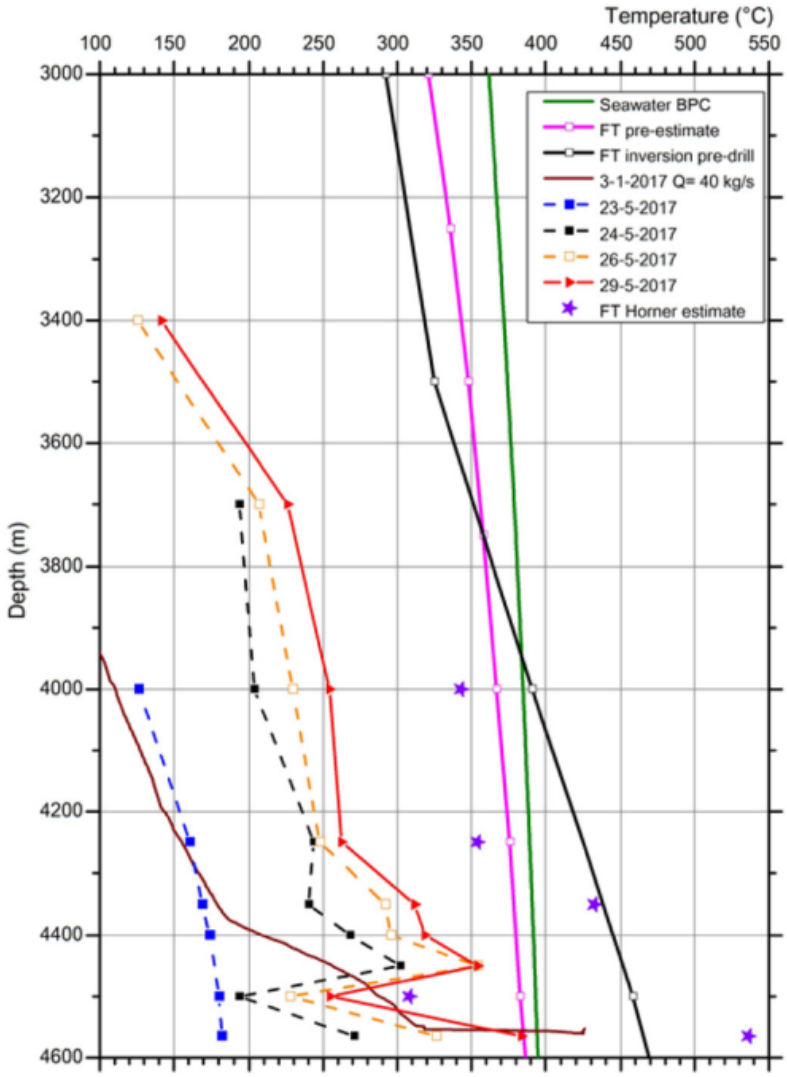

FIGURE 3.12: A compilation of several temperature profiles (B) including the one from Figure 3.8. The temperature logs were measured on the 23d, 24th, 26th, and 29th May 2017. The three T profiles shown by black, violet and green solid lines represent estimated formation temperatures, a pre-drilling temperature estimate based on an extrapolated T-gradient in RN-15, and a boiling point with depth (BPD) curve for seawater. The purple stars indicate formation temperatures based on Horner plot estimates from the warm-up temperature logs (Friðleifsson et al. 2017).

The highest estimation from the Horner plots is approximately 535 °C at

4'615 m. The black line curve passes the 374 °C at a depth of 3'900 m and the 406 °C at about 4'150 m. Only the temperature logs from 3.1.2017 and 29.5.2017 pass or stop at about 374 °C. Therefore, it is not conclusive at which depth the supercritical conditions start.

Taking the core runs into account, Figure 3.13 shows a piece of the drill core 11 from 4'634.2 - 4'642.8 m. The felsite veins and also conjugate sets of older fractures and veins are visible. The mixing of supercritical vein fluid causes the red color of the felsite with cold oxidizing drilling fluid (Friðleifsson et al. 2017). Therefore, at least at depths of 4'634 m, the well encountered the supercritical fluid.

FIGURE 3.13: A piece of core 11 from 4'634.40 to 4'634.55 m depth. It shows felsite veins and conjugate sets of older fractures/veins. The mixture of supercritical vein fluid with cold oxidizing drilling fluid causes the red color of the felsite (Friðleifsson et al. 2017).

The question remains if it is possible to see the supercritical conditions in the MT data. Temperature > 300 °C causes an increase in electric resistivity (see Figure 2.3b). Pressure values < 500 bar might cause an increase in resistivity of about 30 Ωm or more. Moreover, the chlorite-epidote zone at depth (see Figure 2.6) could lead to a decrease in resistivity. However, the core samples showed that neither chlorite nor epidotes were found in cores deeper than core 5 (3'865.5 - 3'869.8 m, see Table 3.1 and 3.2). Subsequently, the increasing temperature might cause an increase in resistivity at areas deeper than that zone (> 300 °C, see Figure 2.3b). Taking measured data from the area into account, Figure 3.3 shows resistivity values between 20-100 Ωm at a depth > 4 km. The measured temperature logs and core examples show that the well encountered supercritical conditions only at the last meters before the well bottom. Therefore, the alteration minerals and the lithology seem to be the main contributors to the resistivity increases at 4 - 5 km depth. However, it cannot be distinguished for depths > 5 km since different factors cause increases in resistivity here (temperature, alteration, supercritical conditions).

3.2 Äspö Hard Rock Laboratory

Hydraulic fracturing experiments were performed in the underground lab in Äspö, SE Sweden. The hard rock laboratory (HRL) is located on the Äspö island with an underground extension down to 460 m in the bedrock. It is located in the Transscandinavian igneous belt of Svecofennian orogen. A 1.8 Ga old intrusive rocks of granite, syenite, diorite, and gabbro dominate the bedrock (Zang et al. 2017). The HRL was installed in 1986 with a focus on the development of methods for final disposal of spent nuclear fuel.

Figure 3.14 gives an overview of both the entire tunnel system and the on the surface located additional research facilities such as bentonite laboratory (Zimmermann et al. 2019). The access to the 3'600 m long tunnel system is from the Simpevarp peninsula to the southern part of the island, and it continues in a spiral shape in the subsurface. A boist shaft and two ventilation shafts are the connections between tunnel and surface (Kärnbränslehantering 2016).

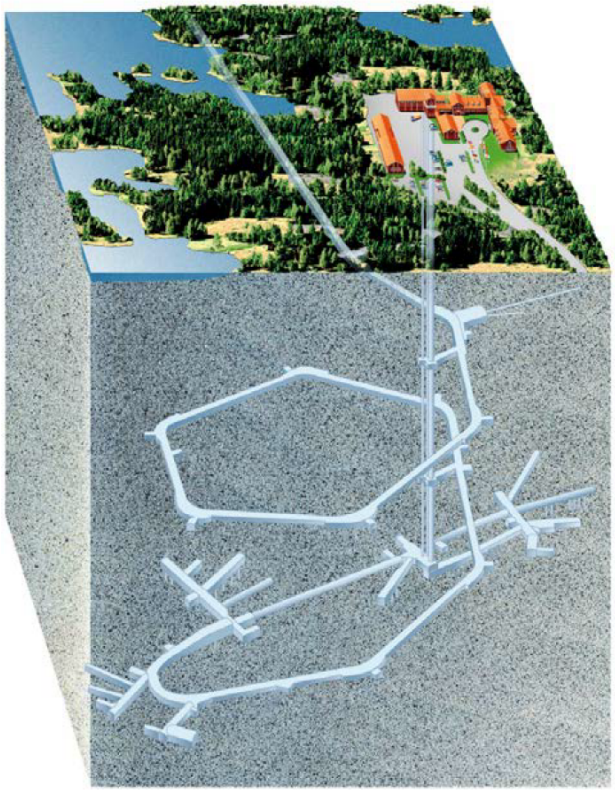

FIGURE 3.14: Schematic sketch of the Äspö hard rock laboratory by the (Kärnbränslehantering 2016).

3.2.1 Hydraulic fracturing procedure

The two discussed hydraulic fracturing experiments are summarized in Table 3.3 including the hydraulic data and the acoustic emissions (AE). HF2 is a hydraulic fracturing test with the conventional injection style, HF3 with a progressive one. The test procedure is as follows (Zang et al. 2017; Zimmermann et al. 2019). First, the test interval is enclosed of packer elements.

The pressure increases until the fracture breakdown pressure is reached and then declines. Then, the interval is shut-in, and the pressure drops. Next, the instantaneous shut-in pressure is measured. Finally, the injection pressure is released, and the fluid is recovered. After this main fracturing cycle (MF), the procedure is repeated to obtain the fracture reopening pressure 4 - 5 times in the refrac cycles (RF). The MF for HF2 is a conventional test with a constant flow rate until the fracture breakdown pressure is measured (see Figure 3.15a).

The MF for HF3 is reached by the so-called *fatigue hydraulic fracturing* (FHF). The fluid injection is in pressure cycles with increasing target pressure and with depressurization phases (see Figure 3.15b) for relaxing the crack tip stresses (Zang et al. 2019). The following RF cycles are conventional, as in HF2.

Both experiments took place in Ävrö granodiorite rock. The fracture breakdown pressure P_c is 10.9 MPa in HF2 and 9.2 MPa in HF3. The reopening fracture pressures P_r are between 6.7 - 8.8 MPa for HF2 and 5.9 - 8.8 MPa for HF3. During HF2 injection, about a third of the injected volume was recovered. In contrast to HF3, where only a few percent of the injected volume was recovered. The permeabilities are larger for all RF cycles of HF2 compared to HF3, with values up to $4.78 \cdot 10^{-15}\ m^2$. A detailed description of the injection types and procedures can be found in Zang et al. (2017) and Zimmermann et al. (2019).

TABLE 3.3: Overview of the hydraulic and seismic data of HF2 (conventional) and HF3 (progressive) experiments. P_c is the fracture breakdown pressure, and P_r is the fracture reopening pressure. V_{inj} and V_{re} is the injected and returned volume, respectively. Q_{mean} is the mean flow rate (Zang et al. 2017; Zimmermann et al. 2019).

HF stage	Mid test interval (m)	P_c or P_r (MPa)	K (10^{-15} m^2)	Number of AE Events, continuous catalog with M_{AE}	V_{inj} (l)	V_{re} (l)	q_{mean} (l/min)
HF2-MF	22.5	10.9	1.32	192	3.8	1.1	1.7
RF1		6.7	3.63	230	5	1.9	1.7
RF2		7.5	3.37	3	1.2	0.6	2.5
RF3		8.6	2.68	287	5.5	2.3	2.5
RF4		8.8	2.97	233	4.8	2.3	4.8
RF5		8.2	4.78	628	9.4	3.9	4.8
Sum				1577	29.7	12.1	
HF3-MF1	19.0		0.211	0	0.11	0	0.94
HF3-MF2			0.181	0	0.12	0	0.95
HF3-MF3			0.146	0	0.14	0	0.93
HF3-MF4			0.464	0	0.14	0	0.61
HF3-MF5		9.2	0.429	0	0.13	0	0.47
RF1		8.8	0.76	70	3.3	0.3	1.6
RF2		5.9	1.23	96	5.2	0.3	2.5
RF3		7.7	1.08	115	5.6	0.8	5.3
RF4		5.9	1.97	325	10.5	1.8	5.3
Sum				606	25.23	3.2	

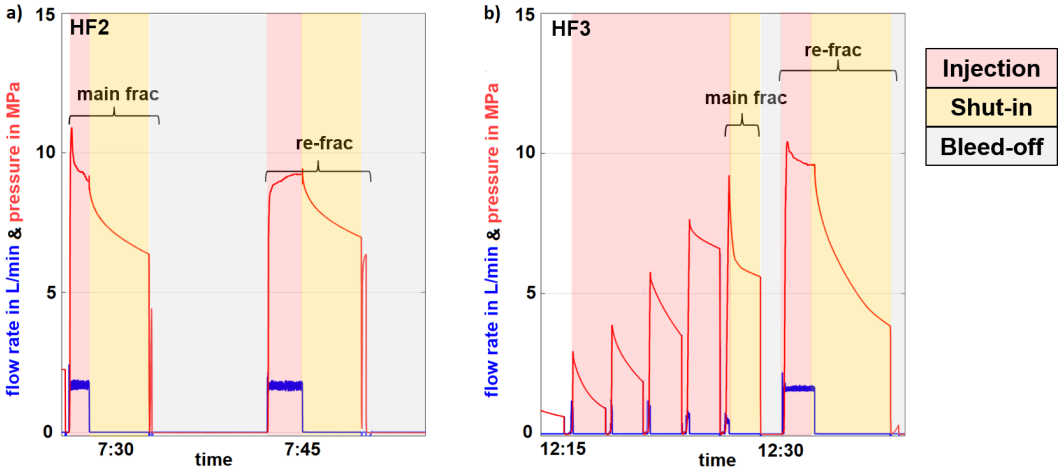

FIGURE 3.15: Exemplary sketch of a) conventional and a b) progressive HF injection protocol. The flow rate is shown in blue; the injection pressure is in red, modified after Zimmermann et al. (2019) and Niemz et al. (2021).

3.2.2 Experimental setup

A horizontal HF borehole, F1, was drilled from the tunnel TASN on level 410 m, as shown in Figure 3.16. Three additional monitoring boreholes (M1-M3) were drilled with a positive inclination of 10°, 26°, and 4°, respectively. A huge hydrological conductor with an outflow of up to 75 L/s is located in the boreholes, hence only upward oriented sensor installation in the boreholes (Zang et al. 2017). All boreholes are sub-parallel to minimum horizontal stress direction; thus, the expected fracture plane is assumed to be perpendicular to the borehole direction and parallel to horizontal stress (Zang et al. 2017).

F1 is 28 m long with a diameter of 102 mm. It is divided into six test intervals for three continuous and 3 HFH experiments, respectively. On level 410 m (near field) 11 AE sensors (3.16 orange dots) and four accelerators (3.16 red dots) for in situ stress measurements are deployed in M1-M3. Two SP chain were used (3.16 blue dots and squares) on both level, (borehole) geophones and broadband seismometers (3.16 green, light blue and black dots and squares, respectively) and two EMR sensors (3.16 magenta dots) parallel (130 °N) and perpendicular (40 °N) to fracture plane, respectively. The parallel and the perpendicular EMR sensors are deployed at a distance of 25 and 15 m from mid-test intervals, respectively. The SP electrodes have an offset of 5 - 10 m in the near field at a distance of 50 - 75 m from F1 and a distance of 150 - 200 m from F1 with 5 - 20 m offset in the far field.

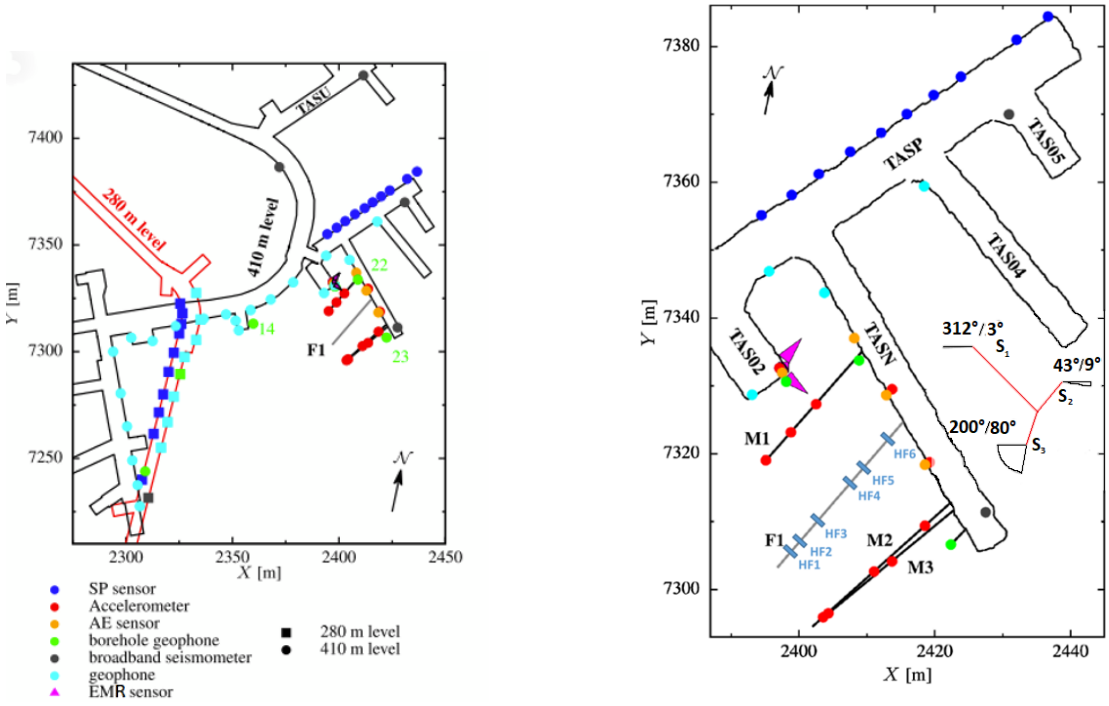

(A) (B)

FIGURE 3.16: Sensor Layout with a) far and new field and b) focus on the near field. The SP electrodes are shown as blue circles and squares, EMR as magenta triangles. The accelerometers are shown in red circles, the AE sensors in orange, the borehole geophones in green, the broadband seismometers in black, and the geophones in light blue circles. The boreholes are tagged as F1 and M1-M3, the tunnels as TASN, TAS02, TAS04, TAS05, and TASU, modified after Zang et al. (2017).

The detailed experimental setup of the operating systems is shown in Figure 3.17. The test interval is enclosed of the packer elements and next to the steel tubing. The coil tubing is connected via the pressure control panel to a digital data acquisition unit and the HP pump.

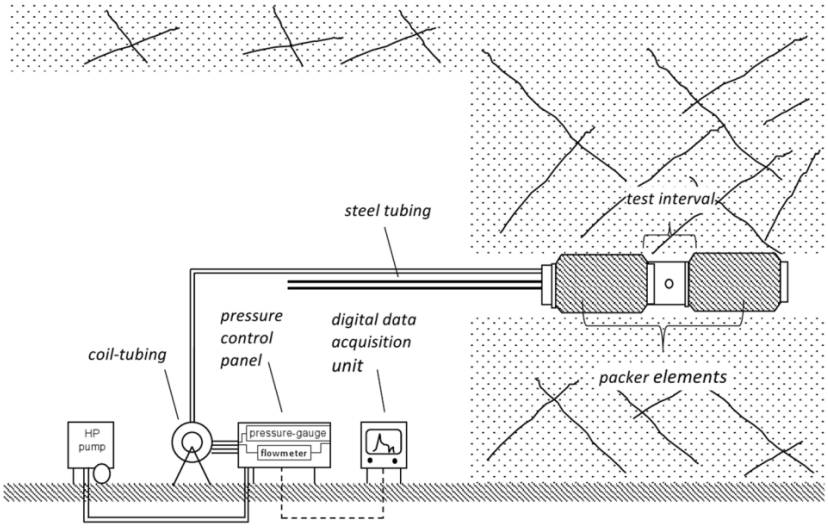

FIGURE 3.17: Schematic sketch of the experimental setup of the HF experiments with the test interval with the packer elements, the pressure control, data acquisition unit and the coil tubing (Zang et al. 2017).

3.2.3 Self-potential measurements

The SP data were recorded in 24-hour windows using non-polarizable electrodes (Pb/PbCl 2 PMS9000 by SDEC, France) filled with NaCl saturated solution and at a sampling frequency of 1 Hz. The electrodes were fixed and coupled in 0.25 m long boreholes with bentonite to the massive granite. The data logger was a CR-6 data logger from Campbell Scientific.

3.2.4 EMR measurements

The EMR data are recorded with a receiver (Cerescope) developed by the company Ceres GmbH in collaboration with Greiling and Obermeyer (2010) (see Figure 3.18). It consists of a 30 cm long beam antenna/ferrite aerial, an analog/digital converter, a digital logic circuit, a data memory (RAM), and a RS 232 interface for data transfer. For monitoring the acoustic, a headphone can be used for reception. The measurements can be performed in three directions (x and y = horizontal, z = vertical) to determine the direction of the largest principal stress σ_1 or smallest principal stress σ_3 (Lichtenberger 2006). The amplification range is between 90 and 120 dB resulting in a sensitivity of 5 μAm^{-1}. The length of a measurement is 0.1 s. First, the input signals are registered and stored for 100 ms, followed by a subsequent period of signal processing of 900 ms with adjustable low-, high, and band-pass filters to diminish narrow and wide-banded noise signals (Greiling and Obermeyer 2010). During that short interval, the electronic will be turned off to avoid signal biasing. Afterward, the electronic is switched on again.

In addition, the gain, the discrimination level, and the frequency range are adjustable. The Cerescope uses a burst averaging technique meaning it only measures the signals above the discrimination line. Therefore, the background noise is avoided. The Cerescope measures the EM signals between 5 - 50 kHz and depicts them in 4 parameters (A - D): A, the number of pulses,

B, the number of pulse packages (burst), C, the average amplitude of the burst, and D, the burst energy.

FIGURE 3.18: The Cerescope measuring unit with an aerial sensor and headphones (Greiling and Obermeyer 2010).

In the following, the burst energy (parameter D) is the preferred parameter in this study. It depends not only on the number of bursts but also on their amplitudes; therefore, it is less affected by possible background noise. The quantity is dimensionless. In this study, the frequency range was 35 - 50 kHz, the gain was set to 3 and the discrimination lines were between 24 - 28 for 130° sensor and 36 - 44 for the 40°. All data are band-pass filtered.

3.2.5 Acoustic emissions

The seismic and AE data were discussed by Zang et al. (2017) and Zimmermann et al. (2019) and Niemz et al. (2020) and kindly provided for our analysis. The AEs were measured with in-situ sensors between 1 - 100 kHz and accelerometers with 50 Hz – 25 kHz. The micro-seismicity and the geophones cover the frequency ranges from 1/120 up to 1 kHz (Zang et al. 2017). The AE results are obtained from a trigger system and a rapid analysis of event location (Zang et al. 2017). In total, 196 AE were detected during the entire experiment, with 102 events during HF2 and 16 during HF3. Recently, Niemz et al. (2020) published an AE catalog obtained from the continuous AE monitoring setup (Figure 2.1). The data were processed with a semi-automated workflow relying on full waveform-based detection, classification, and location procedures (Niemz et al. 2020). As a result, the AE catalog increased from 196 triggered events in previous studies to more than 19'600 AE events. The results by Niemz et al. (2020) are based on 4'302 events with estimated magnitudes. The magnitudes are estimated using maximum amplitudes across the network (Niemz et al. 2020). Here, the AE events will be included in the results chapter.

Figure 3.19 shows the fracture planes for each cycle of all six experiments. The fracture planes of HF2 have similar strikes and dipping angles, and therefore a stable orientation. The strike varies between 109 - 124° and the dip between 31 - 65° throughout HF2 (Niemz et al. 2020). For HF3, varying strike planes with steep dipping are observable for the first cycles, and moderately dipping values for the last two cycles. Moreover, the second set of planes

are like those of HF2 with less steep dipping. Hence, during HF2, a planar, elongated fracture plane is generated with stable orientations throughout the cycles (Niemz et al. 2020). In contrast to that, the authors assumed a more complex fracture pattern in HF3.

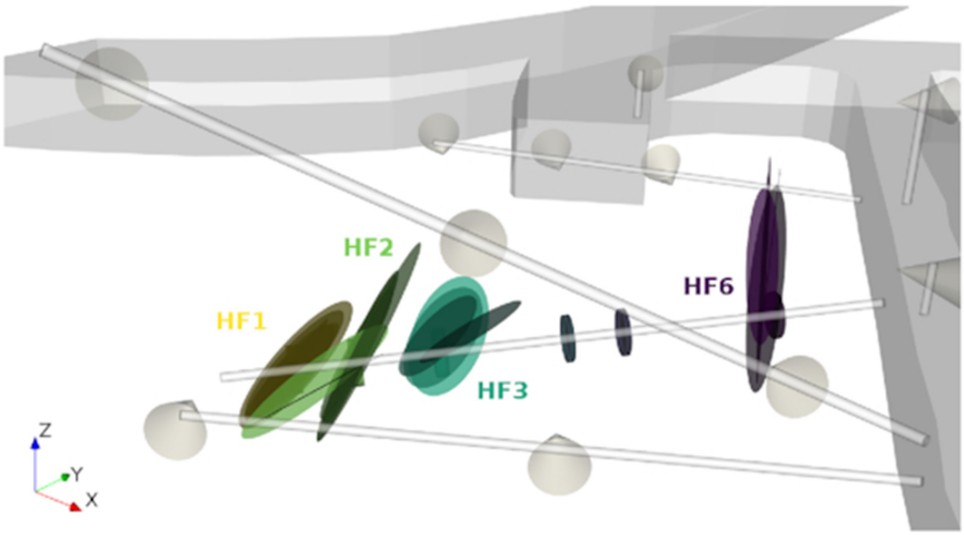

FIGURE 3.19: The fracture planes for the single cycles estimated from the AE cloud using the algorithm described in Niemz et al. (2020). The darker the color of the planes the more zones are overlapped (Niemz et al. 2020)

3.3 Summary

This chapter deals with the two survey areas in which the data sets for this thesis were obtained. The first part introduced the drilling of the geothermal well RN-15/IDDP-2 in Reykjanes, Iceland, and the second part is the HF experiments in the underground lab in Äspo, Sweden.

The drilling of the well and its stages is described, including information about the lithology and alteration. The second survey was a cooperation of KIT together with the GFZ to test the FHF advanced injection schemes. An extensive monitoring array was deployed including SP, EMR and AE sensors. The HF procedure is explained.

Chapter 4

Data processing: theory and results

4.1 Theoretical background of MT processing

The MT data processing is the estimation of frequency-dependent linear relations (transfer function) of magnetic and electric field components. As mentioned in chapter 2, equation 2.22 defines the relationship between the horizontal electric and magnetic fields and the impedance tensor (Chave and Thomson 2004). The matrix version in absence of noise is as follows:

$$\mathbf{E} = \mathbf{ZB}. \tag{4.1}$$

E and **B** are 2-vectors of horizontal electric and magnetic field components at a specific site and frequency. **Z** is a second rank, 2x2 MT response tensor (Chave and Thomson 2004). The solution is given in equation 4.2

$$\mathbf{Z} = (\mathbf{EB}^H)(\mathbf{BB}^H)^{-1} \tag{4.2}$$

The superscript H is the Hermitian (complex conjugate) transpose, and the parentheses are cross- and auto-spectra (Chave and Thomson 2004).

4.1.1 Robust response function estimation

If **E** and **B** are actual measurements then the equations 4.1 and 4.2 are contaminated with noise and the estimation of **Z** and its uncertainty $\delta\mathbf{Z}$ is necessary in a statistical way (Chave and Thomson 2004).

$$\mathbf{e} = \mathbf{bz} + \epsilon \tag{4.3}$$

with N observations (e.g. N Fourier transforms of N independent data sections at a given frequency), with **e** as response N-vector and **b** as Nx2, rank-2 predictor matrix. **z** is the solution 2-vector and ϵ a N-vector of random errors (Chave and Thomson 2004). The conventional approach is a classical least square (LS) regression, which means to minimize the sum of squares of residuals:

$$\sum_i |r_i|^2 = \sum_i (\mathbf{e} - \mathbf{bz})^2 \tag{4.4}$$

Denote the squared length of a n-dimensional vector **v** by $||\mathbf{v}||^2 = \mathbf{v'v} = \sum_{i=1}^{n} v_i^2$, equation 4.4 can be expressed as:

$$||\mathbf{e} - \mathbf{bz}||^2 \tag{4.5}$$

The L_2 norm in equation 4.5 can be minimized then by the LS estimators:

$$\tilde{\mathbf{Z}} = (\mathbf{b}^H\mathbf{b})^{-1}(\mathbf{b}^H\mathbf{e}) \tag{4.6}$$

$\mathbf{b}^H\mathbf{b}$ and $\mathbf{b}^H\mathbf{e}$ are the averaged estimates of auto- and cross-power spectra.

The Gauss-Markov assumptions for the LS, such as no correlation between regressors or that the errors have a constant variance, are not applicable for natural EM source data as stated in Chave and Thomson (2004) and Chave and Thomson (1989) .

(i) During times of geomagnetic disturbances, the residual variance often depends on data variance.

(ii) Data anomalies occur in patches due to such events and violate residual independence requirement, and

(iii) subsequently, more large residuals are common than expected by a Gaussian model.

Any of these cases can cause heavy bias in the LS solution shown in 4.6 (Glen 2018). Therefore, robust procedures are developed. Robust regression provides an alternative to LS regression, relying on less restrictive assumptions. For example, when outliers are present in the data, robust methods provide suitable regression coefficient estimates. However, outliers violate the assumption of normally distributed residuals in the least squares regression (Chave and Thomson 1989). The detailed procedure is described in Appendix B.1.

The advantage of the BIRRP code is that Chave and Thomson (1989) added a leverage control in addition to the robust estimation when it is not sufficient only to limit the influence of outliers. It provides reliable protection against strong data residuals but remains highly sensitive to extreme magnetic field values Chave and Thomson (1989). Subsequently, Chave and Thomson (1989) introduced the bounded influence remote reference (BIRRP) code. The theoretical background of the code is also described in B.2.

4.1.2 Processing steps of BIRRP

The processing of MT data is carried out using the bounded influence remote reference code, BIRRP, (Chave and Thomson 2004). The processing steps can be summarized as follow:

1. Visually inspecting the time series is important to identify possible errors, e.g., if it was measured with reversed polarity.

2. Editing of time series (e.g., spikes, long-term trends) and application of digital filters.

3. Time series are divided into sections by using Welch overlapped section averaging to detect outliers and to improve statistical efficiency (Chave and Thomson 2004).

4. The next step, pre-whitening, is carried out with a short autoregressive filter to avoid spectral bias. Leakage and bias are caused by sidelobes inherent to spectral estimation. There are two possible ways to minimize leakage: First, by using data taper windows, the side lobes become smaller. Second, pre-whitening reduces the power that can pass into side lobes. In this thesis, Slepian sequences are preferred as data tapers because they only depends on one parameter, time-bandwidth (Chave and Jones 2012).

5. After the Fourier transforming of the sections, the pre-whitening is corrected. Finally, the calibration files for the magnetic components are used to remove the instrument responses from the data.

6. Computation of response function using conventional or bounded influence (remote reference) methods. The estimation of the response function is widely discussed in the literature, such as in Simpson and Bahr (2005) or Chave and Jones (2012).

7. Estimates of the standard error on the result are computed using the unbalanced jackknife. Two major challenges in error estimation are, firstly, the correct computing of a number of degrees of freedom in the presence of correlated estimates (Chave and Thomson 1989). The second is, for example, the use of numerous approximations such as Taylor series or asymptotic behavior (Chave and Thomson 1989). Therefore, in recent years, research has turned to non-parametric methods. Confidence interval estimators such as the *jackknife* have the advantage of being a non-parametric method. Parametric methods tend to violate variance homogeneity, meaning that the level of variance for a given variable is constant across the sample. Non-parametric methods, such as jackknife, are insensitive to these violations (Chave and Thomson 2004).

8. Section length is reduced as higher frequencies are addressed, and the whole process is repeated.

4.1.3 Remote reference

The previous processing steps are described for the processing of one MT station. It can be modified to a remote reference scheme by substituting the auto and cross spectra with electric field components of the remote station (see Appendix B.3).

Following the approaches of Gamble et al. (1979) and Clarke et al. (1983), uncorrelated noise can be eliminated from the measured data using remote referencing when a high degree of correlation between the naturally induced electromagnetic fields at a local and at a remote site is reached. Therefore, the remote reference must be sufficiently distant to the local station, i.e., a few skin depths (Chave and Jones 2012). That ensures that the possible bias errors due to correlated noise are small compared to the random errors (Chave and Jones 2012; Gamble et al. 1979).

4.1.4 Parameters in BIRRP-code

The data were processed using the bounded influence remote reference processing software BIRRP in the advanced mode. To overcome the absence of high quality remote data (see below), the station data itself were used as remote reference. To obtain the best possible data quality and low error bars, the following parameters were selected from test runs (Table 4.1).

TABLE 4.1: Summary of the parameter that were applied during data processing using the advanced mode in BIRRP.

Parameter	Value
Time-bandwidth for the Slepian data taper	2
Maximum FFT section length	1024
Total number of reductions	6
Factor of section reduction	2
Index of the first frequency in each section	8
Increment of the first frequency in each section	1
Number of frequencies	8
Coherency threshold for the electric and magnetic field	0.35
Length of time windows of two consecutive days	524'288 points
Number of frequencies to be rejected	2
Pre-whitening filter order	5

4.2 Characterization of noise

Junge (1996) defines noise as part of the data which a theory cannot explain. The EM theory is, as discussed in chapter 4.1, not valid with real data; hence, noise causes biased data. In literature, noise in electromagnetic data is mainly from geologic, cultural, or instrumental noise sources (Chave and Jones 2012; Junge 1996). Cultural noise is often referred to as man-made noise.

4.2.1 Cultural noise

Cultural noise is of artificial origin from power transmission or communication systems. The high level of noise causes an increase in stochastic uncertainty on spectral estimates due to a decreased signal-to-noise ratio (Chave and Jones 2012). Also, spectral leakage occurs from narrow band noise sources. Cultural noise can be divided into active and passive sources (Szarka 1988). Active sources are caused by a primary source as powerlines, fences or pipelines, and induced secondary fields are defined as passive sources. The most prominent peaks of cultural noise in MT data are the 50 Hz or 60 Hz peak in the power spectra due to the power transmission in Europe or the USA, respectively. The spectra are dominated by the primary frequency and the off-harmonics that rise from the departure of the waveform from a sinusoidal form. The peaks can be removed using notch filter acting on the primary frequency and harmonics (Chave and Jones 2012). Another typical peak is the 16.6667 Hz peak caused by the railway. Frequencies below 10 Hz are dominated by the electric field noise, while for higher frequencies, the noise in the magnetic channels is larger than electric field noise (Junge 1996). Junge

(1996) and Szarka (1988) stated that the signal decreases with increasing distance showing an inverse distance law for line current. Model studies could be helpful (Junge 1996) to reduce passive noise, which does not vary with time but might distort results. Junge (1996) suggested that if the noise is far enough from the recording site, the transfer functions could be split into near and far field parts.

An inevitable step in dealing with cultural noise is the visual inspection of time series because irregular noise is only recognizable if its amplitude exceeds the natural signal. Non-sinusoidal noise often produces signals with higher harmonics, which can be suppressed by delay line filter (Junge 1996). Even after all processing approaches and after taking all hints and tips into account for installing a MT site, there is no direct way to separate noise properties from both data, electric, and magnetic fields (Chave and Jones 2012; Junge 1996; Szarka 1988). A remote reference station is a chance to improve data quality in a survey.

4.2.2 Geological noise

Geological noise can have effects on the MT response of spatial changes in resistivity due to other geological sources than the target (Chave and Jones 2012). The possible sources are soil and regolith layers, swamps, or the topography of the survey area. For example, topography can perturb impedance that causes galvanic perturbation of the MT component with an E-field perpendicular to the topography (TM component). Resistive layers as clean sands have more than 10'000 Ωm and more rapidly attenuating EM noise with distance from the source. Due to the strong attenuation of EM fields in very conductive or thick near-surface layers, underlying targets are hard to resolve. Between 0.1 - 1 s, conductive surface layers can have an inductive effect on MT response (1D, 2D, or 3D effects). For most resistivity structures, the response will mask underlying zones' resolution with higher resistivities than the top layer. If there is a case of $\sigma_1 > \sigma_2$, then it is hard to impossible to resolve underlying layers properly (Chave and Jones 2012).

4.2.3 Instrument noise

Instrumental noise is caused due to the temperature dependence of magnetic or electrochemical processes in electrodes (Chave and Jones 2012). Electrodes, in general, have the most influence on the quality of E-field measurements in MT surveys. Subsequently, they are the most critical component and should be chosen with care (Chave and Jones 2012). Figure 4.1 shows time-frequency characteristics of noise for electrodes in lab and field and instruments with signal levels.

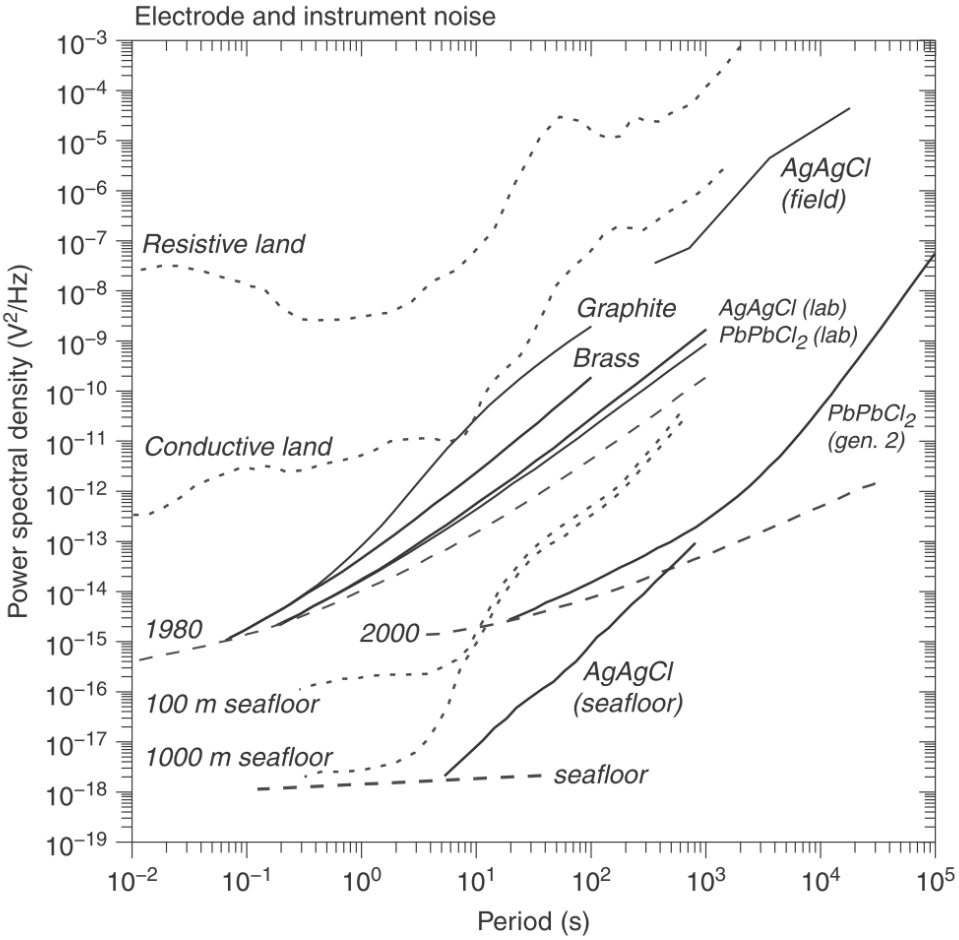

FIGURE 4.1: Electrode and instrument noise with signal levels (Chave and Jones 2012). Black solid lines show the noise level of electrodes in lab, field, and marine deployments; short-dashed lines are telluric potentials, and long-dashed lines are instrument noise.

Between periods of 1 - 10 s, electrode noise might have the highest impact on the signal-to-noise-ratio (4.1). This is because the short periods are dominated by an amplifier and other instrumental sources and less by electrodes. With increasing period, the electrode noise increases higher in field deployments than in the lab experiments (Chave and Jones 2012). Due to the almost isothermal and isosaline conditions in marine surveys, the electrode noise level in the seafloor environment is even lower than in the lab (Constable et al. 1998). During long-term surveys, electrodes might be exposed to the largest temperature variation, which can grow to a sensitive issue in terms of data quality. Chave and Jones (2012) quantifies the influence about 30 - 200 μV/°C for Pb-PbCl_2 and about 160 - 300 μV/°C for Ag-AgCl.

Figure 4.2 shows a) noise and b) sensitivity levels of induction coils and flux-gate magnetometer sensors. Fluxgate noise sources are mainly caused by sensor noise, thermal drift, and long-term drift (Chave and Jones 2012). Chave and Jones (2012) stated that the noise in induction coils is mostly from the coil itself and the electronic circuity, including the amplifier. At higher frequencies, the thermal resistance and the Johnson noise of wiring in the coil are primary noise sources. At very low frequencies, the noise spectrum is dominated by 1/f noise from semiconductors in electronic circuity. As it can

be seen in Figure 4.2b, inductions coils have higher sensitivities at periods of less than 10^3 s, and the fluxgate sensors for longer periods. In this thesis, the MFS-07e sensors were used with the highest sensitivities between 10^{-5}-10^{-1} s.

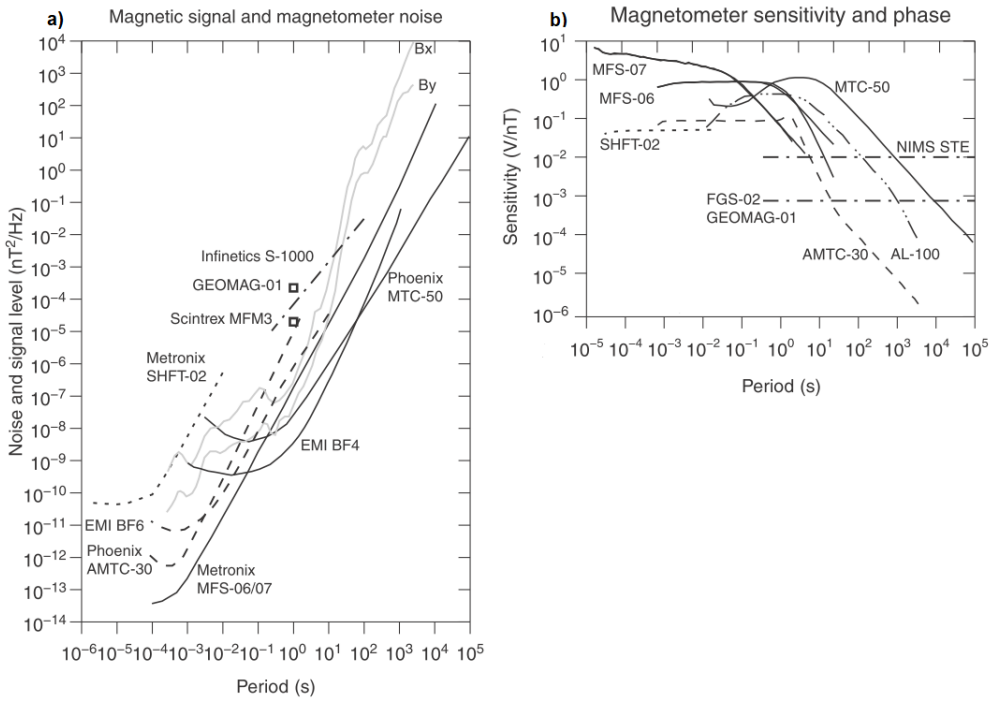

FIGURE 4.2: a) Noise and b) sensitivity levels of induction coils and fluxgate magnetic sensors from different companies including Metronix and Phoenix, modified after Chave and Jones (2012).

To summarize, geological noise is mainly observable in MT transfer functions. The other sources, especially cultural noise, can be analyzed in the power spectra or raw data (time series).

4.3 RN-15/IDDP-2 MT data set

The processing of MT data is carried out using the bounded influence remote reference code, BIRRP (Chave and Thomson 2004). Parameters were set according to test runs (see table 4.1). Mostly acceptable transfer functions were obtained using these parameters in a 48-hour processing window. Note that a geoelectric strike of N0°E is derived after Becken and Burkhardt (2004), therefore, no rotation of the impedance tensor is required for further analyses due to the experimental setting. Thus, XY- and YX-components are sub-parallel to N-S and E-W directions, respectively.

4.3.1 Remote referencing

Note that for MT monitoring, the perturbation period is crucial for the applicability of remote referencing. Changes in the engineering process, i.e., flow rate, pressure, or even related seismicity are caused by perturbations

at the well bottom. These issues are discussed in detail in the section 4.2. If a low period concerning the measurement period and causing an electromagnetic signal, these changes may contribute to uncorrelated noise. Hence, when applying conventional remote referencing, this signal of interest may be weakened or eliminated from the data. Therefore, several remote stations were tested during the project period including a temporary remote reference for the test measurements in September 2016, the MT station RAH at a distance of 5 km from the drilling platform, and the Wittstock remote site in the Northwest of the federal state Brandenburg in Germany. Since the coherency needs to be high for the remote referencing, the transfer functions are averaged over 48 hours to obtain a reasonable resolution for the depth of investigation (Gamble et al. 1979).

Remote referencing with the temporary remote station

In the following, transfer functions calculated for 48 h (workdays 46 - 47) and operations at the drilling site are discussed. On workday 46, the loss zones in the well were cemented down to 2950 m with flow rates between 15 and 30 L/s. At 3:10 p.m., a seismic event of magnitude 0.86 occurred in the reservoir zone. On workday 47, drilling was performed from 2945 - 2950 m with flow rates up to 45 L/s and high-frequency changes.

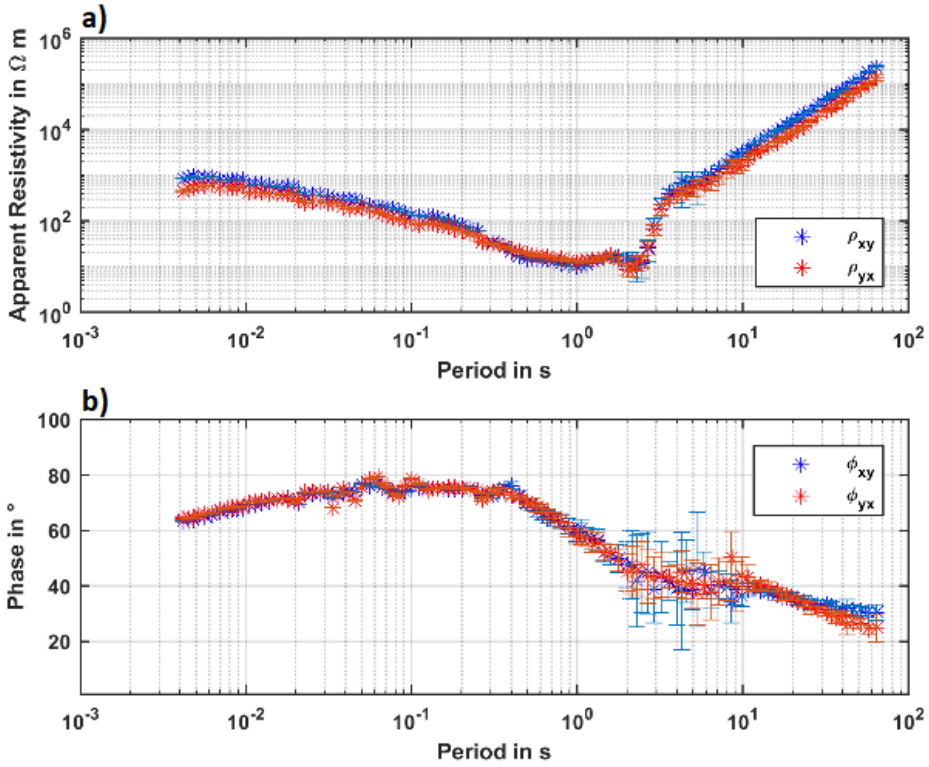

FIGURE 4.3: Single site processed XY (blue) and YX (red) components of apparent resistivity (a) and phase (b) of the temporary remote reference MT station from workdays 46 - 47 (Haaf and Schill 2019).

Figure 4.3 shows the single-site processed transfer function of the temporary remote station from the workdays 46 - 47. The Differences in XY and

YX components in both apparent resistivity and phase are relatively small, implying a well-layered 1-D underground.

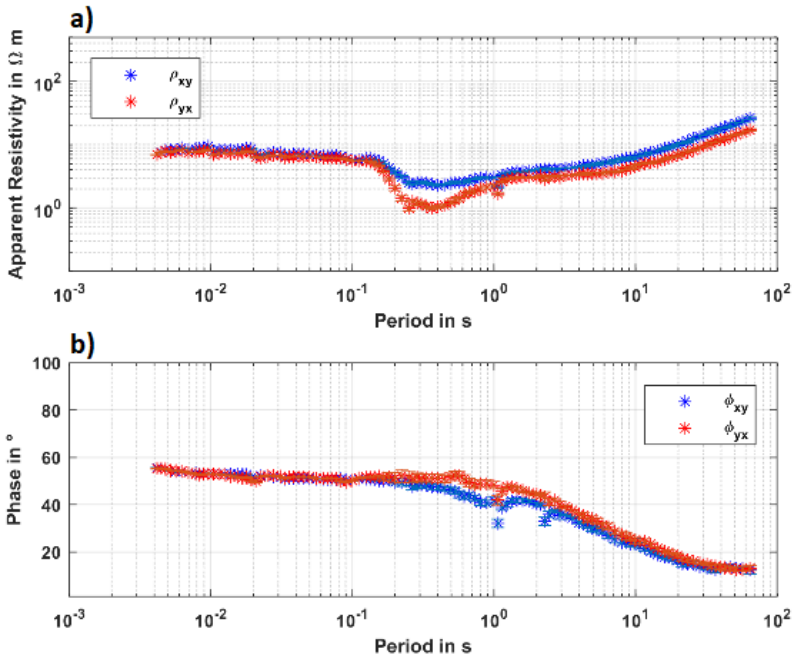

FIGURE 4.4: Single-site processed transfer functions using the temporary reference station, XY (blue) and YX (red) components of apparent resistivity (a) and phase (b) of GUN MT station from September the workdays 46 - 47 (Haaf and Schill 2019).

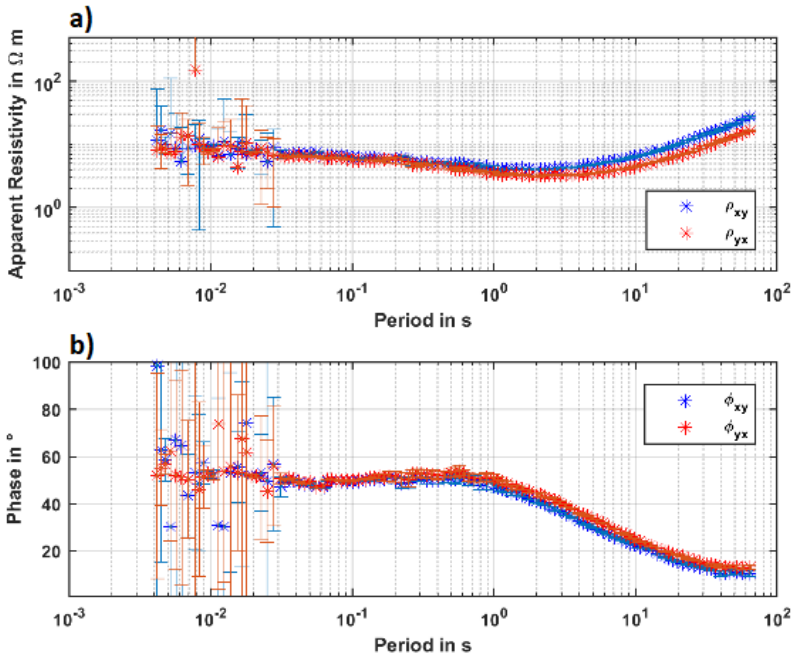

FIGURE 4.5: Remote reference processed transfer functions using the temporary reference station, XY (blue) and YX (red) components of apparent resistivity (a) and phase (b) of GUN MT station from September the workdays 46 - 47 (Haaf and Schill 2019).

The Figures 4.4 and 4.5 compare the transfer function of the same date using single-site and remote referenced processing. Single-site processing shows small error bars and relatively smooth changes in resistivity and phase over most of the periods (Figure 4.4). Small outliers are observed at 0.25 and 1 s in the apparent resistivity and 1 and 2.5 s in the phase. Between $1.5 \cdot 10^{-1}$ and 1 s the resistivity of the YX component decreases from about 6 Ωm down to 1 Ωm compared >2 Ωm in the XY component. Both the small outliers and the decrease in resistivity disappear with remote referenced processing (Figure 4.5). An evident decline in the quality of the transfer function is observed for the low periods down to $3 \cdot 10^{-2}$ s.

Remote referencing with the RAH station

For completeness, Figure 4.6 shows the remote-referenced transfer functions of the GUN station from the workdays 153 - 154, using the RAH station. As mentioned above, these measurements of this station were of bad quality. Consequently, the obtained transfer functions reveal unrealistic results ranging from apparent resistivity values of 10^{-6} to 10^{4} Ωm and extreme error bars for the phase.

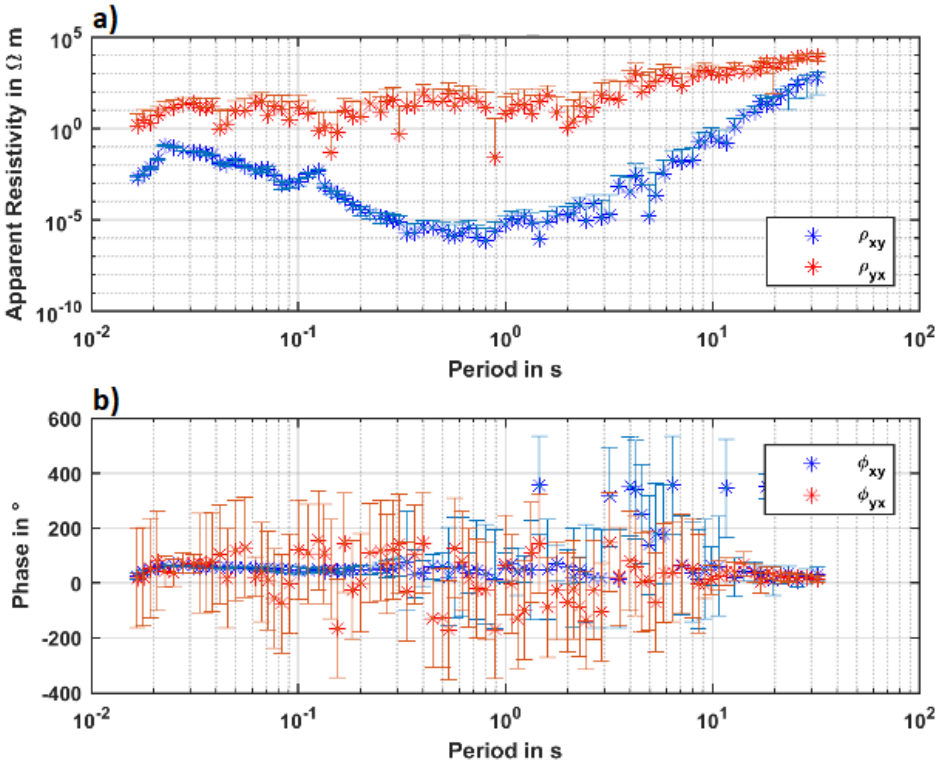

FIGURE 4.6: Remote reference processed transfer functions using the RAH reference station, XY (blue) and YX (red) components of apparent resistivity (a) and phase (b) of GUN MT station from the workdays 153 - 154 (Haaf and Schill 2019) .

Remote referencing with the Wittstock station

Due to different sampling frequencies of 250 Hz in Wittstock (Ritter et al. 2015), the data of Wittstock were resampled using interpolation. In Figure 4.7, remote referencing processed transfer functions of a representative example from the workdays 46 - 47 are shown. The anomaly disappears in the remote referenced transfer function, leading, however, to a sharp increase in error bars at periods > 0.2 s and < 0.008 s in both apparent resistivity and phase.

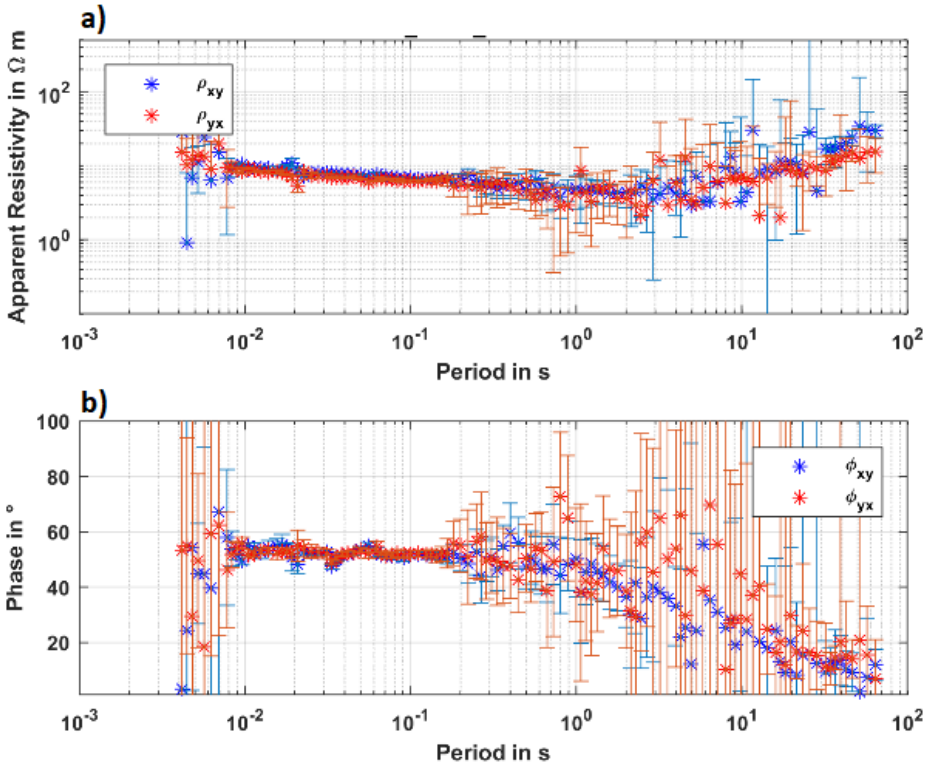

FIGURE 4.7: Remote reference processed transfer functions using the Wittstock reference station, XY (blue) and YX (red) components of apparent resistivity (a) and phase (b) of GUN MT station from the workdays 46 - 47. Wittstock data provided by Ritter et al. (2015).

Remote referencing was tested with a station at an intermediate distance at 46 km (at X = 363'000 and Y = 389'600 in Figure 3.7). Remote reference smooths the transfer functions but cannot decrease the error bars. Due to weather conditions, this remote station can be operated only in summer. Hence, the RAH station was installed during wintertime. However, remote referencing was not applicable throughout the monitoring period due to the bad data quality at RAH and the Wittstock stations.

Lerwick and Narsarsuaq are the closest geomagnetic observatories of the INTERMAGNET (www.intermagnet.org). However, data at these stations are obtained at a sampling rate of 1 Hz. Using these stations as a remote reference would require deleting more than 99 % of the data. Besides, MT monitoring aims at observing changes in the electromagnetic field triggered

by the hydraulic load in the reservoir. When cross-powers between the remote and local variables rigorously replace the local auto- and cross-powers, the high-frequent target signal of MT monitoring may be removed because it appears as uncorrelated noise (Chave and Jones 2012). One can consider the wanted electromagnetic signal appearing as an uncorrelated signal with the distant remote reference station given the short wavelength of the perturbations introduced by drilling and reservoir engineering, and the even shorter wavelength of seismicity concerning the period of integration of 48 h.

For these technical and conceptual reasons, single-site processing appears to be the best compromise for this survey. Notch filters of the respective frequencies were applied to eliminate only the uncorrelated noise originating from operations at the surface. In the case of the high-frequency signal, an improvement of filtering is achieved by decimating the sampling frequency before filtering as shown in the next section 4.3.2.

4.3.2 Time-frequency analyses of anthropogenic noise sources

The MT data set from the monitoring of RN-15/IDDP-2 revealed challenges in the MT data processing. During the drilling of the well heavy machines contribute to the local cultural noise level. Also, an 18-days long noise signal was detected and had to be eliminated in a pre-processing handling.

Editing and filtering of time series

Figure 4.8 shows an example of raw and filtered time series of all five electric and magnetic components. The example is from a biased time window of 18 days during the MT monitoring period.

The 14 Hz noise signal occurs roughly every 30 minutes with a duration of about 60 - 90 s. The source of noise could not be identified. Since the 14 Hz noise occurs approximately every half hour between the workdays 112 - 130, the deletion of the noise would result in data loss of about 50 - 70 minutes per day. To better visualize the noise peaks in the spectrum, the data were decimated to lower frequency bands (128 Hz). Pre-filtering using a notch filter for the respective bandwidths were applied to the 128 Hz data. The spectra of the raw and the filtered data are presented in Figure 4.9. The spectra indicate a significant elimination of the 14 Hz noise signal, and an apparent reduction in amplitude is shown in the time series in Figure 4.8. However, complete removal of the peak is not obtained. A 6 Hz notch filter was also applied to the vertical magnetic field component.

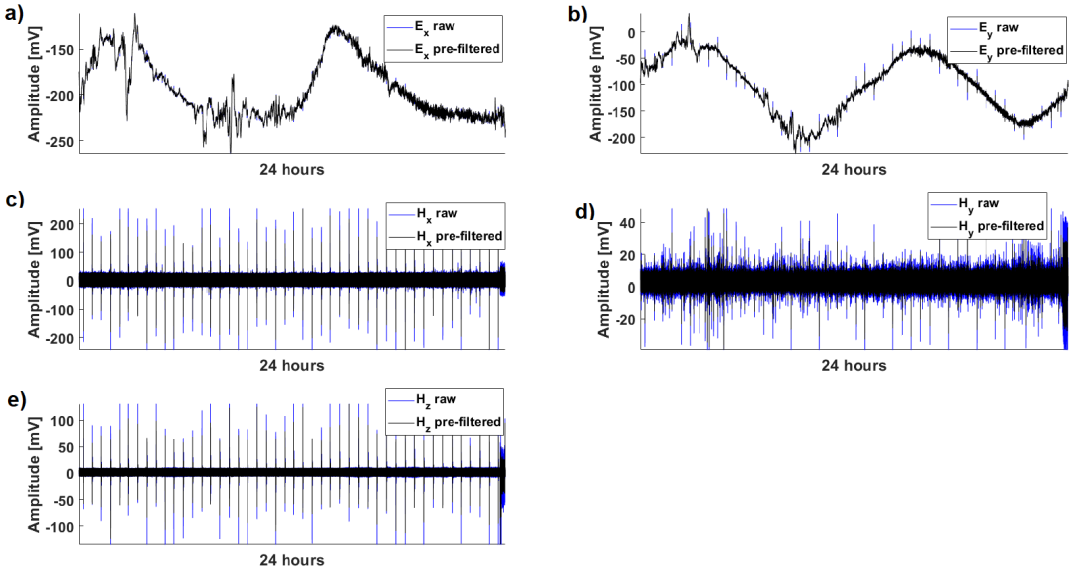

FIGURE 4.8: The time series of the a)-b) electric and the c)-e) magnetic field components are shown from workday 123 in a measuring period of 24 hours. The raw data are illustrated in blue, the bandpass filtered in black.

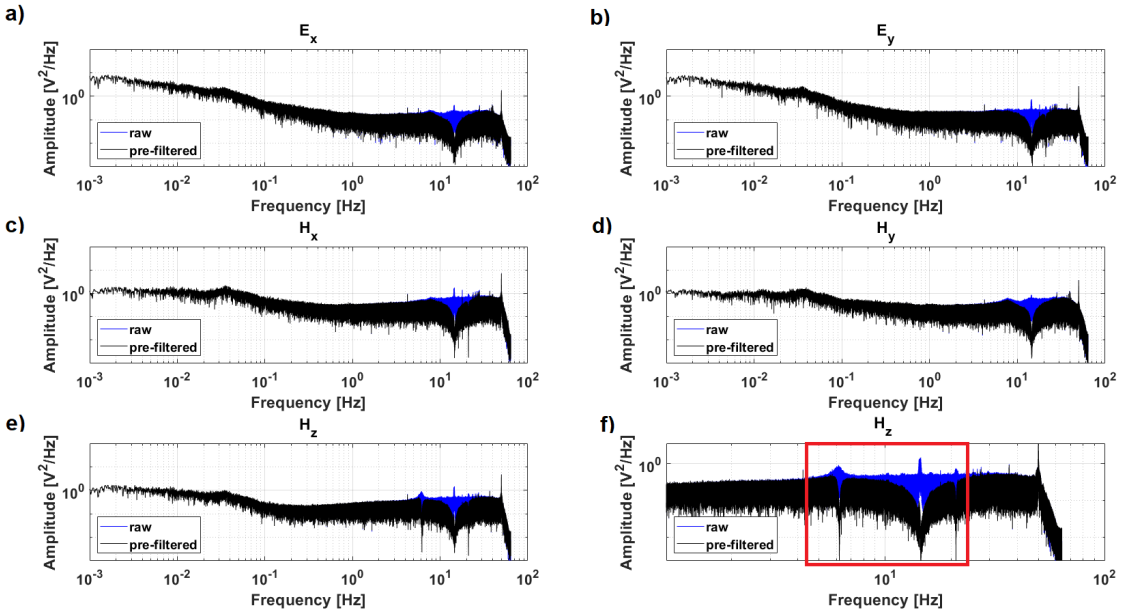

FIGURE 4.9: The calculated spectra of the a)-b) electric and c)-e) magnetic components are shown with a sampling frequency of 128 Hz. The raw data are illustrated in blue, the bandpass filtered in black. The red box shows a zoom into peaks and applied notch filters of the f) vertical magnetic component, modified after Haaf and Schill (2019).

Drilling parameters

In the following, time series and power spectra of representative workdays are provided to elucidate the noise and a possible influence of the drilling process on the electromagnetic signal. As type parameter, the rotational

speed of the drill bit and the torque are compared to the magnetic and electric component for a representative time period (Figure 4.10). The torque is the rotational force between the drill string and the formation. The time series are generally noisy. The electric components seem to be affected by a periodic signal that corresponds to tidal noise periods (Figure 4.10b). A clear correlation between noise and the onset of drilling is not evident.

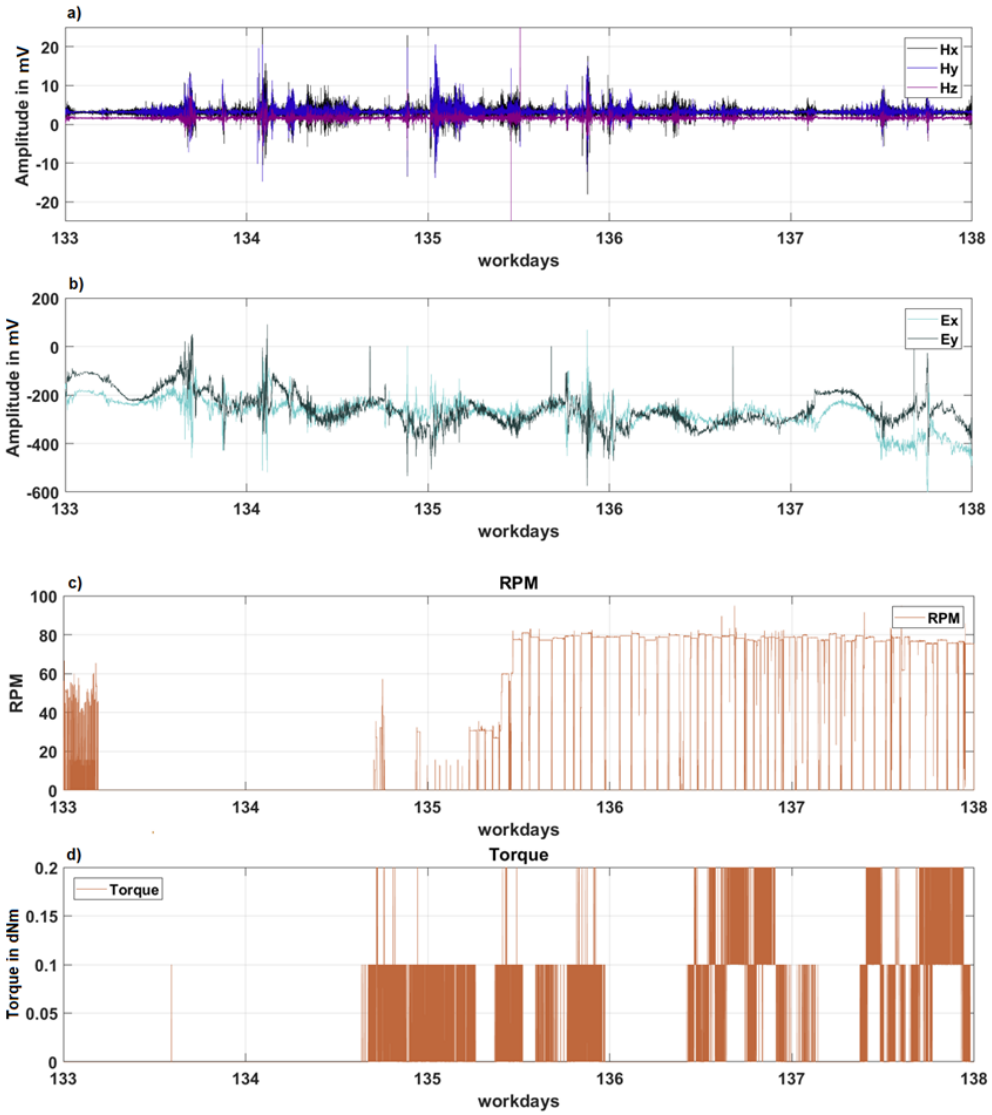

FIGURE 4.10: a) The magnetic field components, Hx, Hx, and Hz, b) the horizontal electric field components, Ex and Ey, and c) the rotation speed in revolutions per minute (RPM) and the torque (dNm) for the workdays 133 - 137 (Haaf and Schill 2021).

The power spectra of the electric and magnetic components (Figure 4.11) were calculated using Welch (1967). The magnetic components overlap and show very similar distributions with no significant peaks. The electric components show small peaks between 4 - 10 Hz. The magnetic components appear to be less affected by noise.

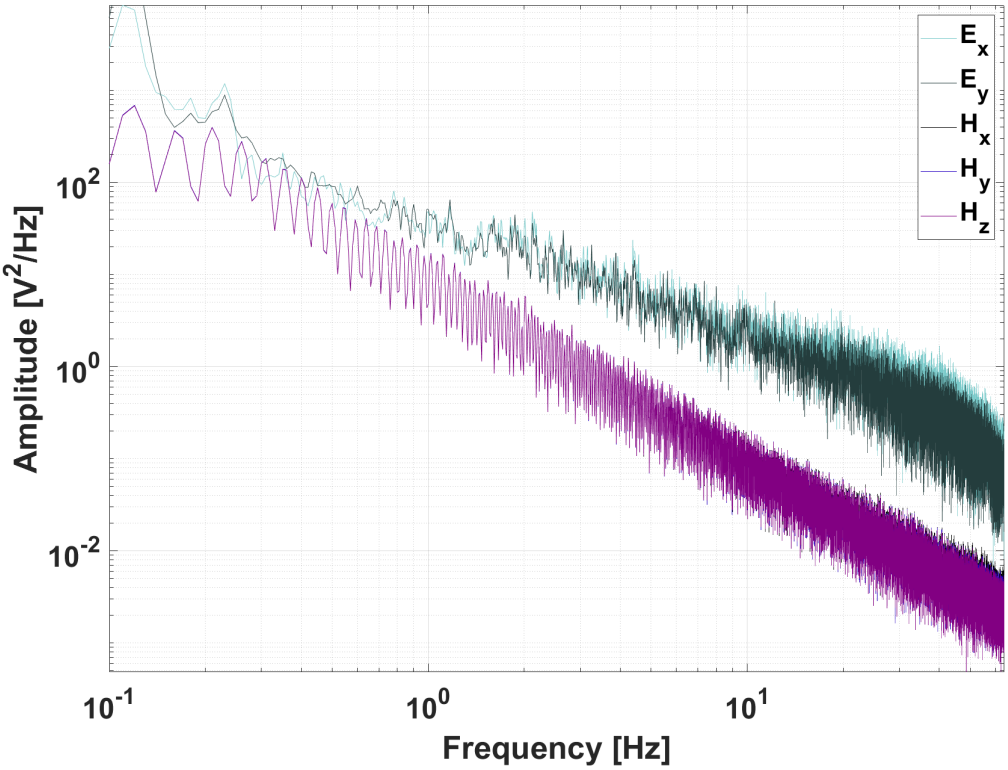

FIGURE 4.11: A representative calculated power spectra for the time series recorded during workdays 133 - 137 (Haaf and Schill 2021).

A time-frequency analysis allows for examining possible noise sources or frequencies in the data. Figure 4.12 shows the spectrograms of the time series of the five MT components at a window length of 3'600 s and a 50 % overlap providing the optimal resolution for both, time and frequency. The power-to-frequency describes the temporal signal strength or weakness of a frequency. A uniform spatial and temporal distribution indicates the absence of a noise frequency. The highest power-to-frequency occurs across the entire time period in the electric components for frequencies between 0.1 - 0.01 Hz, and high power-to-frequency between 10^2-1 Hz. Moderate power-to-frequency values are observable between 0.2 - 0.5 Hz in the dead band for all five channels. Compared to the electric, the magnetic components reveal rather moderate power-to-frequency values.

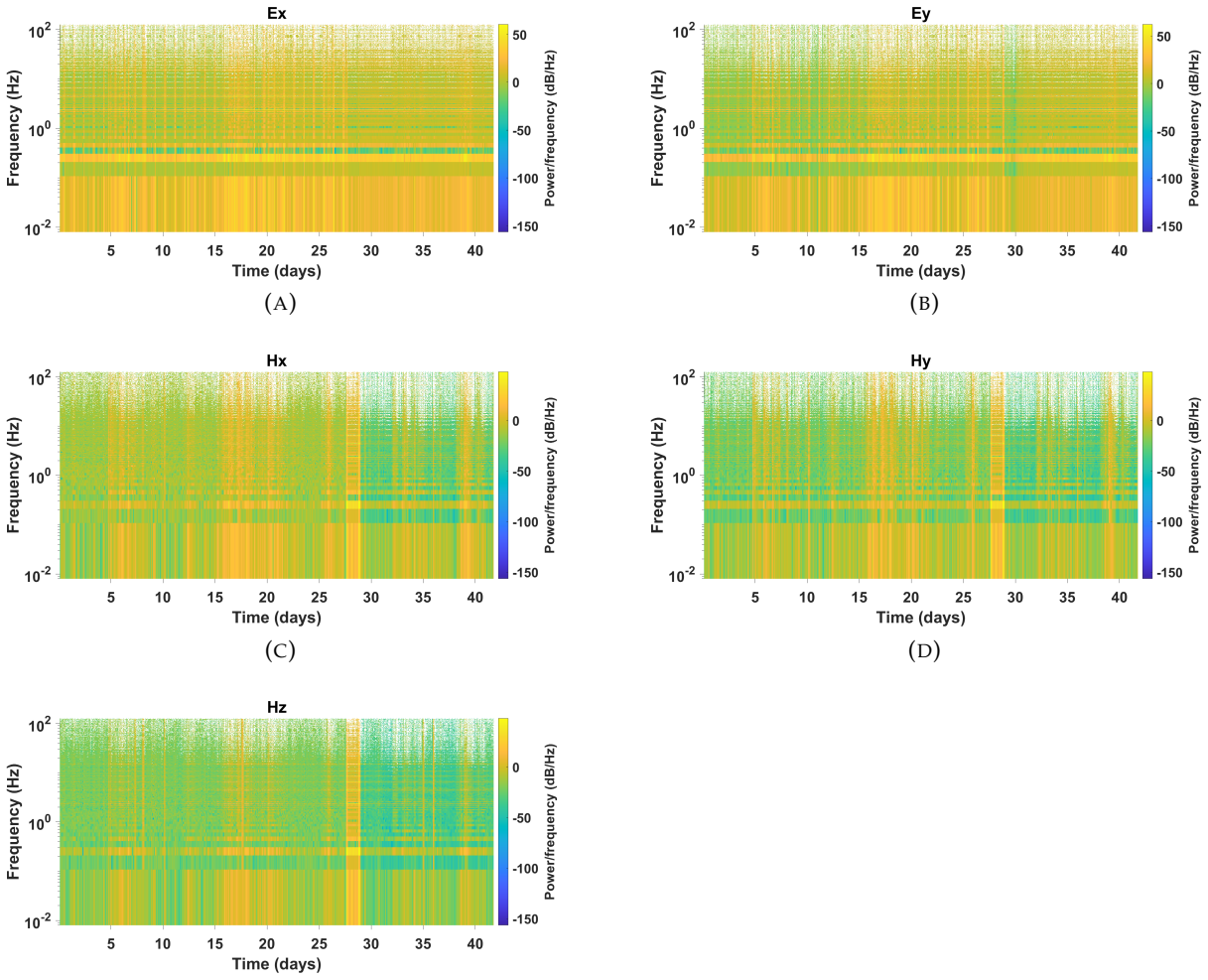

FIGURE 4.12: Spectrograms of the time series (a) Ex, (b) Ey, (c) Hx, (d) Hy and (e) Hz with 3600 s window lengths and 50 % overlap (Haaf and Schill 2021).

To investigate for periodic signals in the drilling parameters their power spectral density was estimated. Three representative parameters, RPM with additional motor, torque and pump are shown in Figure 4.13. While all three spectra show maxima at > 100 Hz, the torque reveals additional local minima at 40 and 80 Hz (Haaf and Schill 2021).

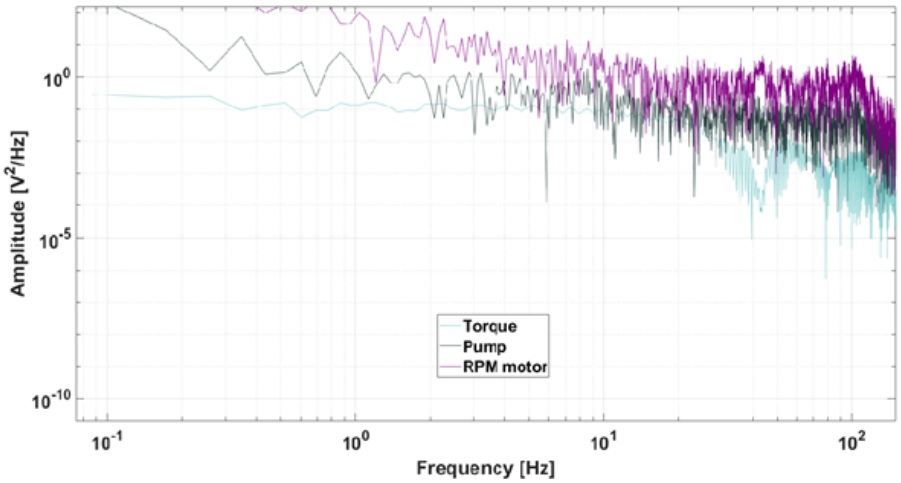

FIGURE 4.13: A representative calculated power spectra for the time series recorded during workdays 133 - 137 (Haaf and Schill 2021).

To identify anthropogenic noise from the drilling operation, the cross-spectrogram with each drilling parameter is calculated for each time series. The window lengths are 100 s, and 50 % overlap considering the lower sampling rate of 0.2 Hz for the drilling parameters. Figure 4.14 shows exemplary the cross-spectrograms of Ey with torque and Hz with RPM. Since the lithology and the progress control the drilling parameters, vertical blocks of the lowest power-to-frequency values of -150 dB/Hz appear when no torque or rotation speed is applied to the drilling equipment. In contrast to Figure 4.10, the cross-spectrogram do not reveal periodic signals. High power-to-frequency signals are observed throughout the monitoring period and when the drilling parameters are not used (blue colored).

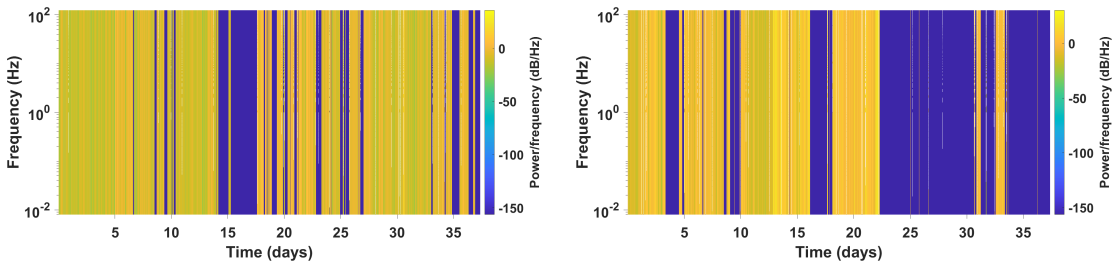

FIGURE 4.14: Cross-spectrogram of (a) Ey and torque and (b) Hz and RPM (Haaf and Schill 2021).

Summary processing and noise of the RN-15/IDDP-2 data set

This chapter deals with the processing and noise in electromagnetic data, in particular with noise in the MT data of this thesis. Three noise types have been characterized: cultural, geological, and instrument noise, which has the most significant impact on MT data. To reduce possible noise sources, the right deployment of the sensors is essential. Furthermore, the best suitable location for a MT site has to be found, and extensive data processing is necessary.

The second part of this chapter deals with noise in the Icelandic data set. Remote reference processing was tested on this data set but could not improve the data quality. Therefore, the processing scheme was adapted to substitute the remote reference processing to eliminate any possible noise sources by pre-processing and an extensive time-frequency analysis, including cross-spectrograms of the drilling parameters. The drilling parameters are analyzed and compared with the time series of the MT data. The time-frequency analysis shows that only the electric time series are affected by a periodic signal. This seems to be linked to tidal activity. However, with a frequency of $2.32 \cdot 10^5$ Hz, it is beyond the frequency range of interest (10^{-3} - 10^2 Hz).

To conclude, no consistent anthropogenic noise source that correlates with the intervals and frequencies of the observations in the transfer functions (i.e., decrease in apparent resistivity) could be detected in the data with methods applied in this study. Therefore, single-site processing was the best compromise in this study due to the danger of eliminating the sought-after electromagnetic signal as uncorrelated noise in the data.

4.4 Äspö dataset

The SP and EMR dataset were obtained during the HF experiments in the Äspö HRL.

4.4.1 SP data analysis

In this thesis, the measured SP raw data were obtained during HF experiments. The sampling frequency is 1 Hz. Three exemplary SP amplitudes obtained during HF2 are shown in Figure 4.15 as Δ V (the difference between the base electrode the corresponding electrode). The sampling example covers about 6000 s. The SP amplitudes vary between -1500 mV and 1800 mV. The time series have a high amount of peaks and fluctuating changes in amplitude.

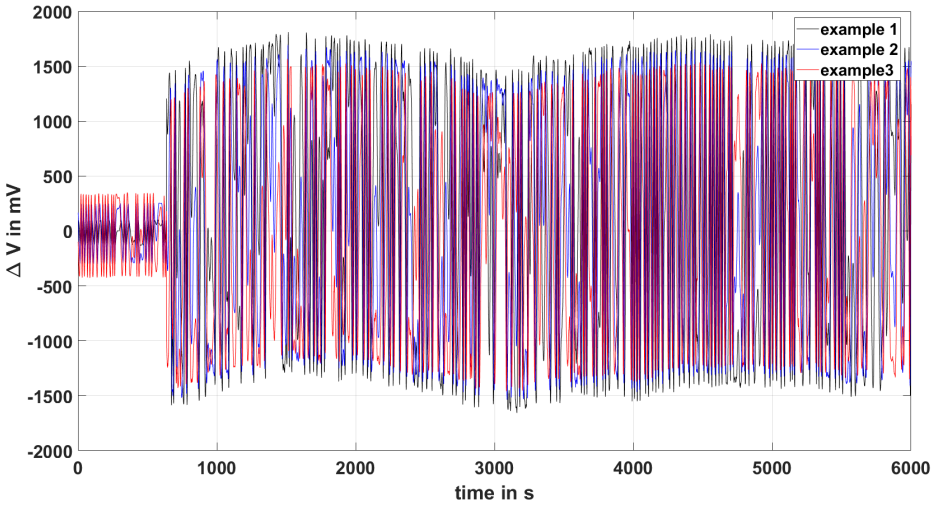

FIGURE 4.15: Three examples of raw SP data during HF2.

SP processing in monitoring campaigns has the goal of smoothing the data by applying a moving average filter. For example, during a one-week long injection in Soultz, Marquis et al. (2002) applied a one-day moving average filter to remove long-term trends of the SP data. That kind of procedure works as a convolution of the original time sequence with a boxcar function and is, therefore, a filtering operation. It acts as a low-pass filter by smoothing the data.

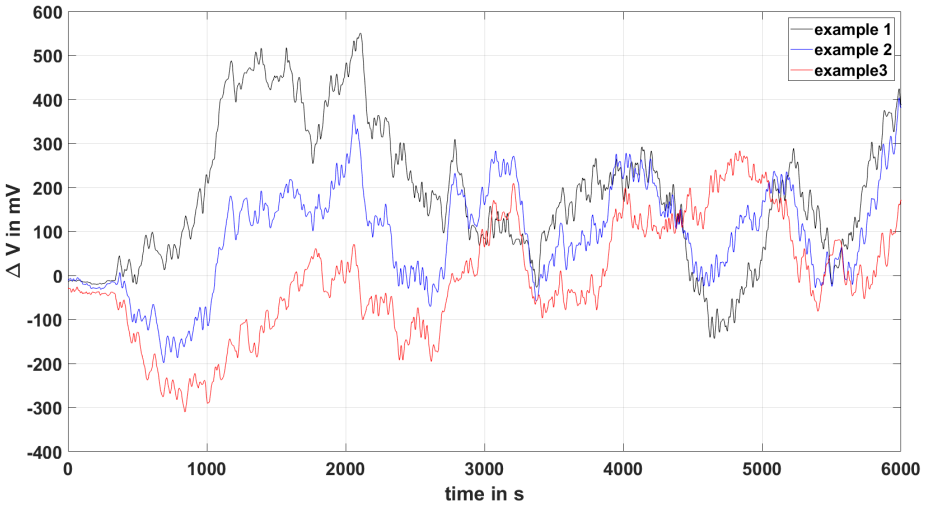

FIGURE 4.16: Three examples of smoothed SP data recorded during HF2.

In this thesis, the recording time was roughly between 90 - 120 minutes per HF experiment. Thus a ten-minute moving average filter was applied to the data. The results from the raw data (Figure 4.15) are shown in Figure 4.16. The amplitudes of the SP signals decreased and are now between -300 mV up to 500 mV. However, many small peaks remain in the data.

Therefore, a second moving average filter of 10 minutes was applied to smooth the data. The results are shown in figure 4.17.

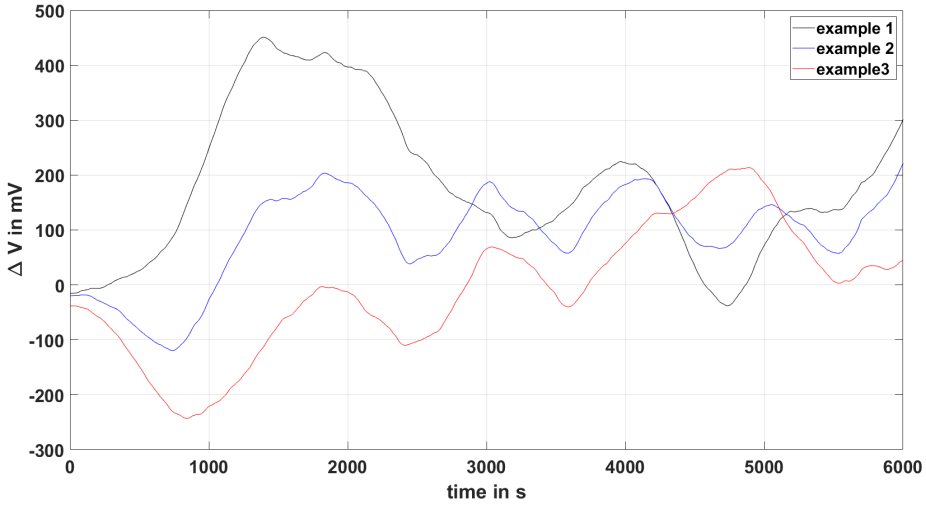

FIGURE 4.17: Three examples of smoothed SP data recorded during HF2.

4.4.2 EMR data analysis

In this study, the EMR data are band-pass filtered during the measurements. Hence, the behavior and the distributions of the three EMR parameters, namely the number of pulses and bursts and the burst energy, are analyzed. Figure 4.18 shows the distributions of EMR parameters during HF2 040° orientation. The burst energy is shown in black, the number of bursts in red, and the number of pulses in blue. All three parameters show increases in the same time intervals, whereby the bursts have the smallest amplitudes and the burst energy the highest ones. All three parameters have similar behavior throughout the experiment.

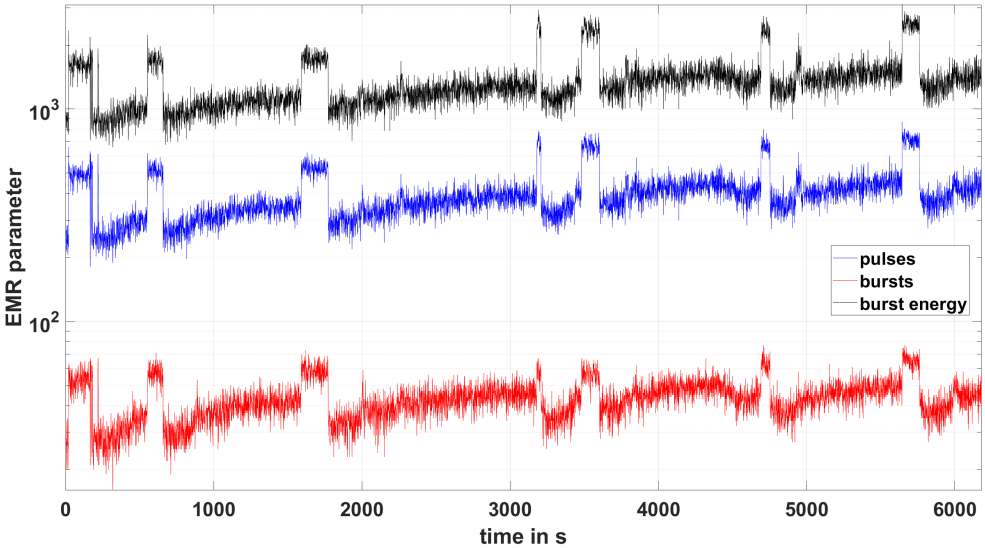

FIGURE 4.18: The EMR parameter measured during HF2 with sensors of the 40° orientation. The burst energy is shown in black, the amount of bursts in red and the amount of pulses in blue.

The EMR results of HF3 for the 130° orientation are shown in Figure 14. Here one can see that the distributions of burst energy and bursts are very small compared to the amount of the single pulses. Note that the number of bursts decreases during the maxima of the pulses, indicating that the discrimination line was set incorrectly. It appears that the signal was truncated due to the discrimination line being set too high, since the number of pulses increased at the same time as the bursts decreased. Therefore, the sensor with the 130° orientation was excluded from the discussion.

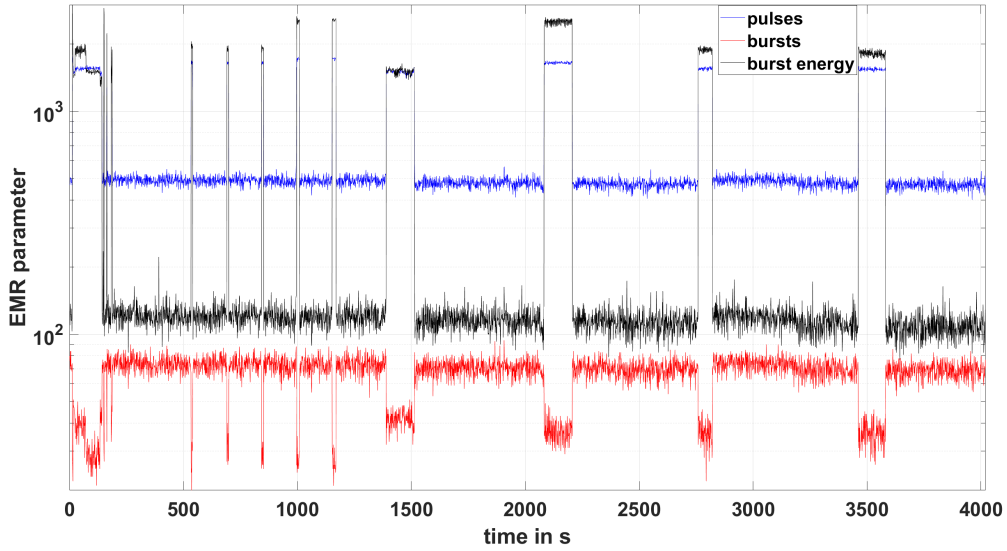

FIGURE 4.19: The EMR parameter measured during HF2 with sensors of the 130° orientation. The burst energy is shown in black, the amount of bursts in red and the amount of pulses in blue.

4.5 Summary

This chapter deals with the processing of the data set acquired in this thesis. MT processing accounts for the bulk of this chapter due to its elaborate processing scheme and the special handling of the Icelandic data set.

Chave and Thomson (2004) introduced a bounded influence estimator to limit the influence of both outliers and leverage points. Contrary to the conventional approach of remote referencing, the procedure in this thesis was single-site processing. Given the short wavelength of the perturbations introduced by drilling and reservoir engineering and the even shorter wavelength of seismicity concerning the period of integration of 48 h, one can consider the sought-after electromagnetic appearing as an uncorrelated signal with the distant remote reference station.

In contrast to the MT processing, the data sets of SP are processed more efficiently. A moving average filter was applied twice to smooth the SP data. The EMR data are already filtered and smoothed in the recording procedure. However, the EMR parameter of the 130° orientation revealed a too high discrimination line and was excluded from the discussion.

Chapter 5

Analyses of transient effects

This chapter deals with the results obtained during the monitoring of the geothermal well RN-15/IDDP-2.

5.1 Temporal changes in the transfer functions

In the following, the resulting single-site processed, filtered, and decimated transfer functions are averaged over 48 hours with an overlapping window of 24 hours. A reference day is required for comparison since operation in the conventional field is continuously ongoing, and MT monitoring started during drilling. The Ap value is used to describe the geomagnetic activity, i.e., the daily average of the Kp-values as a floating-point number (GFZ German Research Centre For Geosciences 2020). The daily Ap values are compared to the median value of 5 over the entire measurement period of workdays 112 - 167.

5.1.1 Reference transfer function and introduction to the cases

Given the unexpected high fluid losses and the induced seismicity during the deepening phase of RN-15/IDDP-2 and the continuous operation in the conventional part of the Reykjanes geothermal field, monitoring was started already during this deepening period. Thus, an unbiased reference could not be acquired. The reference transfer function that has been acquired during the workdays 46 - 47 (25-26/9/2016) is shown in Figure 5.1. These two days have been chosen based on the following criteria. The drilling had not yet reached the later open-hole section. Only cementing was ongoing.

The transfer function reveals a smooth distribution with an increasing period. Between 0.002 to 0.1 s, resistivity values are in the order of 10 Ωm with a slightly decreasing tendency towards longer periods. A significant decrease to 1 - 3 Ωm for the YX and XY components, respectively, is observed between 0.1-1 s. Towards longer periods, resistivity increases continuously. Generally, the YX component reveals lower values. Ap values of 20 - 22 indicate high geomagnetic activity during the workdays 46 - 47.

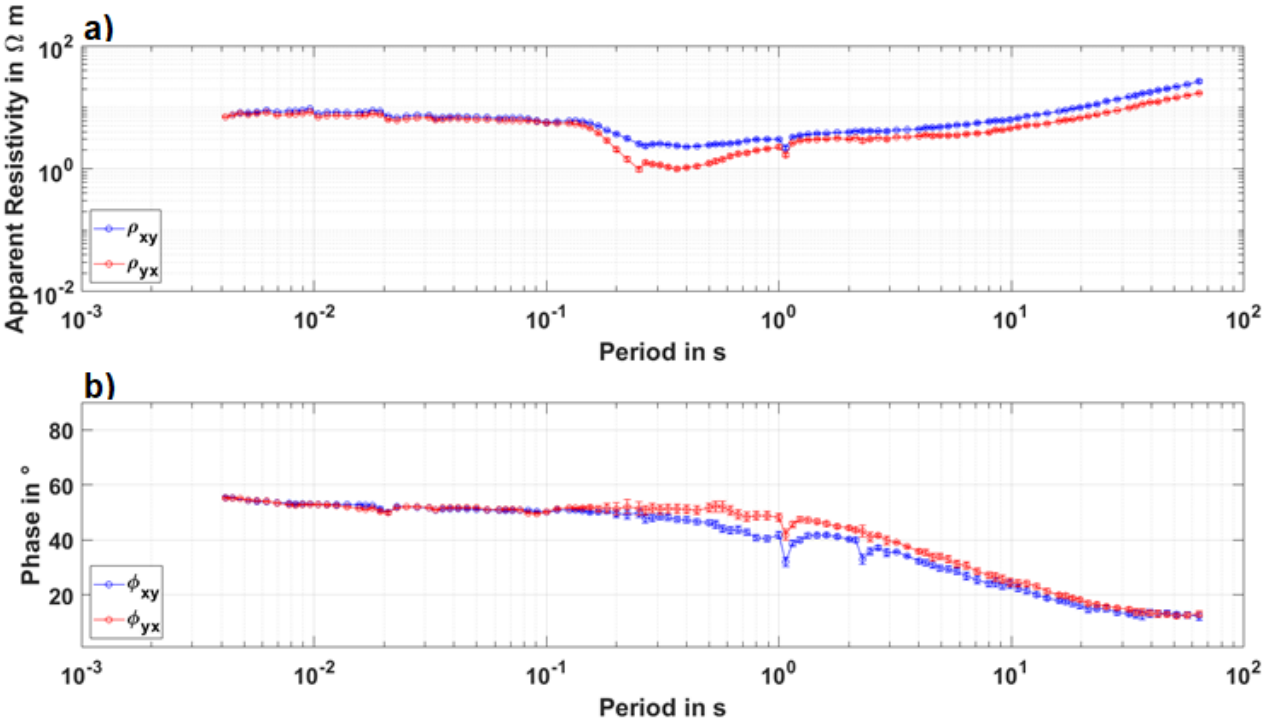

FIGURE 5.1: The reference transfer function that has been acquired during the workdays 46 - 47 (25-26/9/2016) with a) apparent resistivity, and b) phase of the XY component (Haaf and Schill 2021).

In the following, representative workday pairs with different combinations of geomagnetic, hydraulic, and seismic conditions are analyzed with respect to their electromagnetic responses. An overview of the cases is given in Table 5.1. The following cases include relatively low geomagnetic field activity, no circulation loss, small magnitudes and high numbers of events (Case 1), relatively low geomagnetic field activity, total circulation loss, small magnitudes and low number of events (Case 2), relatively strong geomagnetic field activity, no total circulation loss, large magnitudes and low number of events (Case 3), and relatively low geomagnetic field activity, total circulation loss, intermediate magnitudes and high number of events (Case 4).

TABLE 5.1: Overview of the changes in the geomagnetic field activity, the induced seismicity and fluid losses occurring during the workdays of the cases 1 to 4 (including data gaps of MT monitoring) (Haaf and Schill 2021) .

	Case 1	Case 2	Case 3	Case 4
Workdays	157-163	112-115	133-137	126-130
Total fluid loss during seismicity events	-	> 50 L/s on workdays 113-114	-	> 54 L/s on workdays 128-132
Number of induced seismic events	15 on workdays 161-163	2 on workday 113	6 on workdays 133 and 136	11 (9 on workdays 128-130)
Maximum magnitude	1.25	1.23	1.66 on workday 133	1.44
Workdays with Ap < median value	157-160	112-115	-	126-128
MT data gap	161	-	-	-

During workdays without total fluid losses or significant seismicity, little variation from the reference transfer function is observed (Figure 5.2). During the representative workdays, 116 - 117 and 165 - 166, 15 - 54 L/s, and 0 - 115 L/s, respectively, were circulated at different frequencies. Note that during both periods, geomagnetic activity is low (Ap values < median value). The only exception from these observations and the cases 1 - 4 occurs during the workdays 138 - 140 and is discussed in the section 5.1.6. Note that during that period, the Ap values are > the median Ap value.

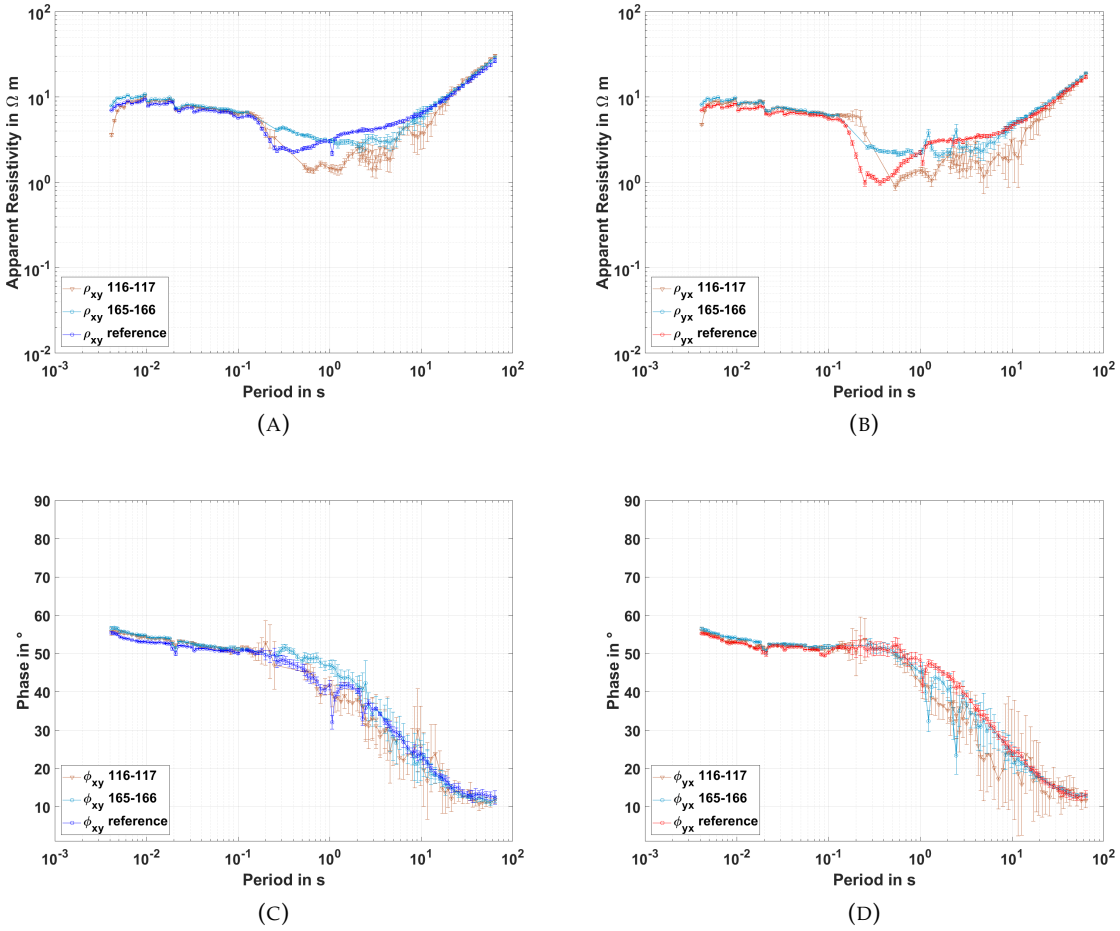

FIGURE 5.2: Transfer functions of the workdays 116 - 117 and 165 - 166 (injection rates of 15 - 54 L/s and in the latter 0 - 115 L/s) with a) apparent resistivity, and c) phase of the XY component and b) apparent resistivity, and d) phase of the XY component (Haaf and Schill 2021).

5.1.2 Case 1: No total fluid losses, maximum number of seismic events

In Case 1, a number of eleven, three, and one seismic events occur (3, 2, 1 with magnitudes M>1) on workday 161, 162, and 163, respectively. The Ap values vary from 1.5 - 4.5 during the workdays 157-160 and increase to 9.6 - 14.3 during the workdays 161 - 163. The changes in apparent resistivity and phase of the transfer functions over time are shown in comparison to the reference for the XY and YX components in Figure 5.3. Due to the data gap mentioned in section 3.1, MT data are available only for the workdays 156 - 157, 159 - 160, and 162 - 163. For the workdays 159 - 160, resistivity decreases with respect to the reference are observed between 0.1 and 20 s with minima of 0.1 Ωm and < 0.1 Ωm at 0.17 s and 0.37 s on the XY and YX components, respectively. This decrease nearly fades at the workdays 162 - 163 and the remaining offset is shifted towards larger periods. Apart from an increase in uncertainty and a decrease in smoothness during the workdays 159 - 160, the phase follows the reference curve in the XY component. Changes are significantly more prominent in the YX component and at periods > 2 s.

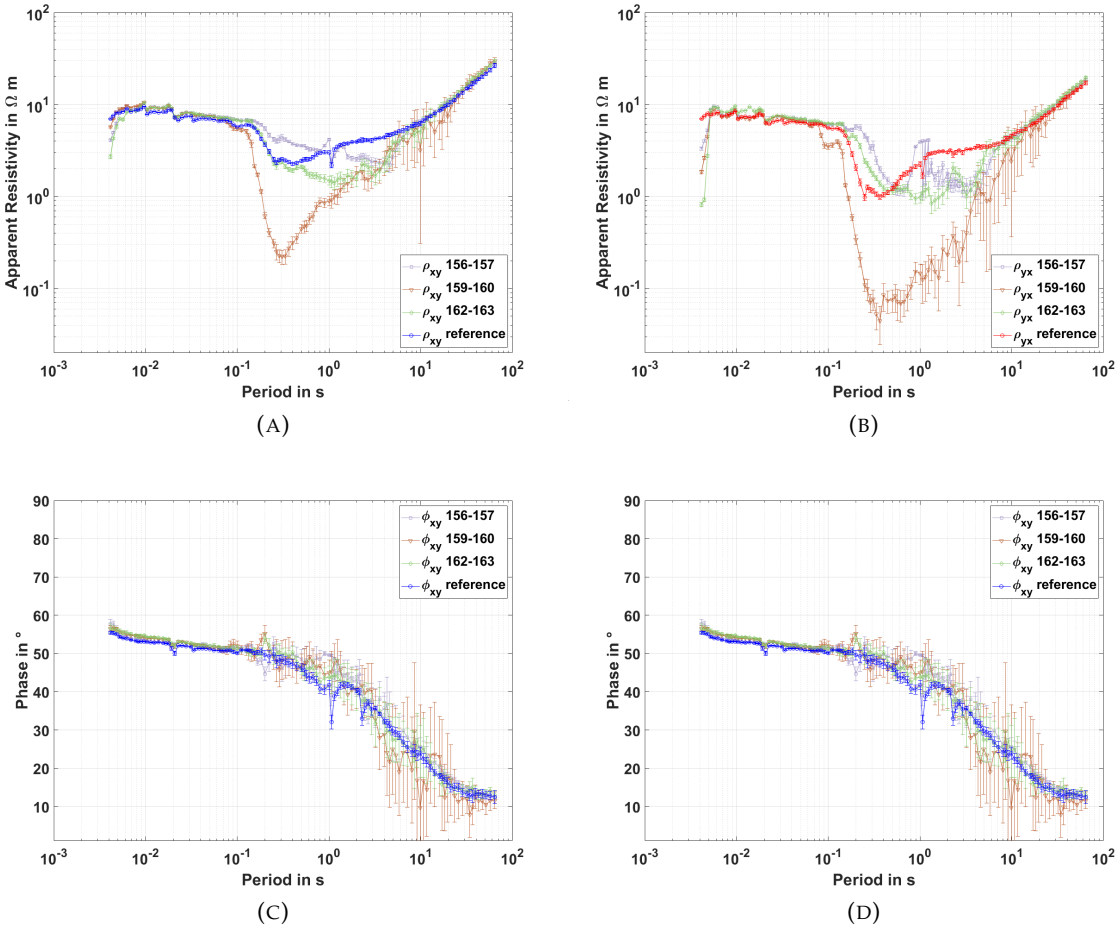

FIGURE 5.3: Transfer functions of the workdays 157 - 163 before, during and after 15 induced seismic events for the XY component with a) apparent resistivity, and c) phase, as well as the YX component with b) apparent resistivity, and d) phases (Haaf and Schill 2021).

5.1.3 Case 2: Total fluid losses, minimum number of seismic events

Case 2 deals with the workdays 112 - 115 during which total fluid losses of 50 L/s occurred when the well reached a depth of about 4188 m TVD after 30 hours. Only minor seismicity (three events of M < 1.2) occurred during workdays 113 and 115. The geomagnetic activity is continuously low showing a minimum Ap value of 0.9 on workday 116. The apparent resistivity and phase of these workdays (Figure 5.4) reveal a resistivity drop to 0.2 Ωm between 4 - 8 s with respect to the reference and predominantly in the YX components. The phase is reveals an increase in uncertainty at the same period range. Note that the difference to the reference is comparable to the workdays 156 - 157 and 162 - 163, in which no fluid losses occur (Figure 5.3). The reference curve is fully recovered by workday 116 (Figure 5.1).

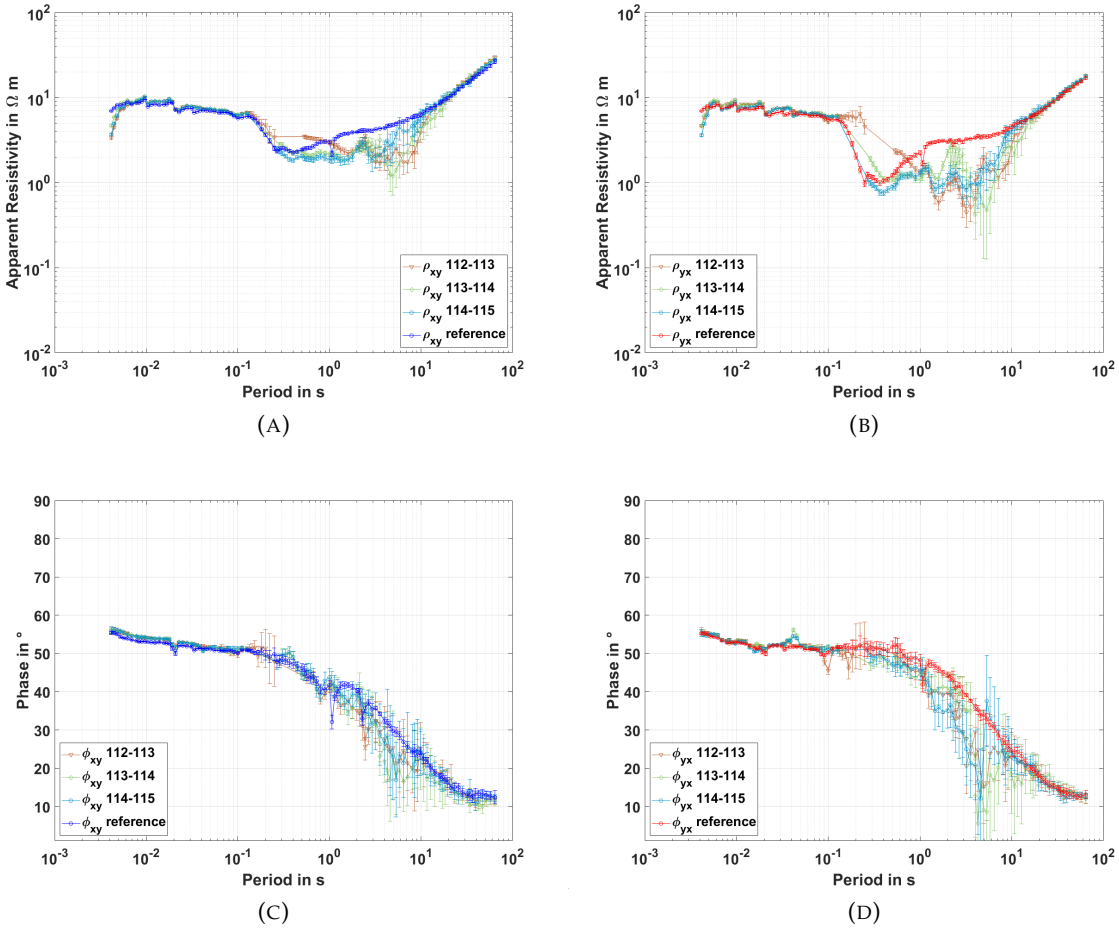

FIGURE 5.4: Transfer functions of the workdays 112 - 115 during total fluid loss for the XY component with a) apparent resistivity, and c) phase, as well as the YX component with b) apparent resistivity, and d) phases (Haaf and Schill 2021).

5.1.4 Case 3: No fluid losses, maximum magnitude induced seismicity

This interval is characterized by events with the maximum magnitudes of 1.6 and 1.3 on the workdays 133 and 136, respectively. Note that fluid losses stop on workday 132. Ap values between 11.8 and 23.2 characterize the strong geomagnetic field activity. The electromagnetic response of the subsurface in comparison to the reference is presented in Figure 5.5. No significant change with respect to the reference is observed during the workdays 133-134 with the maximum magnitude event. Changes develop at workdays 134-135 and reach a minimum of apparent resistivity of about 0.2 and 0.6 Ωm for the XY and YX components at 0.2 to 4 s during the workdays 135 - 136, respectively. The reference is recovered during the workdays 136 - 137 when the seismicity is ongoing and comes to an end.

The highest uncertainties in the phase are recorded in the period range of 0.6 - 20 s during the workdays 135 - 136. Besides the related scattering of workday 135 - 136, the trend of decreasing phase from the reference days is maintained for all workday pairs between 133 and 137.

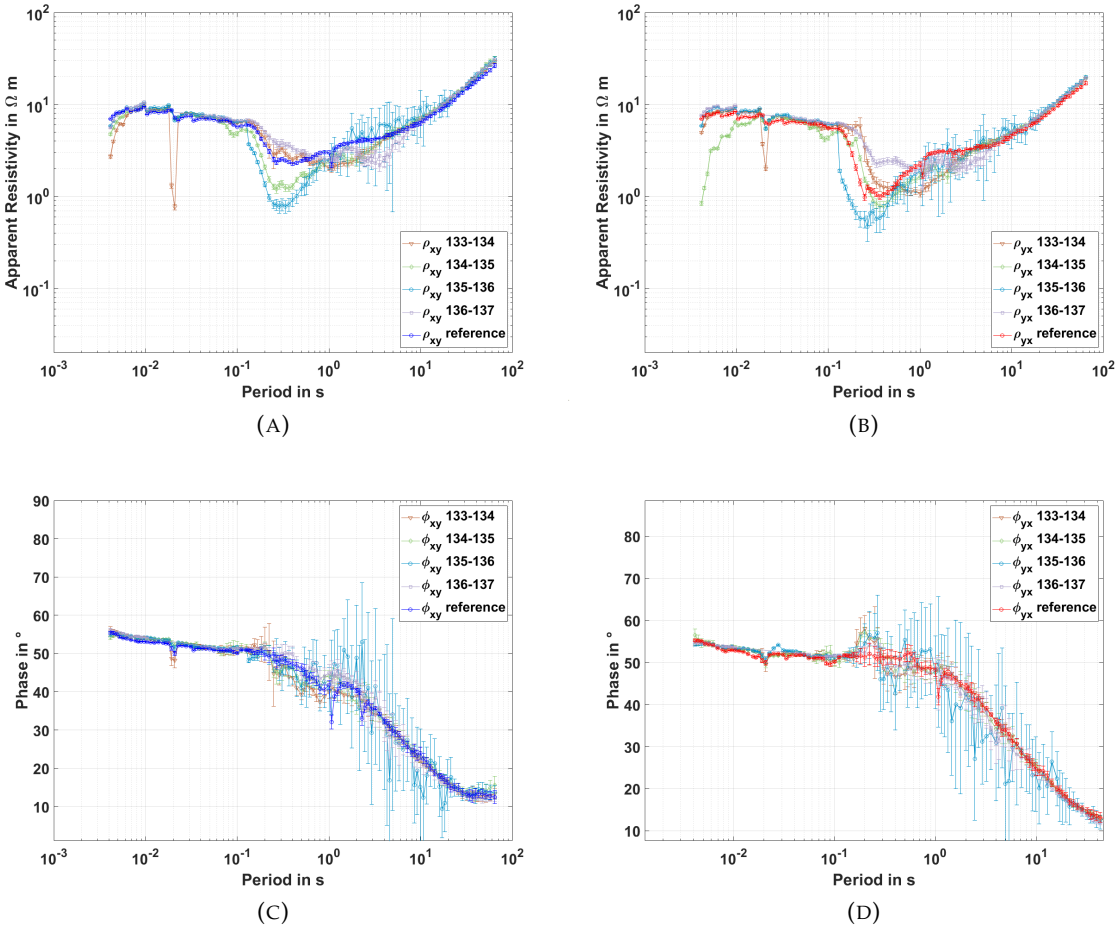

FIGURE 5.5: Transfer functions of the workdays 133 - 137 during an interval of seismicity with maximum magnitudes for the XY component with a) apparent resistivity, and c) phase, as well as the YX component with b) apparent resistivity, and d) phases (Haaf and Schill 2021).

5.1.5 Case 4: Contemporaneous fluid losses and induced seismicity

Total fluid losses characterize this period during the workdays 128 - 132. Continuous induced seismicity occurs during the workdays 126 - 130 with a peak frequency of four events and a maximum magnitude of 1.4 on workday 127 (Figure 5.6). Note that before workdays 126-127 with no fluid losses, a period of four days is characterized by fluid losses. A low geomagnetic period is reached during the workdays 126 - 129. Three different phases characterize the resistivity distribution during the workdays 126 - 130 for the XY component:

1. Between workdays 126 - 128 (comparably low seismicity), a significant minimum of apparent resistivity of 0.1 - 0.2 Ωm between 0.15 and 1 s, followed by a secondary minimum of about 0.3 - 1 Ωm between 2 and 7 s is observed. Note that both, particularly the secondary minimum, are more prominent at workdays 127 - 128.

2. With the onset of more prominent seismicity in frequency and magnitudes (workdays 128 - 129), the minimum of apparent resistivity between 0.15 and 1 s reduces to > 1 Ωm, while the "secondary minimum" remains at values < 1 Ωm.

3. With a peak in seismicity during the workdays 129 - 130, the apparent resistivity distribution of the reference is nearly recovered.

The changes in apparent resistivity are particular in the YX component and reveal one broad minimum of the same range during the workdays 126 - 127 and two similarly distinguished peaks from workdays 127 - 128. While in the XY component, the minima disappeared from workdays 129 - 130, the minimum at 0.1 - 1 s persists in the YX component. The phase follows the reference, and during workdays revealing apparent resistivity decreases, it is characterized by an increase in uncertainty and scattering (Comparable to cases 1 and 2).

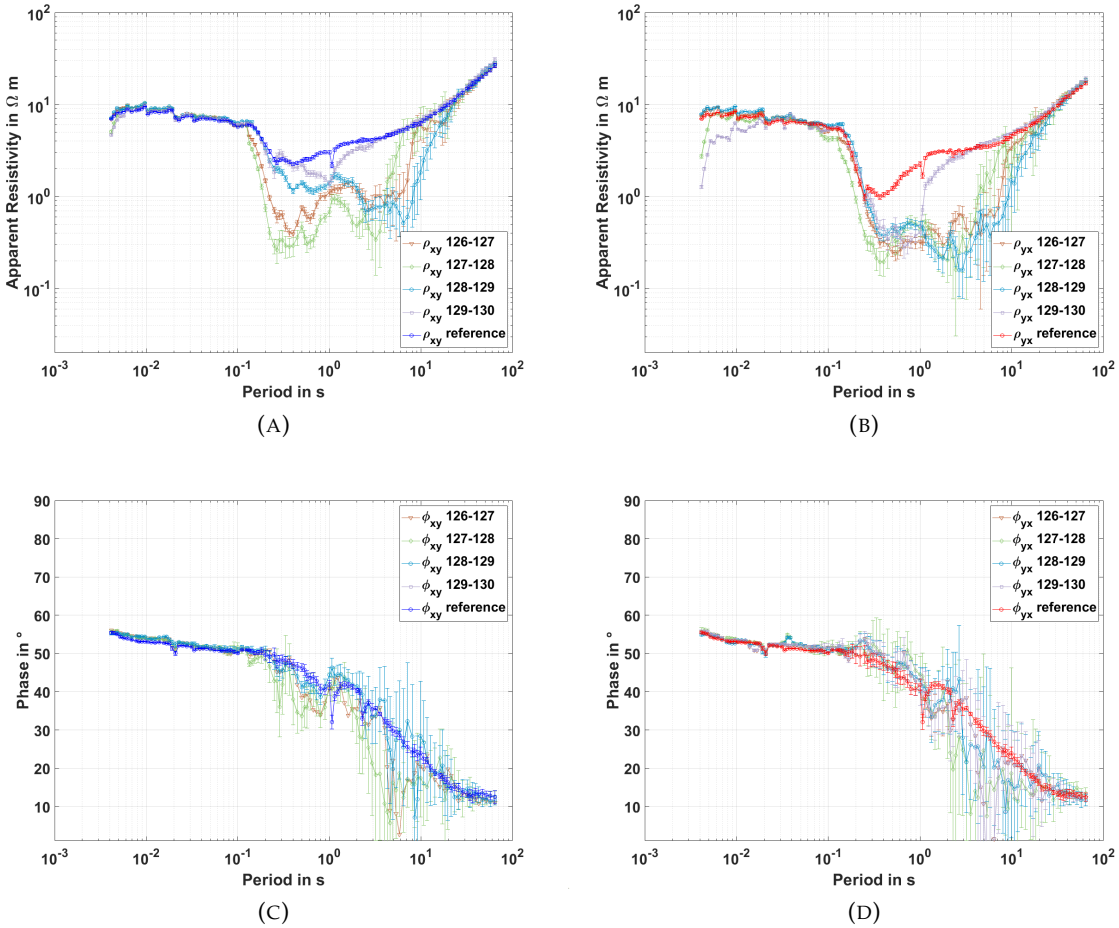

FIGURE 5.6: Transfer functions of the workdays 126 - 130 during total fluid loss for the XY component with a) apparent resistivity, and c) phase, as well as the YX component with b) apparent resistivity, and d) phases (Haaf and Schill 2021).

5.1.6 Regional seismicity

After the seismic event with a magnitude ML < 1 on workday 138, no local seismicity or fluid losses are observed during the workdays 139 - 141. The geomagnetic activity is low between workdays 140 - 141. The MT monitoring results reveal a decrease in apparent resistivity on both components starting from the workdays 137 - 138, comparable to the decrease in case 1 (Figure 5.7 a-b and 5.7 a-b). The data from the workdays 138 - 140 are characterized by the largest uncertainties and strongest scattering of the apparent resistivity and phase values of the entire survey (Figure 5.7 c - d and 5.8 c - d).

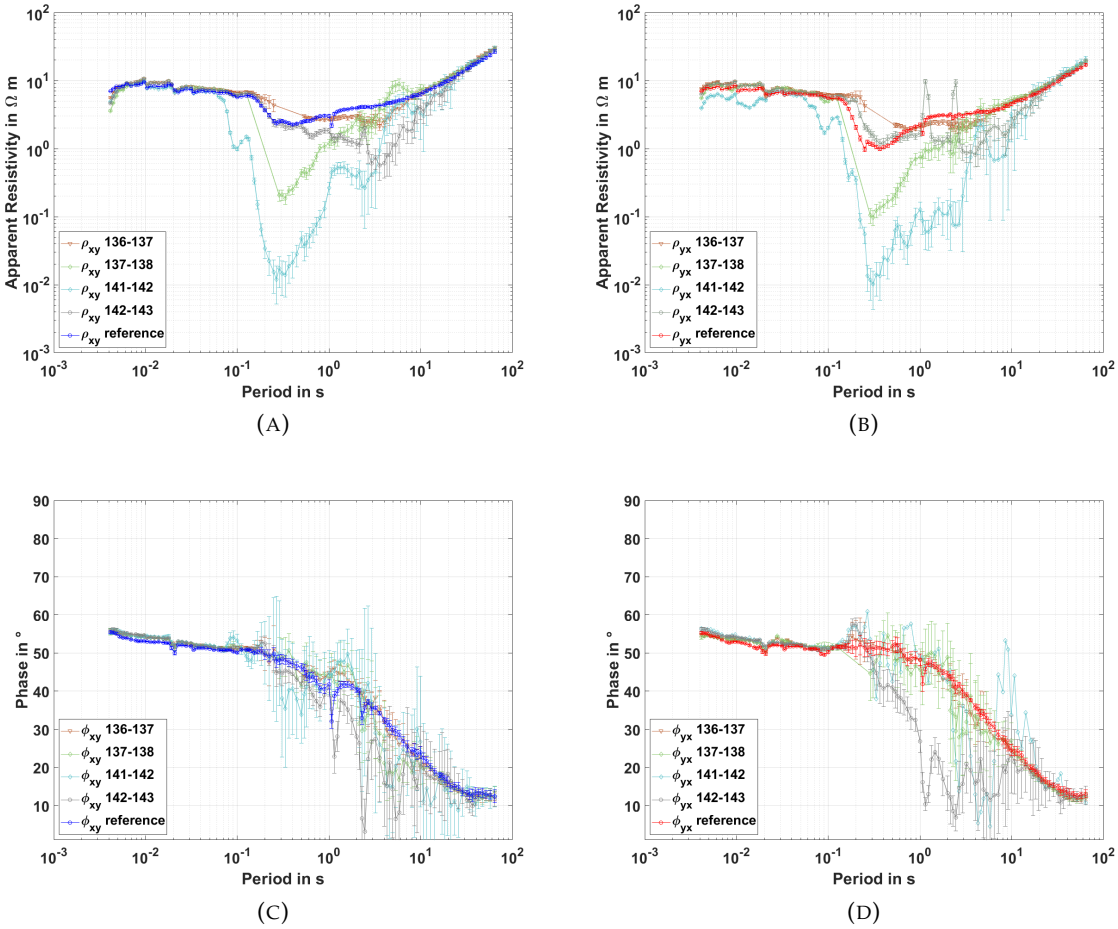

FIGURE 5.7: Transfer functions of the workdays 136 - 143 during total fluid loss for the XY component with a) apparent resistivity, and c) phase, as well as the YX component with b) apparent resistivity, and d) phases (Haaf and Schill 2021).

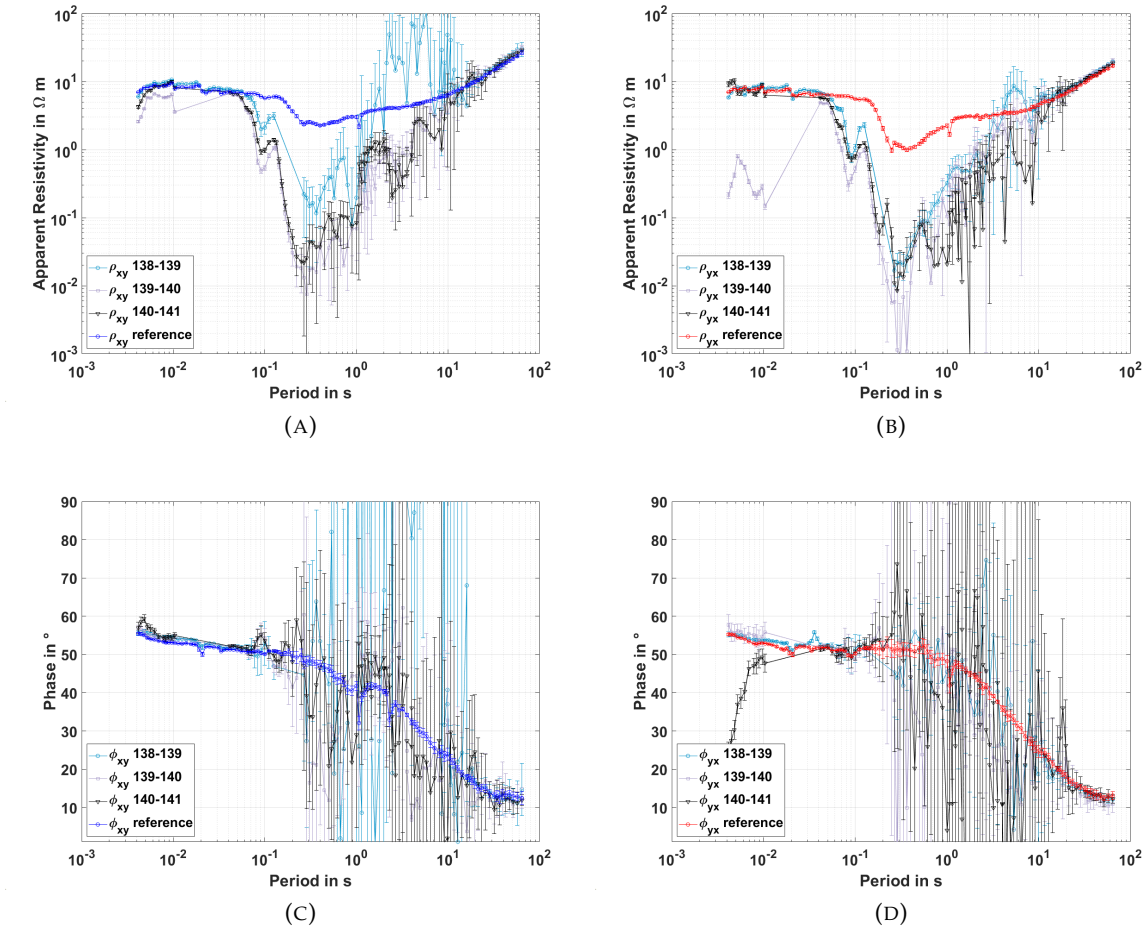

FIGURE 5.8: Transfer functions of the workdays 138-141 during total fluid loss for the XY component with a) apparent resistivity, and c) phase, as well as the YX component with b) apparent resistivity, and d) phases (Haaf and Schill 2021).

The phase improves during workdays 140 - 141. Uncertainties and scattering recover to values comparable to the observations in the cases 1 - 4 at workdays 141 - 142 (Figure 5.7 a - b and 5.8 a - b). The resistivity minimum persists during these workdays. Reference values are reached during workdays 142 - 143 when a cluster of seismic events characterizes the processes in the reservoir.

The SIL seismic network registered several seismic events in the vicinity of the well during this period. Several events occur close to the bottom hole depth of RN15/IDDP-2 including the ML = 1.45 event close to the well at 5'053 m TVD on workday 138. More events occur on the same day at distances of up to 60 km east from the borehole with ML up to 1.67 at 3'564 m TVD. Deeper seismic events of ML of 1.25 - 1.29 occurring on workday 140 at TVDs of 7'180 and 10'445 m up to about 60 km east of the borehole. Similar to workday 138, the events on workday 142 are accompanied by a series of similar and larger magnitude events about 60 km to the east in a depth range of about 2 - 5.5 km TVD.

5.2 Comparison of resistivity minima with the geomagnetic activity

A comparison between the Ap value and the apparent resistivity (YX component) is presented in Figure 5.9 to evaluate the influence of low magnetic activity on the MT signal and thus the deduced apparent resistivity in the subsurface. Low magnetic activity is defined by Ap values below the median value of Ap = 5 over the entire monitoring period. The Ap and the apparent resistivity values are calculated over 48 hours and shown in 24-hour windows.

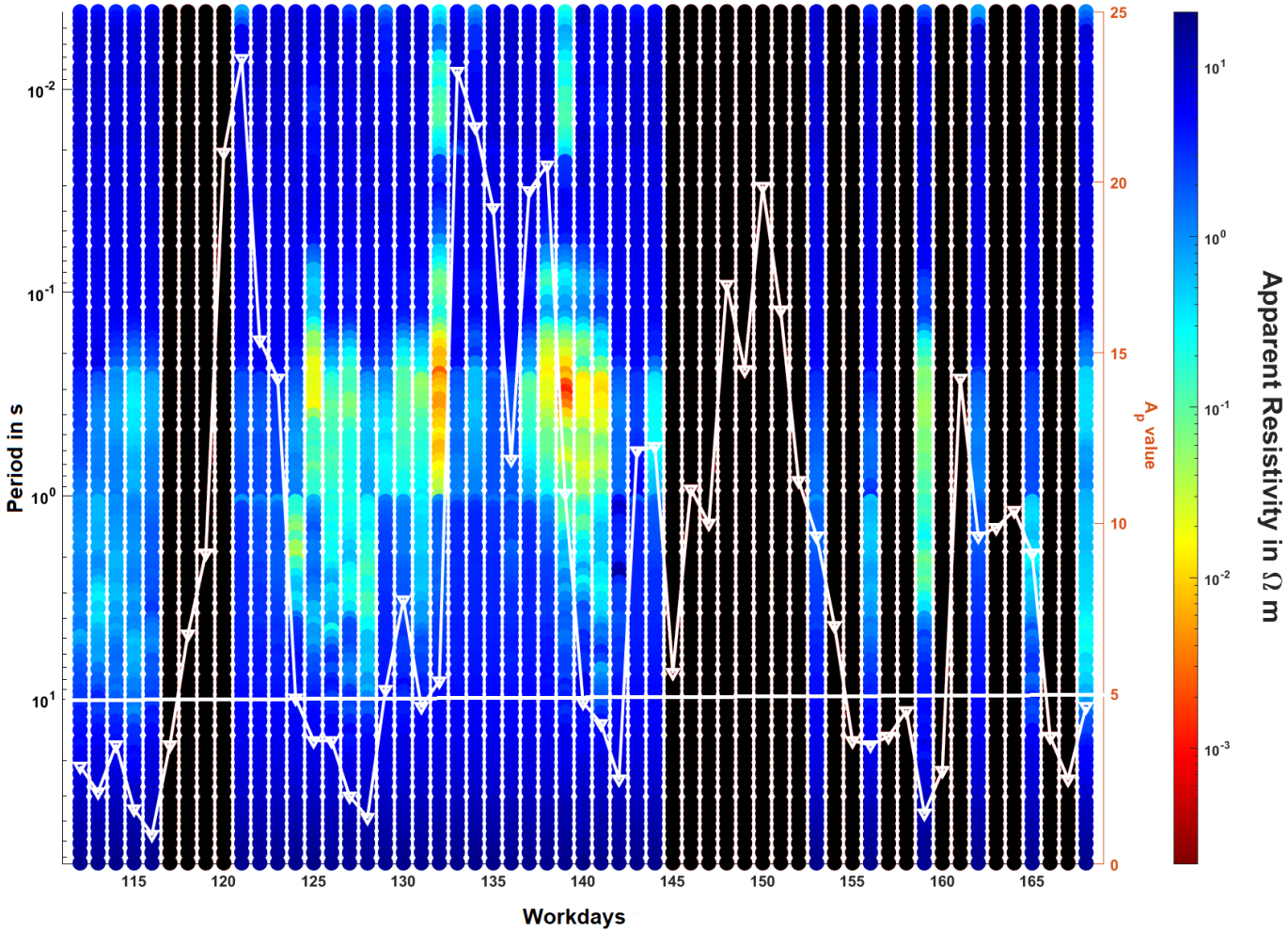

FIGURE 5.9: The geomagnetic activity as Ap value (GFZ German Research Centre For Geosciences 2020) with the apparent resistivity values (YX component). Both parameters are calculated over 48 hours and shown with a 24-hour window. The white horizontal line shows the median value of Ap = 5 and the fluctuating white line the daily Ap value. The black columns are days without MT data (Haaf and Schill 2021).

Although correlation coefficients between the resistivity minima and Ap values are very low (R2 values of 0.033 for XY and 0.0621 for YX), most of the

extreme resistivity minima (more than one order of magnitude lower compared to the reference) occur in periods of low magnetic activity except for the days 132 - 133, 134 - 135, 138 - 139 and 143 - 144. The extreme resistivity minima do not correspond to the local minima in the Ap value except for the 159 - 160. Furthermore, we observe a number of workdays (156 - 157, 129 - 130, 137 - 138) during low geomagnetic activity periods in which no minima are observed.

5.3 Estimate of resistivity changes by extensive fluid losses

A simple forward model is proposed to assess possible changes in electric resistivity during extensive fluid losses (Figure 3.6). Major fluid losses with an electric resistivity of 0.66 Ωm occur in the depth range between 2'900 and 3'300 m. At this depth, a porosity of 10 % is observed (T. Weisenberger et al. 2017).

In the first step, we compare the 1-D inversion of MT measurements at GUN from workday 79 (28/10/2016) to the resistivity distribution with depth from 3-D inversion (see Figure 3.3, (Karlsdóttir and Vilhjálmsson 2016)) and resistivity logs (Hydraulic Data RN-15/IDDP-2 2017) from the respective depth range (Figure 5.10). The determinant was inverted using a Levenberg-Marquardt scheme. Note that the 1-D inversion reveals the general low resistivity zone down to < 2'000 m depth that is characteristic for the area (Figure 3.3). This zone appears to be separated into two distinct layers, 200 - 300 m and 900 - 2'000 m at the MT station GUN in the 3-D inversion. This separation is not delineated in the 1-D inversion. This low resistivity cannot be found in the transfer function of GUN neither. Therefore, it might result from the TEM data included in the 3-D inversion but not in the 1-D inversion.

Furthermore, the 1-D inversion seems to underestimate the general resistivity provided by logging in the zone of high fluid losses. However, resistivity logging reveals several zones with resistivities reduced by up to one order of magnitude with respect to the matrix resistivity, i.e., about 100 - 200 Ωm. The thickness of these zones of reduced resistivity ranges between 5 and < 20 m summing up to about 40 m thickness and providing pathways for the massive fluid losses during drilling. The overall volume of the fluid losses during drilling is about 91'627 m^3, resulting in a freshwater lens with a radius of about 27 m. Against this background, we add a layer of 40 m with a by about one order of magnitude reduced resistivity (namely 0.66 Ωm) to investigate the effect of fluid losses on the MT data (dashed line in Figure 5.11).

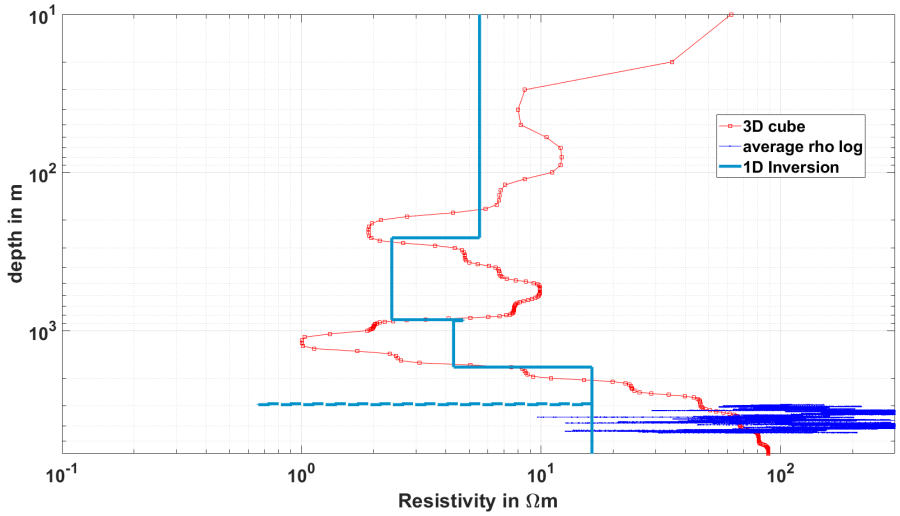

FIGURE 5.10: Resistivity distributions of the 3D model, the 1D inversion , the forward model and the resistivity log of the well RN-15/IDDP-2 (Haaf and Schill 2021).

Figure 5.11 reveals the low expected differences of 1 Ωm (and 3° in the phase) between the transfer function of the measured data at GUN and the results from forward modeling of the resistivity distribution with the depth of the 1-D inversion with the additional resistivity low resulting from the fluid losses. The resulting changes even overestimate the effect given the small radius of the freshwater lens.

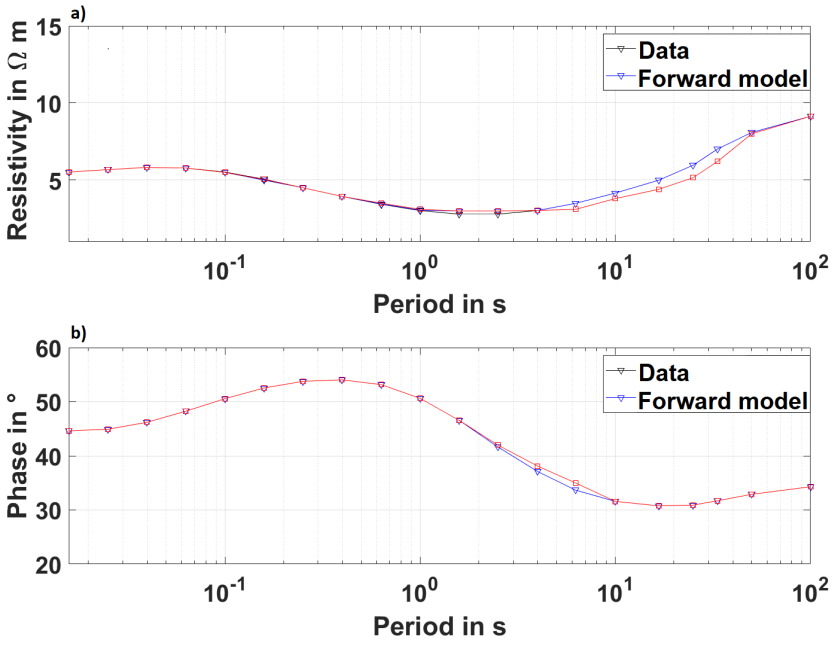

FIGURE 5.11: Obtained transfer function of the layered model (triangle) and the forward model with the resistivities (a) and the corresponding phases (b) (Haaf and Schill 2021).

5.4 Temporal changes in the phase tensor

The residual phase tensors are shown for the individual workdays in Figure 5.12 and compared to the geomagnetic activity. The phase tensors residuals are calculated after Caldwell et al. (2004) and Peacock et al. (2013) by subtracting the individual workdays from the reference workdays 46 - 47 (see equation 2.30). Thus, scalar differences are represented by a circular shape, while an ellipsoidal shape results in directional dependent changes (Peacock et al. 2013). Phase tensor residuals are determined in 48-hour windows.

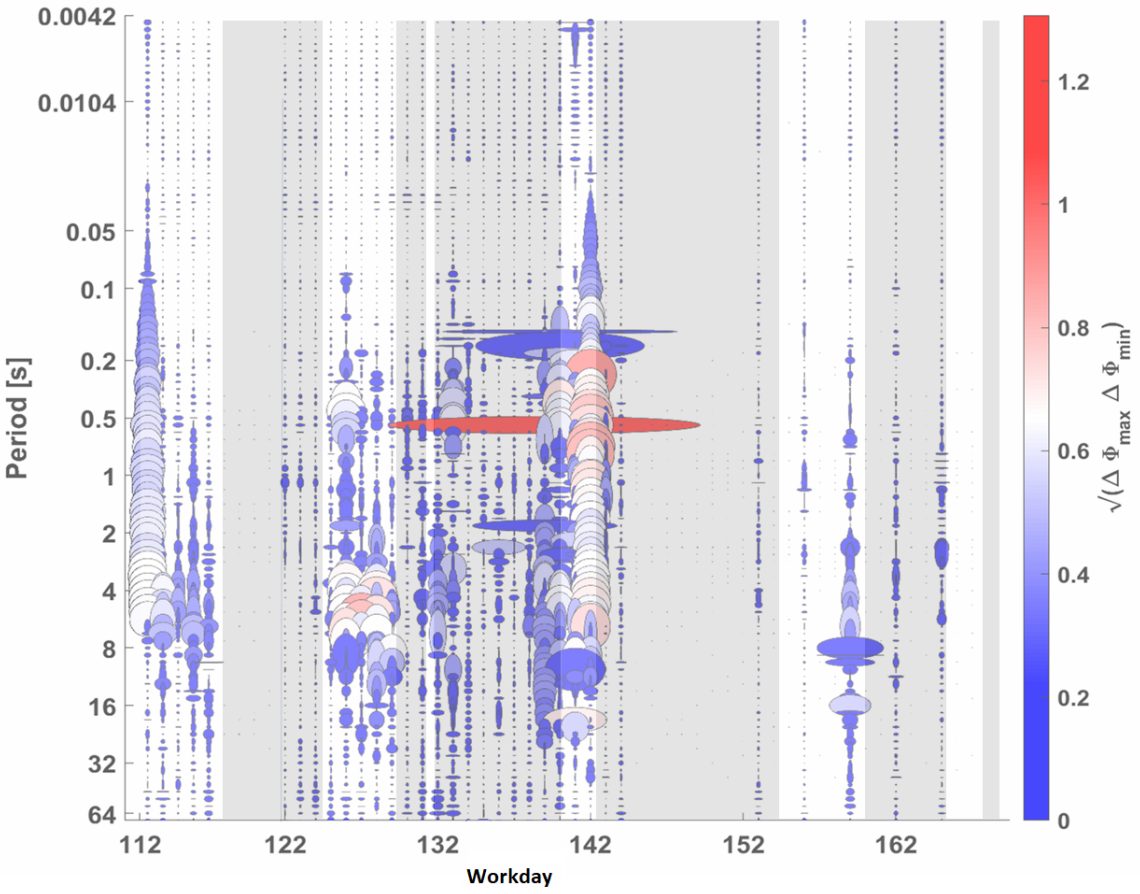

FIGURE 5.12: Overview of the calculated phase tensor residuals and intervals of geomagnetic activity (Ap values) above (grey) and below (white) the Ap median. The phase tensors residuals are calculated between the reference and the phase tensors of the corresponding workdays after Peacock et al. (2013) (Haaf and Schill 2021).

Generally, the geometric mean (color code in Figure 5.12) reveals differences of up to 30-40 % with respect to the reference. For periods < 0.05 s, the phase tensors show only slight differences from the reference. Changes between 50 - 65 % are observed in the period range of 4 - 8 s during the workdays 112 - 113, 126 - 129, and 142 - 143. The phase tensor residuals of the workdays 139 - 143 reveal the largest expansion between the periods 0.1 - 16 s and the highest percent changes with 60 - 100

The residual phase tensors predominantly show a circular shape; its predominant orientation is E-W whenever the shape becomes ellipsoidal. The

observation is consistent with the results obtained in the cases 1 - 5 that show more pronounced resistivity minima in the YX components than the XY components. This summary shows the highest percent changes in intervals of low geomagnetic activity, but there are also changes of up to 50 % in intervals of high geomagnetic activity.

5.5 Discussion

No consistent anthropogenic noise source, which correlates with the intervals and frequencies of the observations in the transfer functions, i.e., the decrease in apparent resistivity, could be detected in the time series or the power spectra. Filtering and decimation minimized the high-frequency anthropogenic noise. In addition, the time-frequency analysis shows that only the electric time series are affected by a periodic signal. This might be linked to tidal activity but with a frequency of $2.32 \cdot 10^5$ Hz, it is beyond the frequency range of interest (10^{-3}-10^2 Hz).

The goal of this study was to relate external geomagnetic, hydraulic, or seismic processes to the origin of the low resistivity anomalies. In this respect, three types of transfer functions are obtained during the MT monitoring of the deepening period of RN-15/IDDP-2. The phase of all three reveals enhanced uncertainties in the period intervals of 3 - 20 s. The type functions are distinguished by their distribution of apparent resistivity with the period. They occur temporarily related to geomagnetic, hydraulic, and seismic observations.

- No significant variation with respect to the reference workdays 46 - 47 are observed during workdays in which neither fluid losses nor significant induced seismicity observed, or during workdays in which no fluid losses but seismicity occurs, that is significant either in magnitude or in the number of events. Such transfer functions are observed during both low and high geomagnetic activity.
- Significant minima of resistivity between periods of 0.15 and 1 s with minimum resistivity values in the order of 0.1 Ωm and smaller occur during workdays preceding significant induced seismic events of either relatively large magnitude or a number of events. These minima are slightly more pronounced in the YX component. Two periods of the extreme minima fall into periods of low geomagnetic activity (workdays 125 - 126 and 159 - 160), while the other two coincide with transitional periods (workdays 132 - 133 and 139 - 140).
- During intervals of total fluid losses, secondary minima between of 4 - 8 s with a minimum value of about 1 Ωm are observed. Low geomagnetic activity accompanied all minima in this period range. However, the minima may also occur during workdays without fluid losses.

Although major resistivity minima usually occur during periods of low geomagnetic activity, this trend cannot fully explain the occurrence and absence of such minima. In Figure 5.13 we present a summary of the temporal coincidences between these processes to identify workdays with optimal constellations of high geomagnetic activity and hydraulic or seismic

processes. Optimal constellations at the workdays 122, 148, and 161 lack data before the seismic events occur. Furthermore, the simplified modeling showed that the fluid losses could not explain the amplitude of the observed resistivity decreases. The remaining optimal constellations at workdays 133 and 136 reveal an overlap with total fluid losses before workday 133 and a significant resistivity decrease at periods < 1 s (Figure 5.5).

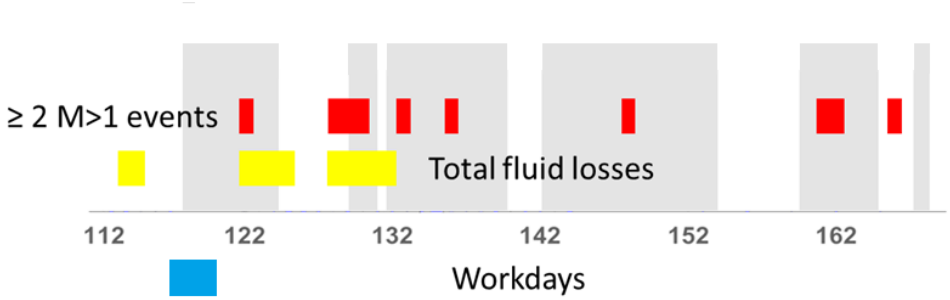

FIGURE 5.13: Summary of the temporal coincidence of high geomagnetic activity (grey), major seismic activity (red), and periods of total fluid losses (yellow) for the workdays 112 - 169 (Haaf and Schill 2021).

The attribution of this "noise" to geogenic processes is not conclusive because of this low number of optimal constellations. However, in comparison to earlier MT monitoring surveys mentioned in section 1, the following differences and similarities are observed (Table 5.2).

TABLE 5.2: Summary of the tectonic boundary condition and electromagnetic observations during injection experiments in EGS wells (Abdelfettah et al. 2018; Baujard et al. 2017; Didana et al. 2017; Haaf and Schill 2021; Peacock et al. 2013, 2012).

Orientation of \ Site	**Paralana**	**Habanero**	**Rittershoffen**	**RN15/IDDP-2**
SHmax	N110°E	N82±5°E	N170°E	N30°E
Seismic cloud	NNE-SSW, NE-SW	Horizontally extended with tendency to N-S, NNE-SSW orientation	n/a	Scattered with no specific induced swarms.
Geoelectric strike	N9°E	N50°E	N-S	N5°E
Residual phase tensor during injection	N-S, NNE-SSW	N-S	N170°E	isotropic to E-W
Significant resistivity minima component	XY ∥ N-S	XY ∥ N-S	YX ∥ E-W	XY ∥ N-S and YX ∥ E-W
Approx. frequency range of (resistivity) anomalies	2-20 s	17-34 s	8-20 s	0.15-1 s and 4-8 s

Note that the literature does not provide a detailed analysis of the Habanero site about the transfer functions. Hence, the discussion focuses on the comparison with sites of Paralana and Rittershoffen.

1. With two exceptions, the resistivity minima occur in a rather similar period ranges between 2, 4, and 8 to 20 s at Paralana, RN15/IDDP-2 (secondary minima), and Rittershoffen, respectively. Only at RN-15/IDDP-2 minima are observed at the period range > 0.2 s for the first time. The minima at Habanero are observed at longer periods of 17 - 34 s.

2. In contrast to the other sites, at the RN15/IDDP-2 well, significant resistivity minima are observed nearly equally distributed on both XY and YX components with slightly smaller values of apparent resistivities in the YX component.

3. Although revealing similar geoelectric strikes and residual phase tensor orientations during injection, the directional occurrence of the resistivity minima differs strongly between Paralana, Rittershoffen, and RN15/IDDP-2. While at Paralana, resistivity minima occur in the component parallel to the strike and residual phase tensor. At Rittershoffen, it occurs perpendicular to this direction, and at RN15/IDDP-2, it occurs in both directions.

4. The parallelism of the respective components with apparent resistivity minima are observed with the orientation of Shmin for Paralana, Habanero, and Rittershoffen and partly with the orientation of the seismic cloud at Paralana. Note that at Rittershoffen, no seismicity was observed. However, the significant minima in apparent resistivity occur perpendicular to the major fault zones (Baujard et al. 2017). At RN15/IDDP-2, Shmin (N120°E) is oriented between the two components; the seismic cloud is scattered and follows no specific induced swarm.

Chapter 6

Electric self-potential and electro-magnetic monitoring of hydraulic fracturing experiments in the Äspö HRL.

In the following, the results of the EMR and the SP monitoring will be discussed. The hydraulic data, namely flow rate, injection and packer pressure, are added in or to each Figure. Furthermore, the acoustic emissions are added in each Figure as magnitude M_{AE}. For a better overview, the number of the MF and RF cycle is added in the figures of the hydraulic data. Note that the textboxes' position is chosen for practical reasons and does not indicate any start or endpoints of the cycles.

6.1 EMR monitoring results

6.1.1 HF2

Figure 6.1 shows the a) burst energy and the b) hydraulic data and the AE events of HF2. The experiment started with a leakage test, followed by the MF and the five refrac cycles. Seven maxima are observed in the burst energy. Interestingly, the maxima are only observable during the injections, i.e., when the pumping is ongoing. Therefore, it is not possible to exclude the pump as a possible noise source. The EMR starts to increase during the leakage test at the beginning of HF3. The increase continues between the RF cycles until the end of HF2. At 8.30 am, the amplitude decreases before RF4 starts. A small peak in EMR is observed during the pressure release of RF4.

In total, 1577 AE events were detected in HF2. The amplitudes of the AE events are between 1 - 4, whereby the highest values occurred during the RF4 and RF5. In general, the amount of the AE events and the amplitudes are roughly increasing with time (number of RF cycles). This trend is also observable in the burst energy with an increasing amplitude from RF1 to RF5.

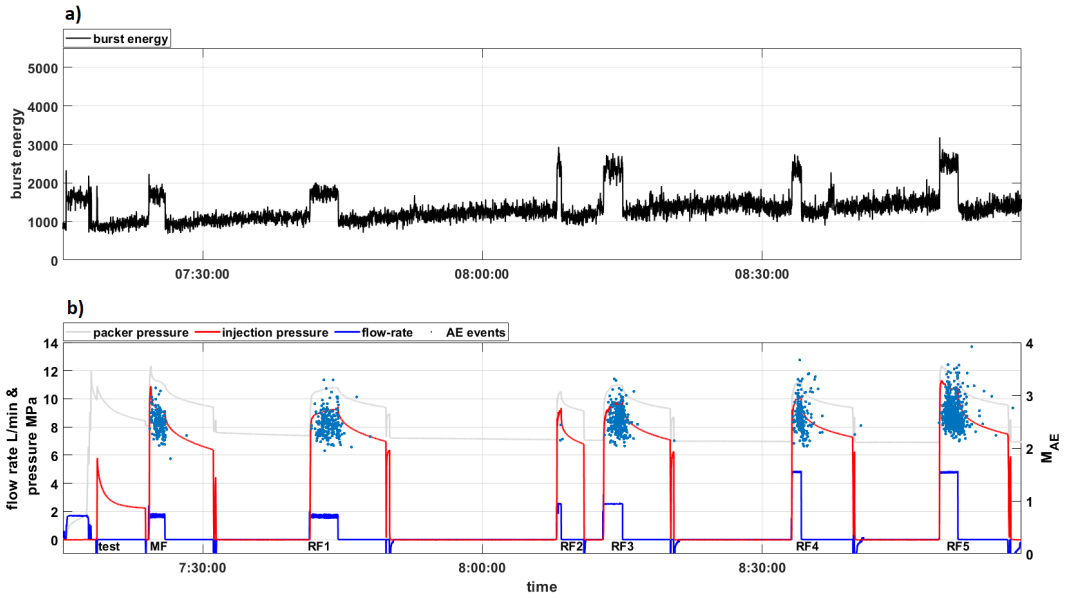

FIGURE 6.1: EMR results of HF2 with a) burst energy and b) the hydraulic data. The acoustic events are marked as blue dots, and their magnitude is at the right ordinate. The other quantities are at the left ordinates in a) with the burst energy in black and in b) with the flow rate in blue, injection pressure in red, and the packer pressure in grey.

6.1.2 HF3

Figure 6.2 shows a) the burst energy and b) the hydraulic data and AE events of HF3. The experiment started with a leakage test, followed by a stepwise flow rate increase and injection pressure. Finally, the MF occurs in step 5, as it can be seen in the pressure drop. The MF is followed by four RF cycles as in HF2 with a conventional injection scheme. As shown in Figure 6.1, maxima in burst energy are observed during pumping. In addition, thin peaks are seen during the pressurization and depressurization phases of the MF cycle. Again, pump noise cannot be ruled out as the cause of these maxima.

The EMR amplitude starts to increase during the leakage test at the beginning of HF3. Then, after each RF cycle, the EMR amplitude starts at a lower level than before the cycle but increases until the beginning of the next RF cycle. At 13:05 pm, the EMR amplitude decreases before the last RF cycle starts. In total, 606 AE events were detected in HF3. Almost half of them were measured in the last RF cycle.

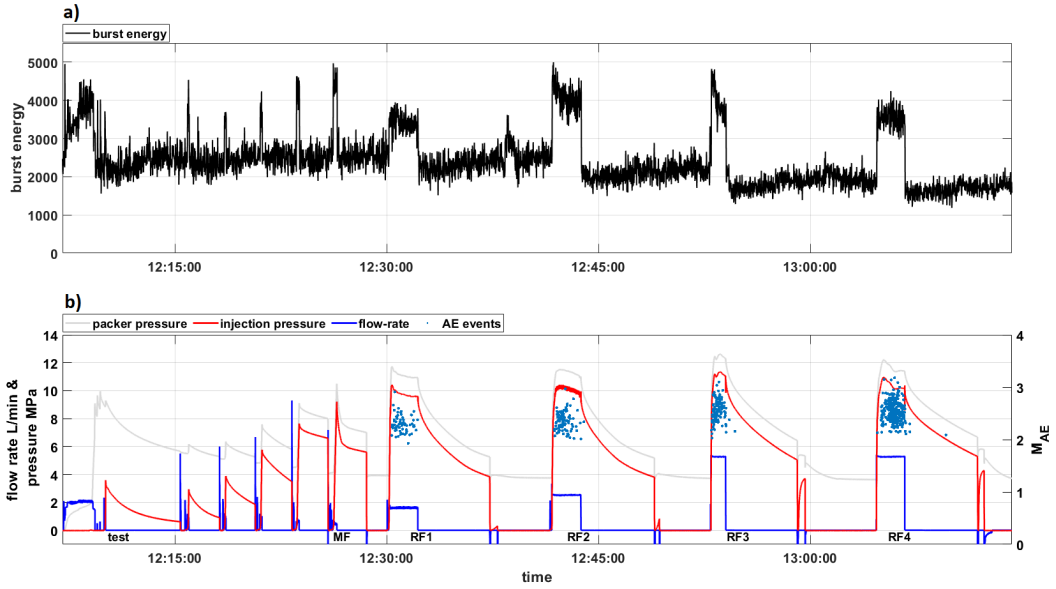

FIGURE 6.2: EMR results of HF3 with a) burst energy and b) the hydraulic data. The acoustic events are marked as blue dots, and their magnitude is at the right ordinate. The other quantities are at the left ordinates in a) with the burst energy in black and in b) with the flow rate in blue, injection pressure in red, and the packer pressure in grey.

6.2 SP monitoring results

The Figures 6.3 and 6.4 give an overview of the SP data during the HF experiments. The black vertical lines mark the start and endpoints of the HF experiments. In addition, a big machine stopped running shortly after the start of HF2, and the ventilation stopped during HF3. An earthquake occurred at the Reykjanes Ridge with a magnitude of 5.1 during HF3 at 12:17:06.6 pm.

The SP amplitudes in the near field vary between -250 mV and 450 mV during HF2 and between -250 mV and 80 mV during HF3. Note that SP1 was excluded from the far field data due to a male functioned electrode.

The amplitudes in the far field are between -380 mV and 20 mV for HF2 and -180 mV and 20 mV for HF3. The difference between the near and far field is the amplitudes in the near field are almost twice as large. Moreover, a phase shift is observed in the major maxima and minima in the near field.

The background signal is reached about 40 minutes after the end of HF2 and HF3. In the far field, this is only observed for HF2. The SP amplitudes of HF3 of the far field do not show significant amplitude ranges compared to the other SP data. The decrease of about 100 mV before the start point of HF3 remains in question. Nothing was found in the technical reports that might have explained the drop before the experiment started.

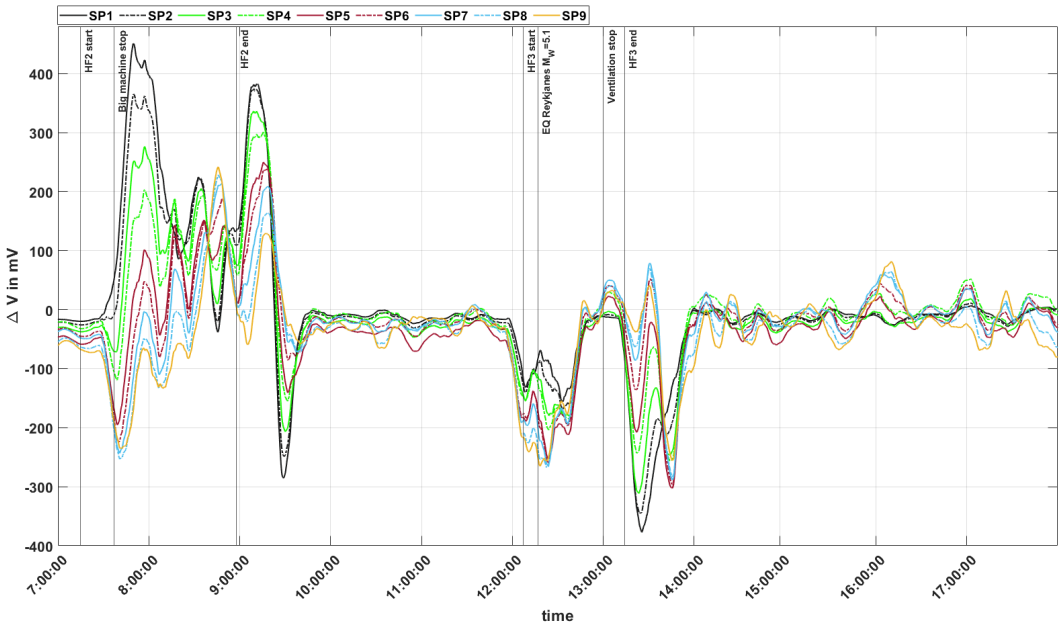

FIGURE 6.3: The overview of the SP data of the near field. The black vertical lines mark the start and end point of the experiments HF2 and HF3, the time a big machine stopped running and when the ventilation stopped. An earthquake occurred at the Reykjanes Ridge with a magnitude of 5.1 during HF3.

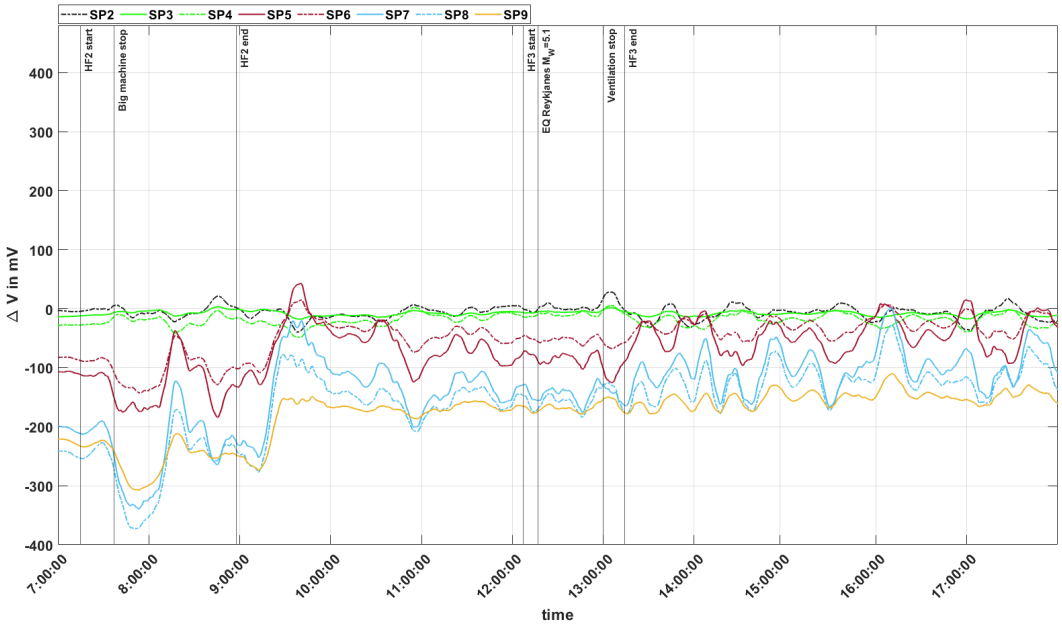

FIGURE 6.4: The overview of the SP data of the far field. The black vertical lines mark the start and end point of the experiments HF2 and HF3, the time a big machine stopped running and when the ventilation stopped. An earthquake occurred at the Reykjanes Ridge with a magnitude of 5.1 during HF3.

6.2.1 HF2

Figure 6.5 shows the SP signals of the near field, the hydraulic data, and the AE events of HF2. The SP amplitudes vary from -250 mV to 450 mV during the experiment. The SP1 - SP2 amplitudes begin to increase in the shut-in phase of the MF while the SP3 - SP9 reveal first a decrease followed by an increase of 150 - 300 mV. The maxima go through all SP distributions from over 400 mV in SP1 down to SP9 with an amplitude of -60 mV. Moreover, a shift of about 10 minutes is observed from the first peak in SP1 to the maximum in SP9. Three smaller maxima are observed between the RF3-RF5. The first maxima start after the shut-in phase in RF3 for SP2 - SP9, followed by the second one for SP1 - SP5 and the last one for SP6 - SP9. In between two minima for SP2 - SP9 and SP1 - SP4 are observed. The second-largest maxima in Figure 6.5 are observed after the pressure release of RF5. Again, the maxima go through all nine SP distributions starting in SP1 with values up to 380 mV and going down to SP9 and about 120 mV with a phase shift of a few minutes.

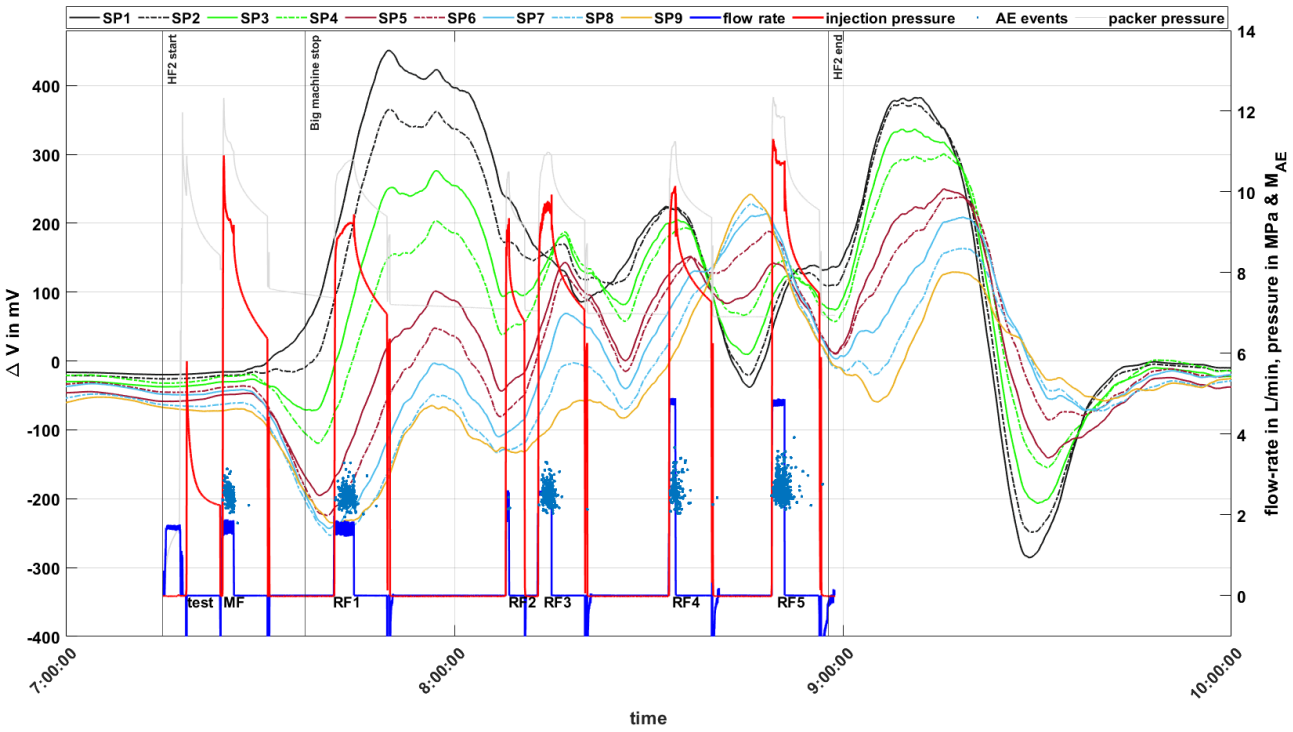

FIGURE 6.5: SP results of HF2 of the near field. The SP1 - SP9 distributions are shown in (dotted) lines in black, green, red, blue and yellow. The flow rate is in blue, the injection pressure in red and the AE events as blue dots. The black vertical lines mark the start and end point of the HF2 experiment.

In the far field, the amplitudes vary from -380 mV to 20 mV during HF2 (see Figure 6.6). In contrast to the near field, the distributions are clustered in small groups with SP2 - SP4, SP5 - SP6, and SP7 - SP9. SP1 was excluded from the discussion due to a male-functioned electrode. During the shut-in of the MF, the SP7-SP8 have a small increase of a few mV before revealing minima with values down to -380 mV. SP5 - SP6 and SP7 - SP9 show synchronous

behavior in maxima and minima. The SP2 - SP4 revealed amplitudes between -40 to 20 mV throughout the experiment without significant maxima or minima. In general, the amplitude ranges are half as large as in the near field. After the pressure release in RF5, the amplitudes need about 15 minutes to reveal increases of about 150 - 200 mV in SP5 - SP9. Afterward, the amplitudes reach the background signal.

In total, 1577 AE events with a magnitude up to 3.92 occurred during HF2. Most of them occurred during RF5.

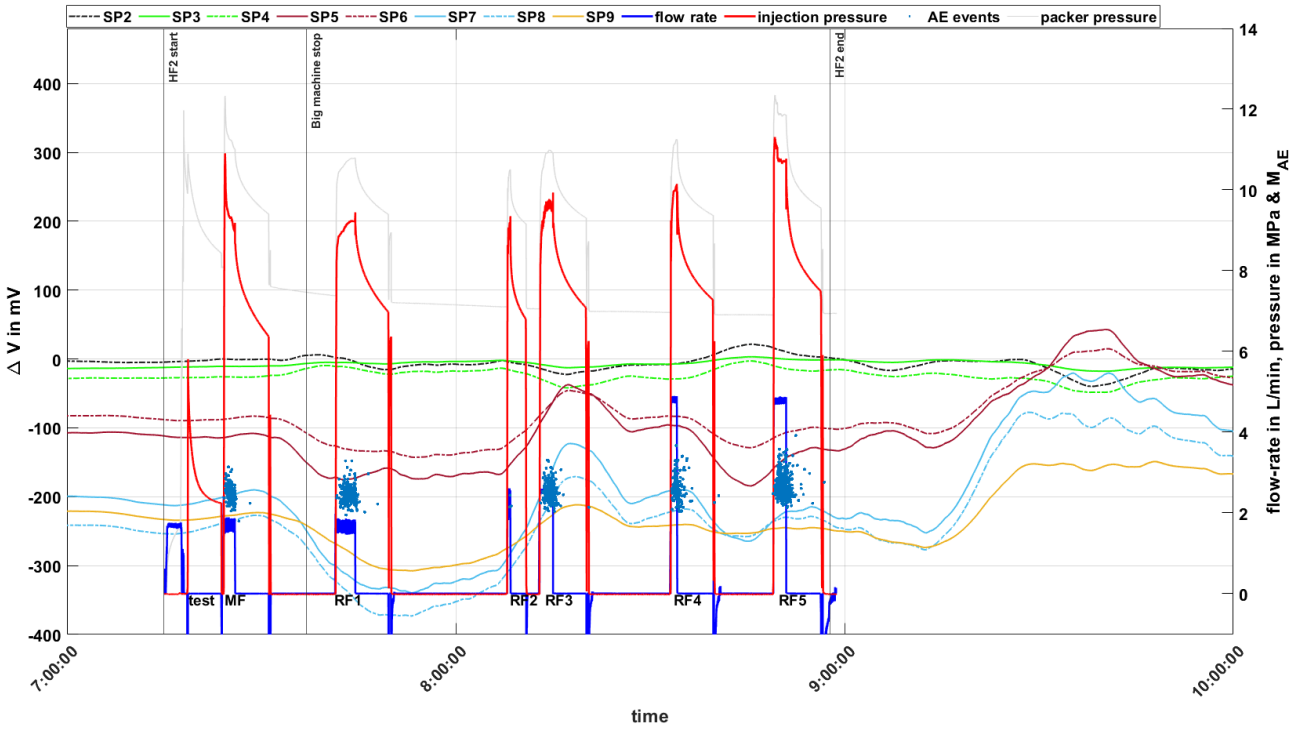

FIGURE 6.6: SP results of HF2 of the far field. The SP1-SP9 distributions are shown in (dotted) lines in black, green, red, blue and yellow. The flow rate is in blue, the injection pressure in red and the AE events as blue dots. The black vertical lines mark the start and end point of the HF3 experiment.

6.2.2 HF3

Figure 6.7 shows the SP signals of the near field, the hydraulic data, and the AE events of HF3. The SP amplitudes vary between -280 mV up to 50 mV during HF3. The observed decrease of about 100 to 200 mV before the start of the HF3 experiment remains an open question. It occurs outside of any activity in the vicinity of the experiment. Consequently, the HF3 initiates at such negative potential differences.

During the pressurization and depressurization stages, the SP amplitudes show only minor variations of about 50 mV. After releasing the pressure of the RF1 and the first cluster of AE events, the SP amplitudes increase by about 200 mV for SP1 - SP9. No shift is observed in the maxima. During the re-fracs 2 - 4, only minor changes are observed. However, after the pressure

release in RF5, the SP data reveal first minima followed by maxima in SP1-SP9. The minima reveal a shift of about 5 minutes from SP9 to SP1. The maxima with values up to 80 mV show a shift from SP9 to SP1 of about 5 minutes.

In total, 606 AE events occurred during HF3. Most of them occurred during RF4.

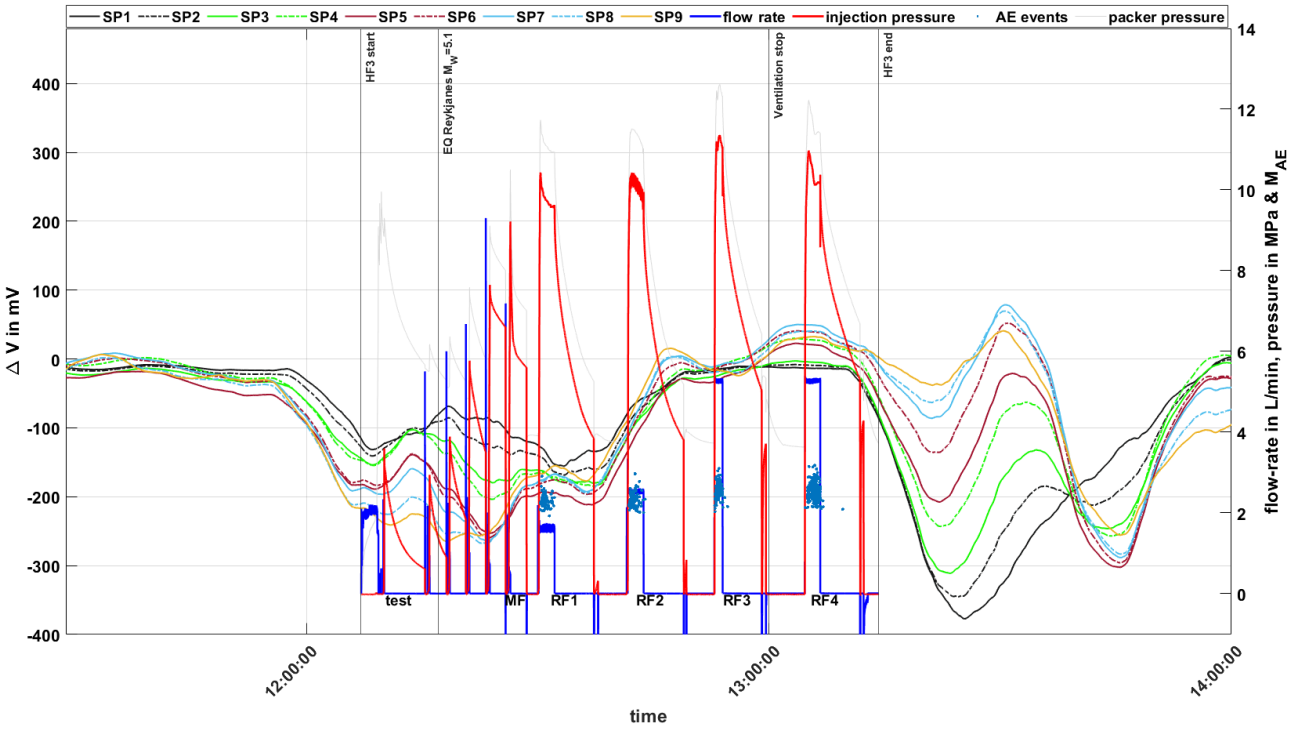

FIGURE 6.7: SP results of HF3 of the near field. The SP1 - SP9 distributions are shown in (dotted) lines in black, green, red, blue and yellow. The flow rate is in blue, the injection pressure in red and the AE events as blue dots. The black vertical lines mark the start and end point of the HF3 experiment.

Figure 6.8 shows the SP signals of the far field, the hydraulic data and the AE events of HF3. The amplitude vary between -180 - 20 mV. In general, no significant changes are observed during HF3 In the far-field sensors, only small variations of 20 - 50 mV during the re-frac 2 - 4.

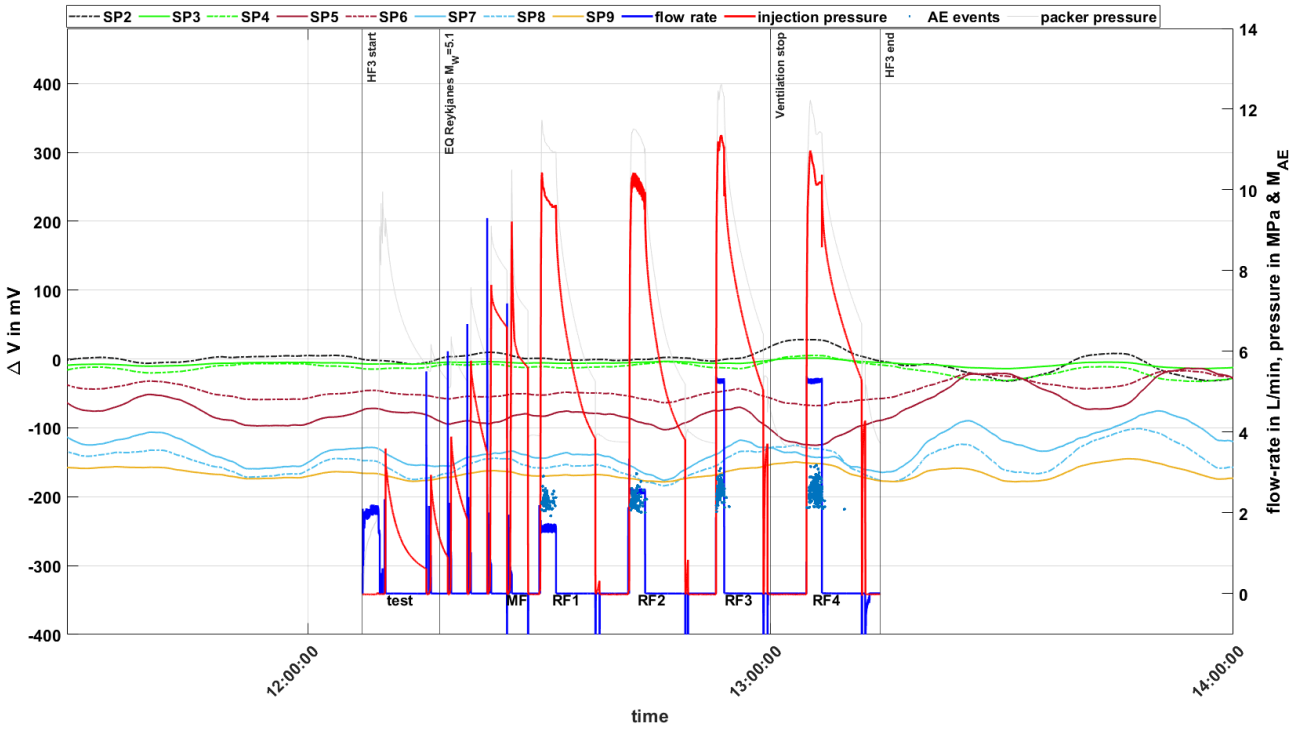

FIGURE 6.8: SP results of HF3 of the far field. The SP1 - SP9 distributions are shown in (dotted) lines in black, green, red, blue and yellow. The flow rate is in blue, the injection pressure in red and the AE events as blue dots. The black vertical lines mark the start and end point of the HF3 experiment.

6.3 Discussion

SP and EMR monitoring of two hydraulic fracturing experiments, HF2 (conventional) and HF3 (fatigue hydraulic fracturing), took place at underground-lab-scale to investigate differences in the mechanic response to different fluid injection schemes.

The EMR results show maxima during the pumping process in both experiments. Thus, the pump could generate the noise signal in the EMR data. Besides the maxima, the EMR amplitudes increase between the (re)frac cycles in both experiments. HF2 shows a nearly constant increase in amplitude with time. In contrast, the EMR amplitudes in HF3 reach the highest values already during the pressurization steps and then decrease throughout HF3 as they start with lower values after each cycle, although they increase between the cycles.

In HF2, a good correlation between AE activity and EMR amplitude can be seen. On the one hand, the number of AE events increases with the refraction cycles, injection pressures, and EMR amplitude. Moreover, the highest AE magnitudes are seen during RF5. On the other hand, in HF3, there is a difference from HF2 in terms of the number and magnitude of AE. While in HF3, many small fracture planes are observed with switching strikes and dips, and in HF2, it is a planar, elongated fracture plane with stable orientations (Niemz et al. 2020). However, despite the differences in AE results,

the EMR results show more similarities. In particular, the increase in EMR amplitude after the noise maxima, i.e., after shut-in, shows a possible inverse correlation between EMR increase and pressure drop.

The SP results show time-delayed amplitude changes for the near-field sensors in both experiments. However, for the far-field sensors (about 150 - 200 m away from the experiment), such changes are observed only during the HF2 experiment. Moreover, the background signal is reached about 40 minutes after the last pressure release. Thus, the time interval between cycles might be too short to bring the SP back to the background signal level. For example, after the six-day injection at Soultz-sous-Fôrets, it took several days for the SP amplitudes to return to a level almost equal to the pre-injection condition (Marquis et al. 2002).

The highest values are measured in the near field during HF2 with values from -250 to 450 mV and during HF3 with values from -200 to 50 mV. In the far field, the amplitude range is from -380 mV to 20 mV during HF2 and from -200 to 20 mV during HF2. The distance between the near and far field to the test location can explain the difference in amplitudes. The nearly double amplitudes of HF2 compared to HF3 could be due to the injection scheme. The permeabilities in HF2 are nearly double as high as during the progressive injection (see Table 3.3).

In general, the minima and maxima between the individual injection steps are in phase. In contrast, after completing the two experiments, HF2 and HF3, the major minima and maxima are characterized by a significant phase shift. Compared to other reservoirs- and laboratory-scale studies, a few hundred mV amplitude ranges match well between the few mV changes at Soultz and the hundreds to thousands of mV obtained in the Oklahoma laboratory test. Large SP amplitudes in injection experiments are often produced by electrokinetic effects (Hu et al. 2020; Pritchett and Ishido 2005). This could explain the long duration of the background signal to return to normal (see Marquis et al. (2002) and Darnet et al. (2004)). However, the spatial distribution of the electrodes contradicts the theory of electrokinetic effects. All electrodes in the near and far fields are spatially located on one side of each experiment. Therefore, all electrodes would have been synchronously affected by a change in the flow direction, and the large maxima and minima would not have been shifted to each other.

Furthermore, possible electrothermal effects can be neglected since no tempered water was injected. Possible electrochemical effects are calculated according to Maineult et al. (2005) and Darnet et al. (2004). The computation can be found in the appendix B.3. The voltage ranges of the electrochemical potential vary around -0.03 - 0.06 mV and are thus $<<$ of several hundred mV observed during the experiments.

Similarities between SP and the AE activity are observed in Äspö. In particular, the large maxima after HF2 in the near field with values up to 380 mV may be correlated to the AE activity during RF5. Thus, the highest values and the largest number of AE events are observed in RF5. In addition, upward migration of AE events is observed, which did not occur in the previous RF phases (Niemz et al. 2020). The distribution of the fracture planes obtained during HF2 shows the upward migration, especially in the last fracture plane (see Figure 3.19). Moreover, the largest injection pressures occurred in RF5

and exceeded the MF pressure. Similar observations were made at Soultz-sous-Fôrets. Schoenball et al. (2014) observed migration of induced seismic events in the shut-in phase to previously inactive areas. This is also the period when seismic energy release is highest (Schindler et al. 2010). Furthermore, the second increase in SP amplitude was observed during the pressure shut-in. Such a clear correlation to the shut-in phase was not seen here in data from Äspö HRL.

To summarize the results obtained in the Äspö HRL, one of the objectives of this study was achieved by adding a new set of electrical and electromagnetic data obtained during the laboratory-scale subsurface injection tests. However, research questions remain regarding the relationship between pressure and SP/EMR signals.

Chapter 7

Synopsis discussion and conclusion

This thesis contributes to an interpretation of SP and EM signals in terms of possible electrokinetic and seismo-electric effects in different data sets obtained during hydraulic injection experiments.

The studies took place at the reservoir- and underground-lab scale at Reykjanes and Äspö HRL. Besides SP, EM, and MT measurements, data acquisition also involves seismic and acoustic emissions, respectively. The latter is a consequence of injection into a highly fractured environment in Reykjanes and hydraulic fracturing in the case of Äspö. Frequencies of the related seismic and EM emissions are scale-dependent, i.e., kHz- and Hz ranges are observed at the underground lab and reservoir scale, respectively. In the SP observations, potential differences are monitored in the mV to hundreds of mV (compared to thousands of mV in lab experiments, e.g., Hu et al. (2020)) on the reservoir- and underground lab levels, respectively.

In the following, the data are discussed first with a focus on the reservoir- and underground lab scale and then framed by the lab- as well as crustal scale.

The experiments at reservoir-scale were electromagnetically monitored using MT. The results of this study show a temporal relation between decreasing apparent resistivity in the period ranges of 0.15 -1 s and 4 - 8 s and (i) the geomagnetic field activity, (ii) the fluid losses up to 60 L/s, as well as (iii) mechanic processes occurring prior to induced seismicity. Against this background, the full physical meaning of the apparent resistivity changes remains a matter of debate. Note that forward modeling of the effect of the injected water volume could not explain the observed resistivity changes.

In the following, it is compared to earlier observations at the reservoir and crustal scale to shed light on its temporal coincidence with clusters of induced seismicity and fluid injection. The typical period ranges of the observed resistivity anomalies at the reservoir-scale (Table 8.3) extend over 2 - 34 s in all studies. At the RN-15/IDDP-2 well, this is completed by a second minimum at lower periods ranging between 0.15 - 1 s. The temporal coincidences with induced seismicity, i.e., the occurrence of MT signals up to 24 h prior to seismic clusters, and fluid injection concern the period range < 1 s and > 1 s, respectively. At crustal scale, EM emissions several days to hours prior to large-scale earthquakes are observed at periods < 1 s with a median value of $1.5 \cdot 10^{-4}$ s (Petraki et al. 2015). Note that in the Habanero and Paralana projects, a pronounced orientation of the residual phase tensors develops during periods with significant resistivity minima. In both projects,

the seismic clouds develop in a preferential direction that, however, shows a slight angle to the residual phase tensor (Didana et al. 2016; Peacock et al. 2012). In Rittershoffen, the decrease of resistivity develops only on the component that is parallel to Shmin (Abdelfettah et al. 2018). Significant changes in the maximum principal component of the phase tensor and its orientation are not observed (Abdelfettah et al. 2018). In contrast to these different directional observations, the results from Reykjanes show that (i) both MT components are affected by the minima, and (ii) the residual phase tensor shows a mostly isotropic shape. This lack of directionality is again consistent with the evolution of the seismic cloud during injection, which also reveals no clear directional behavior.

A number of studies at lab scale indicate, similar to the variation in mechanic response to deformation, a variation in the related electric or electromagnetic signal for different rock types (Freund 2011; Wei et al. 2020). The largest effects are observed in granite and other igneous rocks. Two of the reservoir-scale experiments that were MT monitored were carried out in granitic rock (Habanero and Rittershoffen projects). Note that response in SP was also obtained during monitoring hydraulic stimulation in the granitic reservoir of Soultz-sous-Forêts. Basaltic and metasedimentary rocks were not investigated at the lab scale. However, no significant difference between the Paralana (Mesoproterozonic metasediments) and Habanero MT monitoring projects is observed. An influence of the basaltic rock type of Reykjanes on the MT response to fluid injection, e.g., the shift to higher frequencies, must be investigated in future lab experiments.

TABLE 7.1: Summary of the tectonic and hydraulic boundary conditions (grey) as well as the seismic and electromagnetic observations during injection experiments in EGS wells (Abdelfettah et al. 2018; Baujard et al. 2017; Didana et al. 2017, 2016; Peacock et al. 2013, 2012).

Orientation of \ Site	Paralana	Habanero	Rittershoffen	RN-15/IDDP-2
Engineering step	Massive hydraulic stimulation	Massive hydraulic stimulation	Injection	Drilling
Rock type	Metasediment	Granite	Granite	Basalt
Max. pressure	62 MPa	48 MPa	1-3 MPa	8 MPa
Max. flow rates	58 L/s	53 L/s	28 L/s (GRT1) 42 L/s (GRT2)	55 L/s
Volume	3'100 m^3	36'500 m^3	175 m^3	91'627 m^3
Approx. period range of (resistivity) anomalies	2-20 s	17-34 s	8-20 s	0.15-1 s 4-8 s
Significant resistivity minima component	XY ∥ N-S	XY ∥ N-S	YX ∥ E-W	XY ∥ N-S and YX ∥ E-W
Orientation of the seismic cloud	NNE-SSW, NE-SW	Horizontal with tendency to N-S, NNE-SSW	n/a	Random distribution
Orientation of the max. of residual phase tensor during injection	N-S, NNE-SSW	N-S	N170°E	isotropic to E-W

Hydraulic fracturing experiments at underground lab scale, HF2 (conventional) and HF3 (fatigue hydraulic fracturing), were SP and EMR monitored. Changes in SP have been observed with a temporal delay in both experiments in the near-field sensors (about 50 - 70 m distance from the experiment). However, in the far-field sensors (about 150 - 200 m from the experiment), such changes are observed only during the HF2 experiment. Furthermore, the background signal is reached about 45 minutes after the last pressure release. Generally, minima and maxima obtained from different electrode offsets that occur between the individual injection steps are in

phase. In contrast, the major minima and maxima after completing the two experiments, HF2 and HF3, are characterized by a significant phase shift.

In the near field, the SP amplitudes begin to increase in the shut-in phase of the MF for the electrode pairs with an offset of 5.75 and 15.58 m, while pairs with a larger offset reveal first a decrease followed by an increase in self-potential. Minima (-250 to -80 mV) are reached after 25 minutes and are followed by maxima. Maxima (-80 to 450 mV) are reached after 35 to 40 minutes for offsets between 5.75 - 51.33 m. Lower fracture re-opening pressures of 6.7 - 7.5 MPa characterize follow-up re-fracs compared to the breakdown pressure of 10.9 MPa in the MF. This is reflected in local maxima and minima of about half of the initial amplitude in the SP signal. A distribution of maxima and minima that is similar to the MF is observed for re-frac No. 5. In this re-frac, the injection pressure exceeds the breakdown pressure by about 3.5 MPa. The initial SP background is re-established at about 40 minutes after the pressure release of re-frac no. 5. In the far-field, the SP amplitudes begin to decrease in the shut-in phase of the MF for the electrode pairs with an offset between 34 - 88 m and followed by an increase in self-potential. The maxima are reached after the shut-in of the re-frac No. 3 (after about 1 hour). The electrode pairs with an offset of 9.5 - 24.5 m reveal small variations in the SP amplitudes between -30 to 20 mV. As for the near field, the initial SP background is reached at about 50 minutes after re-frac No. 5.

The observed decrease of about 100 to 200 mV prior to the start of the HF3 experiment remains an open question. Consequently, the HF3 initiates at such negative potential differences. The period of cyclic injection is characterized by local minima and maxima between about 35 and -150 mV. Comparably to MF in HF2, during the first re-frac in HF3, SP remains rather constant. An increase is observed after the pressure release of re-frac 1. During the re-fracs 2 - 4, only minor changes are observed. In the far-field sensors, no significant changes are observed during HF3.

Table 7.2 compares results obtained in Äspö HRL to SP monitoring of hydraulic injection experiments at reservoir level (Soultz-sous-Forêts) and lab scale (Oklahoma lab), as well as mechanical loading experiments (Nasa lab). It details the SP that decreases with the increasing distance of the sensors to the experiment. In some hydraulic experiments, a delay in the SP response with respect to the start of injection is observed. In Soultz-sous-Forêts, the SP amplitudes increase after 12 hours after the injection starts. In Äpsö HRL, it was about 15 minutes, and at the lab scale, no shift was observed. The experiments of Soultz-sous-Forêts and Äspö HRL are characterized by different injection schemes, including a pressure shut-in phase after hydraulic shearing/fracturing. A significant increase in SP of 3 to 4 mV is observed in Soultz-sous-Forêts (Marquis et al. 2002). Schoenball et al. (2014) observed contemporaneous migration of induced seismic events in the shut-in phase to previously inactive areas. This is also the period when seismic energy release is highest (Schindler et al. 2010). Similar observations can be made for the HF2 experiment. The largest AE magnitudes are observed during the shut-in phase of RF5, in which the injection pressure exceeds the break-down pressure in the MF. In addition, upward migration of AE events is observed that did not occur in the previous RF stages (Niemz et al. 2020). After pressure release, relaxation of SP to the previous amplitude levels continued over

several days (Darnet et al. 2006). In the HF2 experiment, the major maxima are temporally delayed with respect to the MF and the RF5. They consist of two local maxima. A clear correlation to the shut-in phase is not evident. In HF3 double peaks are not observed.

TABLE 7.2: Summary of the tectonic and hydraulic boundary condition and self-potential observations during hydraulic injection in Soultz-sous-Forêts, Äspö HRL and Oklahoma lab and mechanical loading experiments in the Nasa lab (Darnet et al. 2004, 2006; Freund 2011; Hu et al. 2016, 2020; Marquis et al. 2002).

Orientation of \ Site	Soultz-sous-Fôrets	Äspö HRL	Oklahoma lab	Nasa lab
Engineering step	Massive hydraulic stimulation	Hydraulic fracturing	Hydraulic fracturing	Mechanic loading
Rock type	Granite	Granodiorite	Granite	Granite/gabbro
Max. pressure	14 MPa	11 MPa	21 MPa	48 MPa
Max. flow rates	50 L/s	5 L/min	2 L/min	n/a
Volume	23'400 m^3	0.001 m^3 (= 29,7 L)	10^{-5} m^3 (= 100 ml)	n/a
Temporal shift between signal increase and start of injection	12 h	15 min	No shift	No shift
Signal increase during shut-in	Yes	Not conclusive	n/a	n/a
Slow signal decay after shut-in	Yes, several days	Yes, about 40 min	n/a	n/a
Amplitude ranges	A few mV	Hundreds of mV	Hundreds to thousands of mV	Hundreds to thousands of mV

Regarding the possible interpretation in terms of electrokinetic or seismoelectric effects, the hydro-mechanic coupling often masks a direct physical link of low resistivity to flow or induced seismicity/AE for both the reservoir and underground lab scale.

Generally, there are two observations concerning a temporal shift between the seismic/AE and hydraulic on the one hand and SP or EM fields on the other hand:

1. Depending on the scale, resistivity decreases are observed prior to seismic or acoustic events, i.e., several days to hours for large-scale earthquakes and about 24 h for reservoir scale. However, at the underground lab scale, such effects were not observed in the EMR measurements.

2. SP signal at the different sensor reveals a time delay that is related to the scale and thus the distance of the sensors. For example, at Soultz-sous-Forêts and Äspö HRL, the delays are about 12 h and about 15 min, respectively, while instantaneous changes in SP are observed at the lab scale.

The following experiments of parts of the experiments provide evidence on the relationship between pressure and SP or EM signals:

1. Rittershoffen: At Rittershoffen, no induced seismicity was observed during the MT monitoring. Furthermore, resistivity decrease was observed only during injection, not during production, and on the component parallel to Shmin. Therefore, a relation to the pressure applied to the fracture planes during injection is likely.

2. A relation between the EM signal and pressure is also indicated by the EMR measurements in the Äspö HRL, where relaxation of the EMR signal during and after shut-in inversely correlates with the pressure decrease.

3. Experiments on a dry rock under mechanical loading clearly demonstrated the significance of pressure for electric potential.

This thesis was undertaken to understand the interaction between hydraulic, mechanical, and electric, magnetic, and electromagnetic processes. It monitors and analyses SP and EM signals in different experimental settings in the context of possible precursors of earthquakes and induced seismicity. In conclusion, the objectives of this thesis have been achieved by

1. providing a new MT monitoring data set of fluid injection in a different rock type, i.e., basalt,

2. filling the scale-gap of SP and EM data sets by monitoring underground-lab scale injection tests, and

3. indicating precursor of seismic events under controllable condition.

A number of open questions remain, such as

1. Can the precursor observations be verified on in other experiments as well as on underground lab- or lab-scale?

2. Is the supposed link between pressure and EM or SP signal linked to fluid flow on micro-fractures or only to pressure?

Based on the findings of this thesis and the remaining questions, including if these observations can be verified under fully controlled conditions, a new experiment is developed at the lab scale. The so-called RockBlock experiment (RockBlockEx) aims to simulate the subsurface's natural pressure differences and is described in the chapter 8.

Chapter 8

RockBlockEx - A hydraulic fracturing experiment at laboratory scale

This chapter deals with the development of the laboratory experiment RockBlockEx.

8.1 Motivation

Induced seismicity and leakage are both related to fracture opening or propagation. Experiments at 10-1000 m-scale have revealed basic concepts to control induced seismicity and permeability enhancement during reservoir engineering (Schill et al. 2017; Zang et al. 2017). At cm-scale, related hydraulic fracturing experiments have been carried out for the first time at the University of Oklahoma (Hu et al. 2016). During the fracturing and circulating phases, the correlation between the pressure drop and the electric self-potential is shown (Hu et al. 2020). At the reservoir scale, changes in the SP are observed not only related to pressure drops but also in the shut-in phase (Marquis et al. 2002). Resistivity changes acquired during magnetotelluric monitoring were mainly related to fluid injection (Abdelfettah et al. 2018), but also occur contemporaneously to induced seismicity (Haaf and Schill 2021). Such signals are even observed before large earthquakes and may serve as precursor (Ohta et al. 2013). Although some theories were put forward, their seismo-electric origin is still debatable. RockBlockEx aims to investigate these effects under controlled laboratory conditions.

Due to its dimensions, RockBlockEx allows the generation and examination of a fracture as a complete system while maintaining the integrity of the fracture. The setting will also allow a 4-D localization of processes through a dense sensor distribution and further instrumentation experiments more specific to monitoring techniques. The setting will also allow a 4-D localization of processes through a dense sensor distribution.

8.2 Experimental setup

Figure 8.1 shows the stainless steel frame of the RockBlockEx experiment. It consists of six enclosing cover plates, a layer of pressure pads (flat jacks), compensation plates, and inner plates with the cutouts for the sensors. The

compensation plates and the inner plates have a thickness of 70 mm. The setup is suitable for a 500x500x500 mm^3 rock block in the middle. The first rock sample, granite from the black forest, has an edge length of 440 mm. Therefore the compensation plates of 30 mm at each of the six sites of the cube. Cutouts for the installed sensors and cable routing were milled into the compensation plates. At the corners, the measuring cables are led out of the installation via 35 mm wide holes. Five openings for injection and production holes were made in the top cover plate.

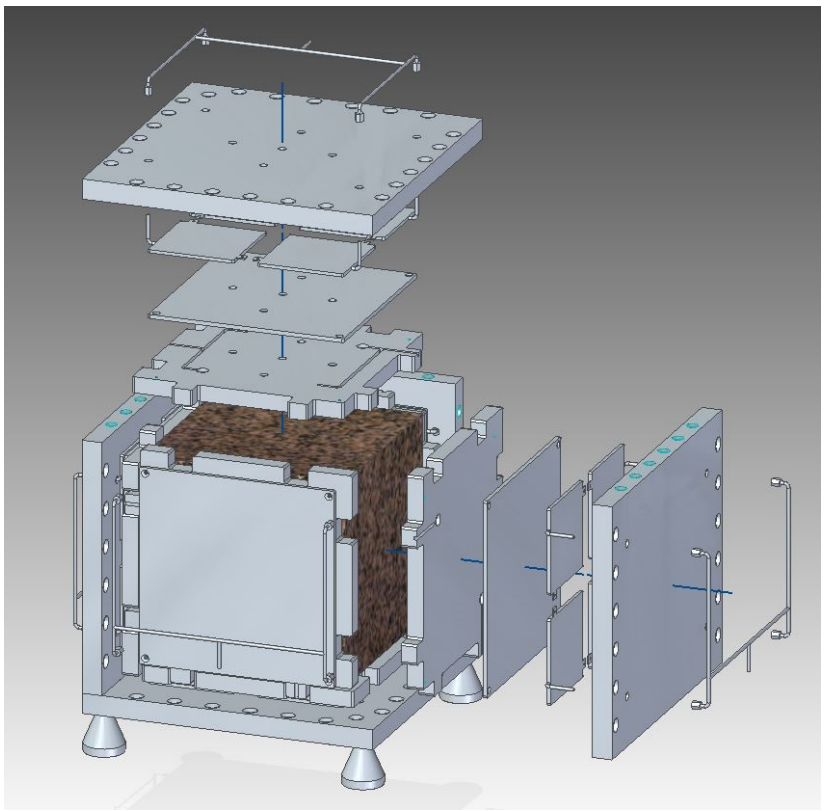

FIGURE 8.1: Design of the RockBlockEx with the different plates covering the rock in the inside.

Figure 8.2a shows the setup of the RockBlockEx, when the setup is closed. The flat jacks are installed at each site of the cube. This setup allows for simulating natural differential pressures in subsurface. Figure 8.2b shows the installed flat jacks exemplary at the front and the right side. The flat jacks are controlled by the external pumps control by Lewa Nikkiso Deutschland GmbH.

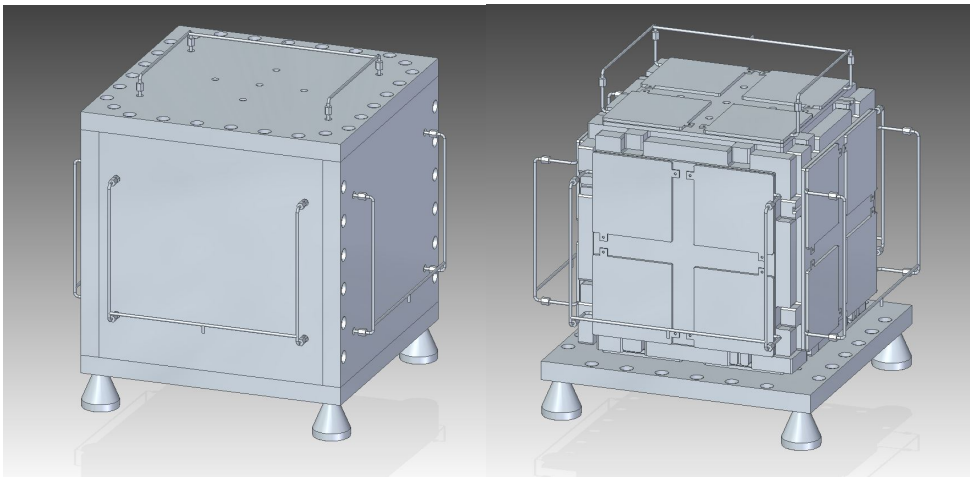

(A) (B)

FIGURE 8.2: (A) the enclosed RockBlockEx and (B) the installed flat jacks in pair of two in the upper and lower half of the RockBlockEx.

Figure 8.3 shows the dense sensor distribution that allows 4-D localization of the processes. The setup includes SP electrodes, EMR antennas, AE sensors, and temperature and pressure sensors in the production and injection wells at the surface. The injection well is connected to the injection pump. P/T sensors are placed in the holes. In addition, two sensors each for AE and EM emissions are installed on cube side 1. Additional AE sensors are placed on all cube sides to ensure total coverage of the experiment. Additional EM sensors are placed on cube side 2 so that all three spatial directions are covered. The electrodes for the SP measurements are installed on cube side 4. A syringe pump (Teledyne ISCO) is installed next to the experiment with flow rates up to 2ml/min. This pump can induce the physical processes by hydraulic injections.

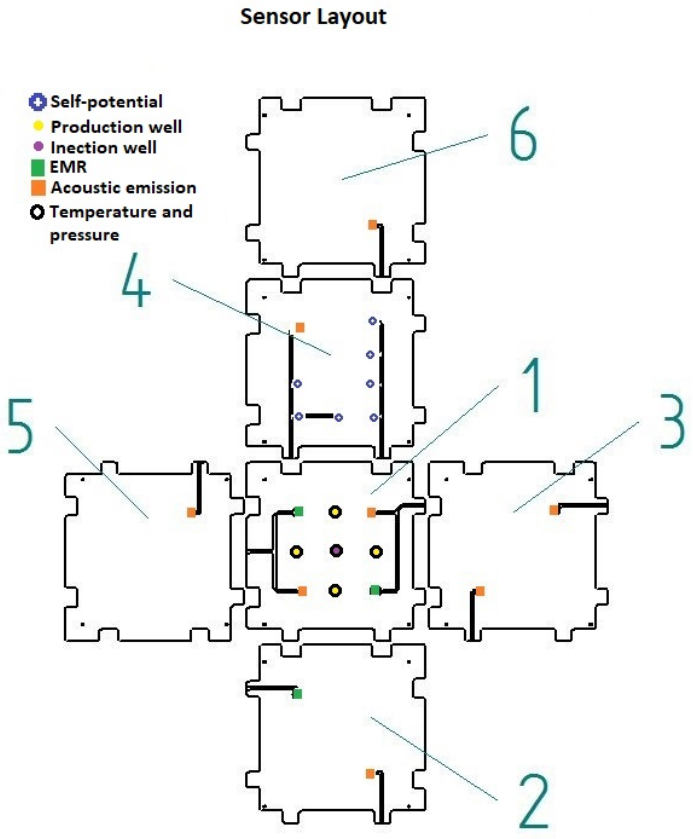

FIGURE 8.3: Sensor layout of the RockBlockEx with yellow and purple circles as production and injection wells, respectively. The temperature and pressure sensors are marked as black circles, the SP sensors as blue markers, AE in orange and EMR sensors in green.

8.3 Outlook on planned experiments

Due to its dimensions, RockBlockEx allows the generation and investigation of a fracture as a whole system under different conditions. The advantage of this setup is the inclusion of acoustic, electric, and electromagnetic sensors compared to other experiments such as (Hu et al. 2016). Another adjustment compared to the Äspö experiment is using a new EMR logger (Universal Self Recorder Geophysical Urga-16). This logger is more refined than the one used in the Äspö HRL: e.i. It covers a broader frequency range from 1-150 kHz and measures the EMR parameters (see section 3.2.4), as well as the raw EMR signals as time series. In addition, the EMR sensors will be installed in drilled holes directly in the rock sample to reduce background noise. Finally, isolating sheets with a thickness of 0.3 mm will be installed between the rock sample and the inner plates to achieve electric insulation.

Initially, preliminary tests will take place to test the entire setup for safety and possible leakage. For example, below the pumps, tubs are placed in case of leaking water or oil from handling the flat jacks pumps. Furthermore, measurements will take place to evaluate possible electric, electromagnetic, or acoustic noise sources for the SP and EMR loggers and the AE sensors.

After adjusting all necessary loggers and pumps, the first experiment will be the hydraulic fracturing test of a granite block. The rock sample was donated by KIMO GmbH, located in southern Germany.

The hydraulic fracturing is initiated by the syringe pump. The goal is to create a fracture in the center of the rock sample and keep it open. SP, AE, and EMR sensors monitor the process. All methods proved appropriate for monitoring crack initiation and propagation at the cm scale.

Circulation experiments can take place in the granite rock to use the created fracture. As introduced in section 2.4, certain electrothermal, electrokinetic, or electrochemical effects cause changes in the SP amplitudes. The effect on the SP amplitudes can be calculated and modeled with certain salinity or temperatures. The setup can handle without adjusting temperatures up to 80°C. The electrokinetic effect can be obtained by measuring the zeta potential directly at the injection and production wells, among other quantities. Parallel to these experiments, a physical model will be developed in COMSOL Multiphysics to examine these effects step by step with the RockBlockEx, starting from a 1D model.

The findings of the MT monitoring in Rittershoffen provide ideas for future RockBlockEx hydraulic fracturing experiments:

1. To test and examine if and when EM signals are measured during the injection or production experiments.

2. The 4D monitoring setup examines the possible propagation direction of the fracture and the AE, SP, and EMR signals during deformation.

3. The spatial mapping can give insights into the open research question of whether the supposed link between pressure and EM/SP signal is linked to the fluid flow on (micro-)fractures or only to pressure.

One of this setup's great advantages is the rock sample replacement. In further experiments, another rock type is planned to be used. Basaltic offers a broad range of usage. First, the test is to reproduce the Icelandic data set, and second to confirm or reject the idea of the different frequency ranges of EM signals. Moreover, to investigate the electric and electromagnetic signals and compares them to those obtained in granitic rocks.

The long-term goal is to establish injection experiments at the lab scale that can provide a scientific basement for the upcoming GeoLab project: a large-scale Helmholtz infrastructure for thermal - hydraulic - mechanical - chemical processes of deep geothermal reservoirs (www.geolab.kit.edu).

Bibliography

Abdelfettah, Y., P. Sailhac, H. Larnier, P.-D. Matthey, and E. Schill (2018). "Continuous and time-lapse magnetotelluric monitoring of low volume injection at Rittershoffen geothermal project, northern Alsace–France". In: *Geothermics* 71, pp. 1–11.

Allmann, M. Käser, and E. Rausch (2019). *Erdbeben - Eine tödliche Gefahr*. Munich RE. URL: https://www.munichre.com/de/risiken/naturkatastrophen-schaeden-nehmen-tendenziell-zu/erdbeben-eine-toedliche-gefahr.html.

Archie, Gustave E (1942). "The electrical resistivity log as an aid in determining some reservoir characteristics". In: *Transactions of the AIME* 146.01, pp. 54–62.

Arnason, Knutur, Ragna Karlsdottir, Hjalmar Eysteinsson, ÓG Flóvenz, and Steinar Thor Gudlaugsson (2000). "The resistivity structure of high-temperature geothermal systems in Iceland". In: *Proceedings of the World Geothermal Congress 2000, Kyushu-Tohoku, Japan*, pp. 923–928.

Bahat, D., A. Rabinovitch, and V. Frid (2005). *Tensile Fracturing in Rocks*. Springer-Verlag. DOI: 10.1007/b137741. URL: https://doi.org/10.1007/b137741.

Baujard, C., A. Genter, E. Dalmais, V. Maurer, R. Hehn, R. Rosillette, J. Vidal, and J. Schmittbuhl (2017). "Hydrothermal characterization of wells GRT-1 and GRT-2 in Rittershoffen, France: Implications on the understanding of natural flow systems in the rhine graben". In: *Geothermics* 65, pp. 255–268. ISSN: 03756505. DOI: 10.1016/j.geothermics.2016.11.001. URL: https://www.sciencedirect.com/science/article/pii/S0375650516301341.

Becken, M and H Burkhardt (2004). "An ellipticity criterion in magnetotelluric tensor analysis". In: *Geophysical Journal International* 159.1, pp. 69–82.

Best, M.E. (Jan. 2015). "Best, M.E., 2015. Electromagnetic (EM) Methods; in Shear Wave Velocity Measurement Guidelines for Canadian Seismic Site Characterization in Soil and Rock, (ed.) J.A. Hunter and H.L. Crow; Geological Survey of Canada, Earth Science Sector, General Information Product 110 e, p. 170-180." In: pp. 170–180.

Bischoff, J.L. and R.J. Rosenbauer (1988). "Liquid-vapor relations in the critical region of the system NaCl-H2O from 380 to 415 C: A refined determination of the critical point and two-phase boundary of seawater". In: *Geochimica et Cosmochimica Acta* 52.8, pp. 2121–2126.

Caldwell, T.G., H.M. Bibby, and C. Brown (Aug. 2004). "The magnetotelluric phase tensor". In: *Geophysical Journal International* 158.2, pp. 457–469. DOI: 10.1111/j.1365-246x.2004.02281.x. URL: https://doi.org/10.1111/j.1365-246x.2004.02281.x.

Charléty, J., N. Cuenot, L. Dorbath, C. Dorbath, H. Haessler, and M. Frogneux (2007). "Large earthquakes during hydraulic stimulations at the geothermal site of Soultz-sous-Forêts". In: *International Journal of Rock Mechanics and Mining Sciences* 44.8, pp. 1091–1105.

Chave and A.G. Jones (2012). *The Magnetotelluric Method: Theory and Practice*. Cambridge University Press. DOI: 10.1017/cbo9781139020138. URL: https://doi.org/10.1017/cbo9781139020138.

Chave and D.J. Thomson (Oct. 1989). "Some comments on magnetotelluric response function estimation". In: *Journal of Geophysical Research: Solid Earth* 94.B10, pp. 14215–14225. DOI: 10.1029/jb094ib10p14215. URL: https://doi.org/10.1029/jb094ib10p14215.

— (June 2004). "Bounded influence magnetotelluric response function estimation". In: *Geophysical Journal International* 157.3, pp. 988–1006. ISSN: 0956-540X. DOI: 10.1111/j.1365-246X.2004.02203.x. eprint: http://oup.prod.sis.lan/gji/article-pdf/157/3/988/6058362/157-3-988.pdf. URL: https://doi.org/10.1111/j.1365-246X.2004.02203.x.

Cicerone, R. D., J. E. Ebel, and J. Britton (2009). "A systematic compilation of earthquake precursors". In: *Tectonophysics* 476.3-4, pp. 371–396.

Clarke, J., T.D. Gamble, W.M. Goubau, R.H. Koch, and R.F. Miracky (1983). "Remote-reference magnetotellurics: equipment and procedures". In: *Geophysical Prospecting* 31.1, pp. 149–170.

Constable, S.C., A.S. Orange, G.M. Hoversten, and H.F. Morrison (1998). "Marine magnetotellurics for petroleum exploration Part I: A sea-floor equipment system". In: *Geophysics* 63.3, pp. 816–825.

D'Incecco, S., E. Petraki, G. Priniotakis, M. Papoutsidakis, P. Yannakopoulos, and D. Nikolopoulos (2021). "CO2 and Radon Emissions as Precursors of Seismic Activity". In: *Earth Systems and Environment*, pp. 1–12.

Darnet, M., A. Maineult, and G. Marquis (2004). "On the origins of self-potential (SP) anomalies induced by water injections into geothermal reservoirs". In: *Geophysical Research Letters* 31.19. DOI: 10.1029/2004gl020922. URL: https://doi.org/10.1029/2004gl020922.

Darnet, M., G. Marquis, and P. Sailhac (2006). "Hydraulic stimulation of geothermal reservoirs: fluid flow, electric potential and microseismicity relationships". In: *Geophysical Journal International* 166.1, pp. 438–444. ISSN: 0956-540X. DOI: 10.1111/j.1365-246X.2006.03026.x.

DEEPEGS Office Reykjavik, Iceland (2016). *DEEPEGS - Deployment of deep enhanced geothermal systems for sustainable energy business*. [Online; accessed 24-August-2021]. URL: https://deepegs.eu/.

Deichmann, Nicolas, Manfred Baer, Jochen Braunmiller, Stephan Husen, Donat Fäh, Domenico Giardini, Philipp Kästli, Urs Kradolfer, and Stefan Wiemer (2006). "Earthquakes in Switzerland and surrounding regions during 2005". In: *Eclogae Geologicae Helvetiae* 99.3, pp. 443–452.

Didana, Y.L., G. Heinson, S. Thiel, and L. Krieger (2017). "Magnetotelluric monitoring of permeability enhancement at enhanced geothermal system project". In:

Geothermics 66, pp. 23–38. ISSN: 03756505. DOI: 10.1016/j.geothermics.2016.11.005.

Didana, Y.L., S. Thiel, G. Heinson, and G. Boran (2016). "Magnetotelluric Monitoring of Hydraulic Fracture Stimulation at the Habanero Enhanced Geothermal System, Cooper Basin, South Australia". In: *ASEG Extended Abstracts* 2016.1, p. 1. ISSN: 2202-0586. DOI: 10.1071/ASEG2016ab123.

Driesner, T., S. Wiemer, R. Krause, and D. Giardini (2020). *FASTER: Forecasting and Assessing Seismicity and Thermal Evolution in geothermal Reservoirs*. URL: https://www.pasc-ch.org/projects/2017-2020/faster/ (visited on 2020).

Edwards, B., T. Kraft, C. Cauzzi, P. Kästli, and S. Wiemer (2015). "Seismic monitoring and analysis of deep geothermal projects in St Gallen and Basel, Switzerland". In: *Geophysical Journal International* 201.2, pp. 1022–1039.

Elders, W.A., G. Friðleifsson, and A. Albertsson (2014). "Drilling into magma and the implications of the Iceland Deep Drilling Project (IDDP) for high-temperature geothermal systems worldwide". In: *Geothermics* 49, pp. 111–118.

Elektronik GmbH, Metronix Meßgeräte und (2019). *Field manual*. https://www.metronix.de/metronixweb/en/geophysiks/start/. [Online; accessed 24-August-2019].

Fetter, C.W. (1993). "Contaminant Hydrogeology Macmillan Publishing Company, 458 pages". In: *New York*.

Flóvenz, Ó.G., L.S. Georgsson, and K. Árnason (1985). "Resistivity structure of the upper crust in Iceland". In: *Journal of Geophysical Research* 90.B12, p. 10136. ISSN: 0148-0227. DOI: 10.1029/JB090iB12p10136.

Flóvenz, Ó.G., E. Spangenberg, J. Kulenkampff, K. Árnason, R. Karlsdóttir, and E. Huenges (2005). "The role of electrical interface conduction in geothermal exploration". In: *Proceedings World Geothermal Congress*. Citeseer, pp. 24–29.

Freund, F. (2011). "Pre-earthquake signals: Underlying physical processes". In: *Journal of Asian Earth Sciences* 41.4-5, pp. 383–400. DOI: 10.1016/j.jseaes.2010.03.009. URL: https://doi.org/10.1016/j.jseaes.2010.03.009.

Frid, V. (1997a). "Electromagnetic radiation method for rock and gas outburst forecast". In: *Journal of Applied Geophysics* 38.2, pp. 97–104.

— (1997b). "Rockburst hazard forecast by electromagnetic radiation excited by rock fracture". In: *Rock Mechanics and Rock Engineering* 30.4, pp. 229–236.

— (2000). "Electromagnetic radiation method water-infusion control in rockburst-prone strata". In: *Journal of Applied Geophysics* 43.1, pp. 5–13.

— (2001). "Calculation of electromagnetic radiation criterion for rockburst hazard forecast in coal mines". In: *Pure and Applied Geophysics* 158.5-6, pp. 931–944.

Frid, V., A. Rabinovitch, and D. Bahat (June 2003). "Fracture induced electromagnetic radiation". In: *Journal of Physics D: Applied Physics* 36.13, pp. 1620–1628. DOI: 10.1088/0022-3727/36/13/330. URL: https://doi.org/10.1088/0022-3727/36/13/330.

Friðleifsson, W.A. Elders, R.A. Zierenberg, A.P.G. Fowler, T.B. Weisenberger, K.G. Mesfin, Ó. Sigurðsson, S. Nıelsson, G. Einarsson, F. Ó., E.Á. Guðnason, H. Tulinius, K. Hokstad, G. Benoit, F. Nono, D. Loggia, F. Parat, S.B. Cichy, D. Escobedo, and D. Mainprice (Feb. 2020). "The Iceland Deep Drilling Project at Reykjanes: Drilling into the root zone of a black smoker analog". In: *Journal of Volcanology and Geothermal Research* 391, p. 106435. DOI: 10.1016/j.jvolgeores.2018.08.013. URL: https://doi.org/10.1016/j.jvolgeores.2018.08.013.

Friðleifsson, W.A. Elders, R.A. Zierenberg, A. Stefánsson, A.P.G. Fowler, T.B. Weisenberger, B.S. Harðarson, and K.G. Mesfin (2017). "The Iceland Deep Drilling Project 4.5 km deep well, IDDP-2, in the seawater-recharged Reykjanes geothermal field in SW Iceland has successfully reached its supercritical target". In: *Scientific Drilling* 23, pp. 1–12.

Friðleifsson, GÓ., Ó. Sigurdsson, D. Þorbjörnsson, R. Karlsdóttir, Þ. Gıslason, A. Albertsson, and W.A. Elders (2014). "Preparation for drilling well IDDP-2 at Reykjanes". In: *Geothermics* 49, pp. 119–126.

Fridriksson, T., A. Stefánsson, F. Óskarsson, E. Eyjólfsdóttir, and Ó. Sigurdsson (2015). "Fluid chemistry scenarios anticipated for IDDP-2 to be drilled in Reykjanes, Iceland". In: *World Geothermal Congress*.

Frohlich, Cliff (2012). "Two-year survey comparing earthquake activity and injection-well locations in the Barnett Shale, Texas". In: *Proceedings of the National Academy of Sciences* 109.35, pp. 13934–13938.

Gamble, T.D., W.M. Goubau, and J. Clarke (1979). "Magnetotellurics with a remote magnetic reference". In: *Geophysics* 44.1, pp. 53–68.

Gershenzon, N.I., M.B Gokhberg, V.A. Morgunov, and V.N. Nikolaevskiy (1987). "Sources of electromagnetic emissions preceding seismic events". In: *Izvestiya Akademii Nauk SSSR, Physics of the Solid Earth* 23.2, p. 96.

Gharibi, M., R. A. Budiman, R. R. Stewart, and L. R. Bentley (2004). *The coupled seismoelectric wave propagation in porous media: Theoretical background*. CREWES Research Report. URL: https://www.researchgate.net/publication/239809395_The_coupled_seismoelectric_wave_propagation_in_porous_media_Theoretical_background.

Glen, S.; (July 2018). *StatisticsHowTo.com: Elementary Statistics for the rest of us*. URL: https://www.statisticshowto.com/gauss-markov-theorem-assumptions/.

Glover, P. (2015). *Geophysical properties of the near surface Earth: Electrical properties: Treatise on Geophysics, 11, 89–137*.

Gold, R.M., G.P. Markov, P.G. Mogila, and M.A. Samokhvalov (1975). "Impulse electromagnetic radiation of minerals and rocks, subjected to mechanical loading". In: *Izvestiya Akademii Nauk SSSR Fizika Zemlii* 7, pp. 109–111.

Golovin, Y. and A. Shibkov (1986a). "Dynamics of dislocation pile-ups and pulsed polarization of LiF single crystals in the case of single slip". In: *Sov. Phys. Sol-State* 28.9, pp. 1625–1626.

— (1986b). "Fast electrical processes and dynamics of dislocations in plastically deformed alkali halide crystals". In: *Soviet Physics—Solid State* 28, pp. 1964–1968.

Greiling, R.O. and H. Obermeyer (2010). "Natural electromagnetic radiation (EMR) and its application in structural geology and neotectonics". In: *Journal of the Geological Society of India* 75.1, pp. 278–288.

Grigoli, F., S. Cesca, A.P. Rinaldi, A. Manconi, J.A. Lopez-Comino, J.F. Clinton, R. Westaway, C. Cauzzi, T. Dahm, and S. Wiemer (2018). "The November 2017 Mw 5.5 Pohang earthquake: A possible case of induced seismicity in South Korea". In: *Science* 360.6392, pp. 1003–1006.

Guðnason, E.Á., K. Ágústsson, K. Gunnarsson, and Ó.G. Flóvenz (2015). "Seismic Activity on Reykjanes December 2014 – November 2015". In: *Iceland GeoSurvey* DEEPEGS.

— (2016). "Seismic Activity on Reykjanes December 2015 – November 2016". In: *Iceland GeoSurvey* DEEPEGS.

Haaf, N. and E. Schill (2019). "Processing of magnetotelluric data for monitoring changes in electric resistivity during drilling operation". In: *PROCEEDINGS, 44th Workshop on Geothermal Reservoir Engineering* 44.

— (2021). ""Noise" during long-term continuous magnetotelluric monitoring of RN-15/IDDP-2 well engineering (Reykjanes peninsular, Iceland): A geogenic origin?" In: *Geothermics* 96, p. 102192.

Häring, Markus O, Ulrich Schanz, Florentin Ladner, and Ben C Dyer (2008). "Characterisation of the Basel 1 enhanced geothermal system". In: *Geothermics* 37.5, pp. 469–495.

Hersir, G.P. and K. Árnason (2010). *Resistivity of rocks: Presented at Short Course V on Exploration for Geothermal Resources,*

Hirose, F., K. Miyaoka, N. Hayashimoto, T. Yamazaki, and M. Nakamura (2011). "Outline of the 2011 off the Pacific coast of Tohoku Earthquake (M w 9.0)—Seismicity: foreshocks, mainshock, aftershocks, and induced activity—". In: *Earth, planets and space* 63.7, pp. 513–518.

Hoaglin, D.C. and R.E. Welsch (Feb. 1978). "The Hat Matrix in Regression and ANOVA". In: *The American Statistician* 32.1, p. 17. DOI: 10.2307/2683469. URL: https://doi.org/10.2307/2683469.

Hokstad, K. and K. Tanavasuu-Milkeviciene (2017). "Temperature prediction by multi-geophysical inversion: application to the IDDP-2 well at Reykjanes, Iceland". In: *Geotherm Resource Council* 41, pp. 1141–52.

Holleman, Arnold F., Egon Wiberg, and Nils Wiberg (2007). *Lehrbuch der anorganischen Chemie* -. Berlin: Walter de Gruyter. ISBN: 978-3-110-17770-1.

Hu, L. and A. Ghassemi (2020). "Heat production from lab-scale enhanced geothermal systems in granite and gabbro". In: *International Journal of Rock Mechanics and Mining Sciences* 126, p. 104205. ISSN: 13651609. DOI: 10.1016/j.ijrmms.2019.104205.

Hu, L., A. Ghassemi, J. Pritchett, and S. Garg (2016). "Laboratory Scale Investigation of Enhanced Geothermal Reservoir Stimulation". In:

Hu, L., A. Ghassemi, J. Pritchett, S. Garg, and T. Ishido (2020). "Self-Potential Response in Laboratory Scale EGS Stimulation". In: *Rock Mechanics and Rock Engineering* 53.2, pp. 691–703. ISSN: 0723-2632. DOI: 10.1007/s00603-019-01937-y.

Hubbert, M K. and W. W. Rubey (1959). "Mechanics of fluid-filled porous solids and its application to overthrust faulting". In: *Geological Society of America Bulletin* 70, pp. 115–166.

Hydraulic Data RN-15/IDDP-2 (2017). *DEEPEGS*.

Ishido, T. and J.W. Pritchett (2000). "Using numerical simulation of electrokinetic potentials in geothermal reservoir management". In: *Proc. World Geothermal Congress 2000*, pp. 2629–2634.

Jónsson, S.S., M.Á. Sigurgeirsson, Ó. Sigurðsson, and H. Ingólfsson (2010). "Reykjanes–Hola RN-15, 3. áfangi: Borun Vinnsluhluta frá 804 m ı 2507 m Dpi". In: *Iceland GeoSurvey, ÍSOR-2010/050*.

Junge, A. (1996). "Characterization of and correction for cultural noise". In: *Surveys in Geophysics* 17.4, pp. 361–391.

Kagan, Y. and L. Knopoff (1976). "Statistical search for non-random features of the seismicity of strong earthquakes". In: *Physics of the earth and planetary interiors* 12.4, pp. 291–318.

— (1977). "Earthquake risk prediction as a stochastic process". In: *Physics of the Earth and Planetary Interiors* 14.2, pp. 97–108.

Karlsdóttir, R. and A. Már Vilhjálmsson (2016). "Reykjanes – Sandvík 3D Inversion of MT Data". In: *Iceland GeoSurvey ÍSOR* ÍSOR-2015/041.

Kärnbränslehantering, Svensk (2016). *Äspö Hard Rock LaboratoryAnnual Report 2016*. Tech. rep. TR-17-10. Box 5864, SE-102 40 Stockholm Sweden: Swedish Nuclear Fueland Waste Management Co - SVENSK KÄRNBRÄNSLEHANTERING AB.

Keller, G.V. and F.C. Frischknecht (1966). *Electrical Methods in Geophysical Prospecting*. Oxford, Pergamon Press.

Khatiashvili, N. (1984). "The electromagnetic effect accompanying the fracturing of alkaline halide crystals and rocks". In: *Physics of the Solid Earth* 20.9, pp. 656–661.

Khodayar, M., S. Níelsson, C. Hickson, E.Á. Guðnason, B.S. Harðarson, V. Guðmundsdóttir, S. Halldórsdóttir, F. Óskarsson, T.B. Weisenberger, and S. Björnsson (2017). "The 2016 Conceptual Model of Reykjanes Geothermal System, SW Iceland". In: *Iceland GeoSurvey ÍSOR* DEEPEGS.

Kim, K.-H., J.-H. Ree, Y.H. Kim, S. Kim, S.Y. Kang, and W. Seo (2018). "Assessing whether the 2017 Mw 5.4 Pohang earthquake in South Korea was an induced event". In: *Science* 360.6392, pp. 1007–1009.

Klebanov, L.B., S.T. Rachev, and F.J. Fabozzi (2009). *Robust and non-robust models in statistics*. Nova Science Publishers New York.

Lichtenberger, Marco (2006). *Infoblatt zur Bestimmung von Spannungen um Tunnelbauwerke durch das Messen rissinduzierter elektromagnetischer Strahlung*. Gesellschaft für Erkundung und Ortung. Südbeckenstr. 14-20 a, 76189 Karlsruhe.

Maineult, Alexis, Yves Bernabé, and Philippe Ackerer (2005). "Detection of advected concentration and pH fronts from self-potential measurements". In: *Journal of Geophysical Research: Solid Earth* 110.B11.

Marquis, G., M. Darnet, P. Sailhac, A.K. Singh, and A. Gérard (2002). "Surface electric variations induced by deep hydraulic stimulation: An example from the Soultz HDR site". In: *Geophysical Research Letters* 29.14, pp. 7–1.

Martti Latva and Christian J. Engelsen, Tuija Kaunisto and and Sten Kloppenborg and Olivier Rod and Sverre Gulbrandsen-Dahl (2017). *Nordic drinking water quality - A Nordic Innovation project*. Report 1. Nordic Innovation project MaiD.

Mattsson, Hans Thunehed, Mikael Keisu, and GeoVista AB (2005). *Oskarshamn site investigationInterpretation of geophysical borehole measurements and compilation of petrophysical data from KLX01, KLX03, KLX04, HLX21, HLX22, HLX23, HLX24, HLX25, HLX26, HLX27 and HLX28*. Tech. rep. P-05-34. Box 5864, SE-102 40 Stockholm Sweden: Swedish Nuclear Fueland Waste Management Co.

Mazurek, Martin, Andreas Jakob, and Paul Bossart (2003). "Solute transport in crystalline rocks at Äspö—I: Geological basis and model calibration". In: *Journal of Contaminant Hydrology* 61.1-4, pp. 157–174.

Morgunov, V.A. (1985). "Electromagnetic emission during seismic activity". In: *Izvestia Akademii Nauk, Fizika Zemli* 3, p. 77.

Neyman, J. (1961). *Contemporary problems of mathematical statistics*. International Mathematical Congress in Amsterdam, Moscow, pp. 229–258.

Niemz, P., S. Cesca, S. Heimann, F. Grigoli, S. von Specht, C. Hammer, A. Zang, and T. Dahm (2020). "Full-waveform-based characterization of acoustic emission activity in a mine-scale experiment: a comparison of conventional and advanced hydraulic fracturing schemes". In: *Geophysical Journal International* 222.1, pp. 189–206. ISSN: 0956-540X. DOI: 10.1093/gji/ggaa127.

Niemz, P., T. Dahm, C. Milkereit, S. Cesca, G. Petersen, and A. Zang (2021). "Insights Into Hydraulic Fracture Growth Gained From a Joint Analysis of Seismometer-Derived Tilt Signals and Acoustic Emissions". In: *Journal of Geophysical Research: Solid Earth* 126.12, e2021JB023057. DOI: https://doi.org/10.1029/2021JB023057.

Ohta, K., J. Izutsu, A. Schekotov, and M. Hayakawa (2013). "The ULF/ELF electromagnetic radiation before the 11 March 2011 Japanese earthquake". In: *Radio Science* 48.5, pp. 589–596. ISSN: 00486604. DOI: 10.1002/rds.20064.

Peacock, J.R., S. Thiel, G.S. Heinson, and P. Reid (2013). "Time-lapse magnetotelluric monitoring of an enhanced geothermal system". In: *Geophysics* 78.3, B121–B130.

Peacock, J.R., S. Thiel, P. Reid, and G. Heinson (2012). "Magnetotelluric monitoring of a fluid injection: Example from an enhanced geothermal system". In: *Geophysical Research Letters* 39.18.

Petraki, E., D. Nikolopoulos, C. Nomicos, J. Stonham, D. Cantzos, P. Yannakopoulos, and S. Kottou (2015). "Electromagnetic pre-earthquake precursors: Mechanisms, data and models-A review". In: *Journal of Earth Science & Climatic Change* 6.1, p. 1.

Petrenko, V.F. (1993). "On the nature of electrical polarization of materials caused by cracks. Application to ice electromagnetic emission". In: *Philosophical Magazine B* 67.3, pp. 301–315.

Pritchett, J.W. and T. Ishido (2005). "Hydrofracture characterization using downhole electrical monitoring". In: *Proceedings of World Geothermal Congress, Turkey*.

Quist, A.S. and W.L. Marshall (1968). "Electrical conductances of aqueous sodium chloride solutions from 0 to 800. degree. and at pressures to 4000 bars". In: *The journal of physical chemistry* 72.2, pp. 684–703.

Rabinovitch, A., D. Bahat, and V. Frid (1995). "Comparison of electromagnetic radiation and acoustic emission in granite fracturing". In: *International journal of Fracture* 71.2, R33–R41.

— (2002). "Similarity and dissimilarity of electromagnetic radiation from carbonate rocks under compression, drilling and blasting". In: *International Journal of Rock Mechanics and Mining Sciences* 39.1, pp. 125–129.

Rabinovitch, A., G. Belizovsky, and D. Bahat (2000). "Origin of mist and hackle patterns in brittle fracture". In: *Physical Review B* 61.22, p. 14968.

Rabinovitch, A., V. Frid, J. Goldbaum, and D. Bahat (2003). "Polarization-depolarization process in glass during percussion drilling". In: *Philosophical Magazine* 83.25, pp. 2929–2940.

Rabinovitch, V. Frid, D. Bahat, and J. Goldbaum (2000). "Fracture area calculation from electromagnetic radiation and its use in chalk failure analysis". In: *International Journal of Rock Mechanics and Mining Sciences* 37.7, pp. 1149–1154.

Revil, A. and N. Florsch (Mar. 2010). "Determination of permeability from spectral induced polarization in granular media". In: *Geophysical Journal International*. DOI: 10.1111/j.1365-246x.2010.04573.x. URL: https://doi.org/10.1111/j.1365-246x.2010.04573.x.

Revil, A. and A. Jardani (2013). *The self-potential method: Theory and applications in environmental geosciences*. Cambridge: Cambridge University Press. ISBN: 9781107019270.

Ritter, Oliver, Gerard Muñoz, Ute Weckmann, Reinhard Klose, Stefan Rettig, Manfred Schüler, Carsten Müller-Brettschneider, Gregor Willkommen, and Paula Rulff (2015). *Permanent Magnetotelluric Reference Station Wittstock, Germany*. en. DOI: 10.5880/GFZ.2.2.2015.001. URL: https://dataservices.gfz-potsdam.de/panmetaworks/showshort.php?id=escidoc:697890.

Schill, E., A. Genter, N. Cuenot, and T. Kohl (2017). "Hydraulic performance history at the Soultz EGS reservoirs from stimulation and long-term circulation tests". In: *Geothermics* 70, pp. 110–124. ISSN: 03756505. DOI: 10.1016/j.geothermics.2017.06.003.

Schindler, M., J. Baumgärtner, T. Gandy, P. Hauffe, T. Hettkamp, H. Menzel, P. Penzkofer, D. Teza, T. Tischner, and G Wahl (2010). "Successful hydraulic stimulation techniques for electric power production in the Upper Rhine Graben, Central Europe". In: *World geothermal congress*. Vol. 2529.

Schoenball, M., L. Dorbath, E. Gaucher, J.F. Wellmann, and T. Kohl (2014). "Change of stress regime during geothermal reservoir stimulation". In: *Geophysical Research Letters* 41.4, pp. 1163–1170.

Simpson, F. and K. Bahr (Feb. 2005). "Practical Magnetotellurics". In: DOI: 10.1017/CBO9780511614095.

Smith, Bill, Joseph Beall, and Mitchel Stark (2000). "Induced seismicity in the SE Geysers field, California, USA". In: *Proceedings, World Geothermal Congress 2000*, pp. 2887–2892.

Suriyaarachchi, N. (Jan. 2012). "Joint 1D Inversion of MT and TEM resistivity data from the Theistareykir high-temperature geothermal area, NE-Iceland and comparison with alteration and temperature logs from boreholes". In:

Szarka, L. (1988). "Geophysical aspects of man-made electromagnetic noise in the earth—A review". In: *Surveys in Geophysics* 9.3-4, pp. 287–318.

Telford, William Murray, WM Telford, LP Geldart, and Robert E Sheriff (1990). *Applied geophysics*. Cambridge university press.

Urusovskaya, A.A. (1969). "Electric effects associated with plastic deformation of ionic crystals". In: *Soviet Physics Uspekhi* 11.5, pp. 631–643.

Wagner, W. and A. Pruß (2002). "The IAPWS formulation 1995 for the thermodynamic properties of ordinary water substance for general and scientific use". In: *Journal of physical and chemical reference data* 31.2, pp. 387–535.

Ward, S.H. and G.W Hohmann (1988). "Electromagnetic theory for geophysical applications". In: *Electromagnetic Methods in Applied Geophysics: Volume 1, Theory*. Society of Exploration Geophysicists, pp. 130–311.

Wei, M., D. Song, X. He, Z. Li, L. Qiu, and Q. Lou (2020). "Effect of Rock Properties on Electromagnetic Radiation Characteristics Generated by Rock Fracture During Uniaxial Compression". In: *Rock Mechanics and Rock Engineering* 53.11, pp. 5223–5238. ISSN: 0723-2632. DOI: 10.1007/s00603-020-02216-x. URL: https://link.springer.com/article/10.1007/s00603-020-02216-x.

Weidelt, P. (1972). "The inverse problem of geomagnetic induction". In: *J. Geophys.* 38, pp. 257–289.

Weisenberger, B.S. Harðarson, F. Kaestner, S.H Gunnarsdóttir, H. Tulinius, V. Guðmundsdóttir, G.M. Einarsson, F. Pétursson, S. Vilhjálmsson, H.Ö. Stefánsson, and S. Níelsson (2017). *Drilling in Reykjanes – Phases 4 and 5 from 3000 to 4659 m*. DEEPEGS Well Report – RN-15/IDDP-2. Iceland GeoSurvey.

Weisenberger, T.B., F. Kästner, S. Níelsson, B.S. Harðarson, B. Kristinsson, H. Ingólfsson, H.Ö. Stefánsson, H. Jónasson, and S. Vilhjálmsson (2017). *Drilling of Well RN-15/IDDP-2 in Reykjanes – Continuation of Phase 3 from 2509 m down to 3000 m*. DEEPEGS Well Report – RN-15/IDDP-2. Iceland GeoSurvey.

Welch, P. (1967). "The use of fast Fourier transform for the estimation of power spectra: a method based on time averaging over short, modified periodograms". In: *IEEE Transactions on audio and electroacoustics* 15.2, pp. 70–73.

Widestrand, Henrik, Johan Byegård, Eva Selnert, Susanne Höglund Mats Skålberg, Erik Gustafsson, and Geosigma AB (2010). *Long term sorption diffusion experiment (LTDE-SD) - Supporting laboratory program - Sorption diffusion experiments and rock material characterization*. Tech. rep. R-10-66. Box 5864, SE-102 40 Stockholm Sweden: Swedish Nuclear Fueland Waste Management Co.

Zang, A., O. Stephansson, L. Stenberg, K. Plenkers, S. Specht, C. Milkereit, E. Schill, G. Kwiatek, J. Dresen, G. Zimmermann, T. Dahm, and M. Weber (2017). "Hydraulic fracture monitoring in hard rock at 410 m depth with an advanced fluid-injection protocol and extensive sensor array". In: *Geophysical Journal International* 208.2, pp. 790–813. DOI: 10.1093/gji/ggw430. URL: https://doi.org/10.1093/gji/ggw430.

Zang, A., G. Zimmermann, H. Hofmann, O. Stephansson, K.-B. Min, and K.Y. Kim (2019). "How to reduce fluid-injection-induced seismicity". In: *Rock Mechanics and Rock Engineering* 52.2, pp. 475–493.

Zimmermann, G., A. Zang, O. Stephansson, G. Klee, and H. Semiková (2019). "Permeability Enhancement and Fracture Development of Hydraulic In Situ Experiments in the Äspö Hard Rock Laboratory, Sweden". In: *Rock Mechanics and Rock Engineering* 52.2, pp. 495–515.

Appendix A

Well design of RN-15/IDDP-2

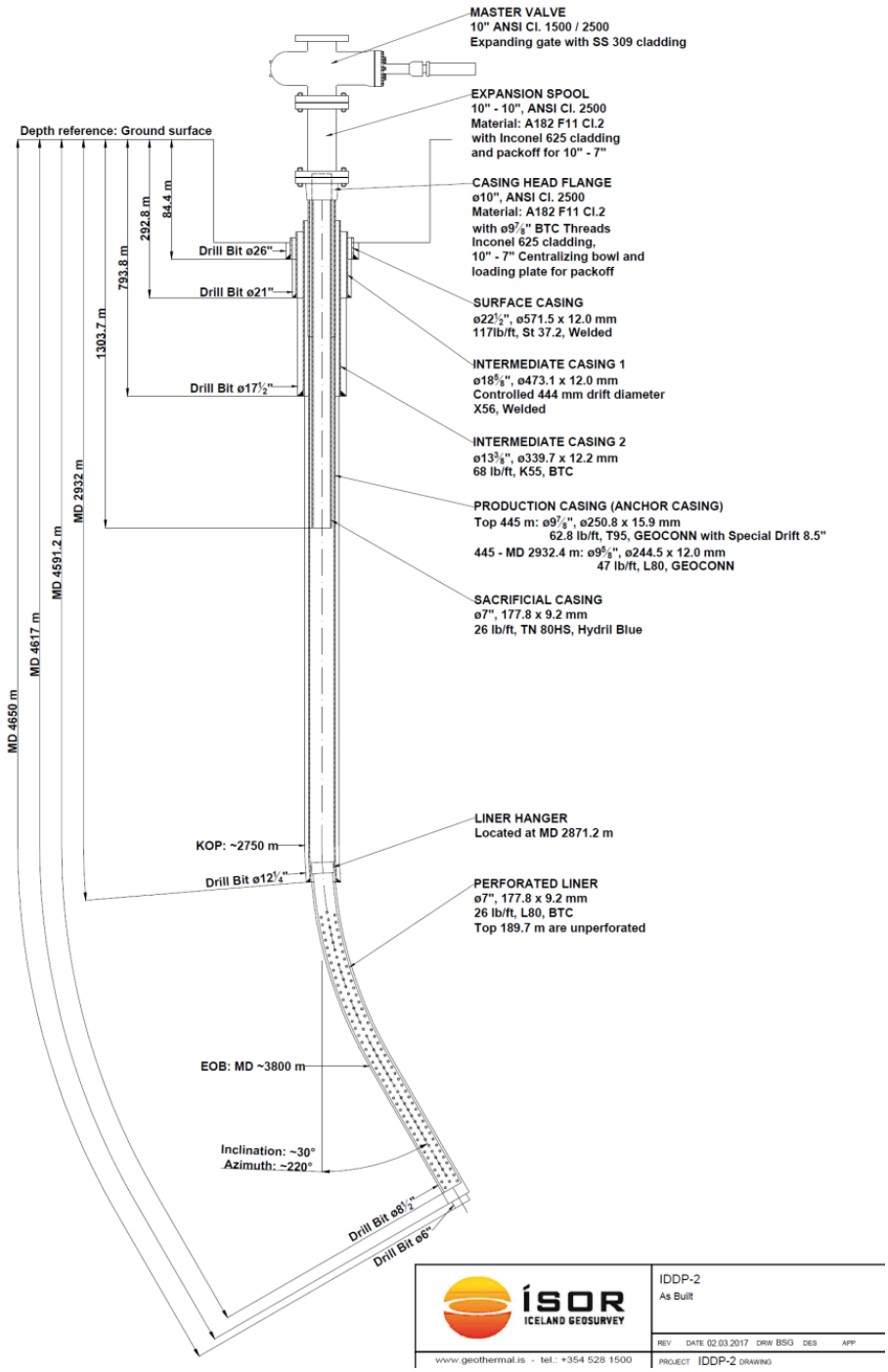

FIGURE A.1: Schematic sketch of the well design of RN-15/IDDP-2 (T. Weisenberger et al. 2017).

Appendix B

Data processing

This is additional information about the data processing of MT data. The robust processing scheme is shortly introduced in the chapter 4. The following sections are based on the theoretical background of the used processing code birrp by Chave and Thomson (2004).

B.1 M-estimator

In MT data the M-estimator is a robust approach which is not sensitive to a certain amount of bad data. M-estimator is a procedure to minimize a norm of random errors but in contrast to LS the misfit is selected that a few extreme values cannot dominate the answer (Chave and Thomson 1989). The M-estimate is obtained by minimizing $\mathbf{R}^H\mathbf{R}$ with $\mathbf{R}$ as a N-vector with $\sqrt{\rho(r_i/d)}$ as ith entry. d is a scale for residuals. The loss function $æ(x)$ is a distance measure between true and estimated values of a statistical parameter (Klebanov et al. 2009, as cited in Neyman 1961).
The M-estimator is a data-adaptive procedure since weights are chosen to minimize the influence of data corresponding to large residuals. Hence, the weighted LS solution is given by

$$\tilde{\mathbf{Z}} = \langle \mathbf{b}^* \mathbf{W} \mathbf{b} \rangle^{-1} \langle \mathbf{b}^* \mathbf{W} \mathbf{E} \rangle \tag{B.1}$$

with weighted auto- and cross-spectra in the parentheses equivalent to 4.6. An example for a widely used weight function in MT processing is the *Huber* function which theoretically guarantees convergence and has a high efficiency (Junge 1996):

$$\begin{aligned} w(x) &= 1 \qquad |x_i| \leq a \\ w(x) &= \frac{a}{|x_i|} \qquad |x_i| > a \end{aligned} \tag{B.2}$$

When $a = 1.5$ (Chave and Thomson 1989) then a 95% efficiency with outlier-free Gaussian data is given. The start of down-weighting of the data is given when $|x_i| = |r_i/d| = a$, hence the scale parameter d determines which of the residuals are considered as large (Chave and Thomson 2004). This step is necessary to make the weighted LS scale-invariant or the multiplication of data by a constant will not produce comparable changes in the solution.
A scale parameter is selected as the ratio of the sample and theoretical values of some statistics based on a target distribution. An example of a robust scale

statistic is given with a sample value

$$S_{MAD} = |r - \tilde{r}|_{\frac{N+1}{2}} \tag{B.3}$$

As a median absolute deviation from the median (MAD) with the subscript i, denoting the *i*th order statistic obtained by sorting the N values sequentially and $\tilde{r}$ as a median of **r**. The theoretical MAD is solution σ_{MAD} of

$$F(\tilde{\mu} + \sigma_{MAD}) - F(\tilde{\mu} - \sigma_{MAD}) = \frac{1}{2} \tag{B.4}$$

$\tilde{\mu}$ is the theoretical median, and F is the target cumulative distribution function. In MT processing, Fourier transform is the data and thus complex, but complex Gaussian may not be the best choice. Chave and Thomson (1989) suggested that Rayleigh is the best choice for an appropriate distribution for the magnitude of a complex number.
To summarize, at each frequency, an initial least squares solution is obtained from 4.6 and used to compute the residuals **r** in 4.3. The scale d is calculated from the ratio of B.3 and B.4 using the Rayleigh model for the residual distribution. An iterative procedure is then applied using B.1 with the Huber weights B.2, where the residuals from the previous iteration are used to get the scale and weights. It stops only when the weighted residual power $r^H vr$ doesn't change below a certain threshold value anymore. The Huber weights fall off slowly but never get zero. Thus they are not suitable for severe outliers. The scale is then fixed at the final Huber weight value, and several iterations are performed using the more severe weight given by

$$V_{ii} = \exp(e^{-\xi^2}) \exp(-e^{\xi(|x_i|-\xi)}) \tag{B.5}$$

again terminating when the weighted residual power does not change appreciably.

B.2 Hat matrix and leverage points

In some case scenarios robust processing is not enough to only limit the influence of outliers, e.g. during auroral substorm source fields or Pc3 geomagnetic pulsations extreme magnetic field data are produced which may be missed by robust estimators due to small residuals. Thus, Chave and Thomson (2004) introduced a bounded influence estimator to limit influence of both outliers and leverage points. As described in section B.1 the bounded influence estimator combines a standard robust M-estimator with leverage weighting based on statistics of the hat matrix diagonal. The hat matrix is a standard statistical measure for unusual predictors (Chave and Thomson 2004). The hat matrix gives each predicted value $\tilde{\mathbf{e}}$ as linear combination of the observed values **e** (Hoaglin and Welsch 1978):

$$\tilde{\mathbf{e}} = \mathbf{He} \tag{B.6}$$

with the hat matrix **H** defined as

$$\mathbf{H} = \mathbf{b}(\mathbf{b}^H\mathbf{b})^{-1}\mathbf{b}^H \tag{B.7}$$

a NxN matrix. An important property of projection matrices are that they are Hermitian and idempotent, $\mathbf{H}^2 = \mathbf{H}$. Thus it follows for the diagonal elements of **H** $0 < h_{ii} < 1$. In addition, the eigenvalues of projection matrices are 0 or 1 and the amount of non-zero eigenvalues is equal to the rank of the matrix, such as rank(**H**) = rank(**b**) = p, and hence the trace(rank(**H**)) = p with p columns in **b** (Hoaglin and Welsch 1978). and $h_{ii} = p/N$. If $h_{ii} = 1$ then model fits the data exactly and the other extreme case takes place when $h_{ii} = 0$ then the predicted value is fixed at zero by design and not affected by **e**. To summarize the hat matrix properties and its diagonal elements are a measure of amount of leverage exerted by a predictor datum.
The hat matrix and its properties can be easily generalized to the robust algorithm like in equation B.1 using its definition of B.7:

$$\mathbf{H} = \mathbf{b}(\mathbf{b}_R^H\mathbf{w}\mathbf{b})^{-1}\mathbf{b}_R^H\mathbf{w} \tag{B.8}$$

with w as diagonal matrix of robust weights with entries w_{ii}

B.3 Remote reference

Following the approaches of Gamble et al. (1979) and Clarke et al. (1983) uncorrelated noise can be eliminated from the measured data using remote referencing, when a high degree of correlation between the naturally induced electromagnetic fields at local and remote site is reached. Thus, the remote reference must be sufficiently distant to the local station, i.e. a few skin depths (Chave and Jones 2012), to ensure possible bias errors due to correlated noises to be small compared to the random errors (Chave and Jones 2012; Gamble et al. 1979). The remote reference solution after Gamble et al. (1979) is given by:

$$\tilde{\mathbf{Z}}^r = (\mathbf{b_r}^H\mathbf{b})^{-1}(\mathbf{b_r}^H\mathbf{e}) \tag{B.9}$$

with the remote reference magnetic field $\mathbf{b}_r$. The remote reference solution analogous to the weighted least squares problem in B.1 may be written as:

$$\tilde{\mathbf{Z}}^r = (\mathbf{b_r}^H\mathbf{v}\mathbf{b})^{-1}(\mathbf{b_r}^H\mathbf{v}\mathbf{e}) \tag{B.10}$$

The weights **v** are computed as in B.1 based on the residuals from 4.3.

Appendix C

Computation of the electrochemical potential

The computation of the electrochemical potentials was introduced in the chapter 2.4.3 with the equation 2.37. The following assumptions were made to compute the electrochemical potential during the HF experiments in Äspö HRL following the study of Darnet et al. (2004) and Maineult et al. (2005):

The units and values of the physical quantities are collected in the Table C.1.

Assuming a radial flow during injection in a homogeneous porous medium, the mass transport can be written as

$$D_L \frac{\partial^2 C}{\partial r^2} + \left(\frac{D_L}{r} - v_r \right) \frac{\partial C}{\partial r} = \frac{\partial C}{\partial t} \tag{C.1}$$

where D_L is the hydrodynamic longitudinal dispersion coefficient, v_r is the average linear fluid velocity, r is the radial distance from the well, and t is time.

The dispersion coefficient D_L is defined as

$$D_L = \alpha_L v_r + D^* \tag{C.2}$$

with D^* as molecular diffusion coefficient and α_L as the longitudinal dispersivity.

The mass conversation equation of the injected water is used to estimate the average linear fluid velocity

$$Qt = \pi r_0^2 h \phi_P \tag{C.3}$$

with Q as the injection rate, r_0 as the average frontal position of the injected water and h as the open hole section.

Here, the fracture planes are estimated based on the hypocenter location of the AEs of each (re)fracturing stage (Niemz et al. 2020). In particular, assuming that the fluid flows through the fractures, consider the largest fracture plane (HF2 RF5) with an ellipsoidal distribution and a radius of about 5 m. Thus, the maximum value of r_0 is 5 m. The smallest value of r_0 is assumed to be the length of the test interval, 0.5 m.

In addition, it is assumed that the fluid velocity is equal to the velocity of the front of injected water v_0 and it follows

$$v_r \approx v_0 = \frac{dr_0}{dt} = \frac{Q}{2\pi\phi_P}\left(\frac{Qt}{\pi h\phi_P}\right)^{-1/2}. \tag{C.4}$$

With a value of $\alpha_L v_r = 4.7735 \cdot 10^{-4} >> D^* = 5.10^{-10}$, the molecular diffusion is negligible.

Figure C.1 shows the calculated amplitudes of the electrochemical potentials using the equation 2.37. The amplitude ranges are for both extreme cases of r_0 extremely small with values between 0.02 -0.034 mV. Therefore, the electrochemical potential can be neglected when the SP amplitudes vary in ranges of hundreds of mV.

TABLE C.1: Summary of the values used in the computation of the electrochemical potentials (Fetter 1993; Holleman et al. 2007; Martti Latva and Christian J. Engelsen and Olivier Rod and Sverre Gulbrandsen-Dahl 2017; Mattsson et al. 2005; Mazurek et al. 2003; Niemz et al. 2020; Widestrand et al. 2010).

Quantity	**Value**	**Unit**	**note/ reference**
Molar gas constant R	8.3144598000000	J $mol^{-1}K^{-1}$	Holleman (2007)
Unit charge e	1.602176634x10^{-19}	C	Holleman (2007)
Avogadro's number N	6.02214076x10^{23}	mol^{-1}	Holleman (2007)
Ionic mobility u_{Na}	5.2x10^{-8}	$m^2\ s^{-1}\ V^{-1}$	Holleman (2007)
Ionic mobility u_{Cl}	7.9x10^{-8}	$m^2\ s^{-1}\ V^{-1}$	Holleman (2007)
Initial concentration C_0	2.2649x10^{-06}	mol L^{-1}	226 ppm Swedish tap water, Kaunisto et al. (2017)
Temperature	291.15	K	
Longitudinal dispersivity α_L	0.45	m	Value for crystalline rock by Mazruek et al. (2003)
Hydrodynamic longitudinal dispersion coefficient D_L	4.7735x10^{-04}	$m^2\ s^{-1}$	Equation C.2
Fluid velocity v_r	0.001060776627006	m s^{-1}	Equation C.4
Flow-rate Q	5,0×10-5	$m^3\ s^{-1}$	Average flow-rate of HF2 and HF3
Molecular diffusion coefficient D*	5.10^{-10}	$m^2\ s^{-1}$	Fetter (1993)
Time in s	272	s	Average injection time of HF2 and HF3
Porosity ϕ_P	0.26	%	Widestrand et al. (2010)
Open hole section h	5.0	m	Estimated radius of largest elliptical fracture plane of AE activity in HF2 and HF3 (Niemz et al., 2020).
Average frontal position of the injected water r_0	0.5-5.0	m	Minimal (test interval) and maximal radius (see h) were tested.
Concentration C_1	1.71*10^-5	mol L^{-1}	Mattsson et al. (2005)

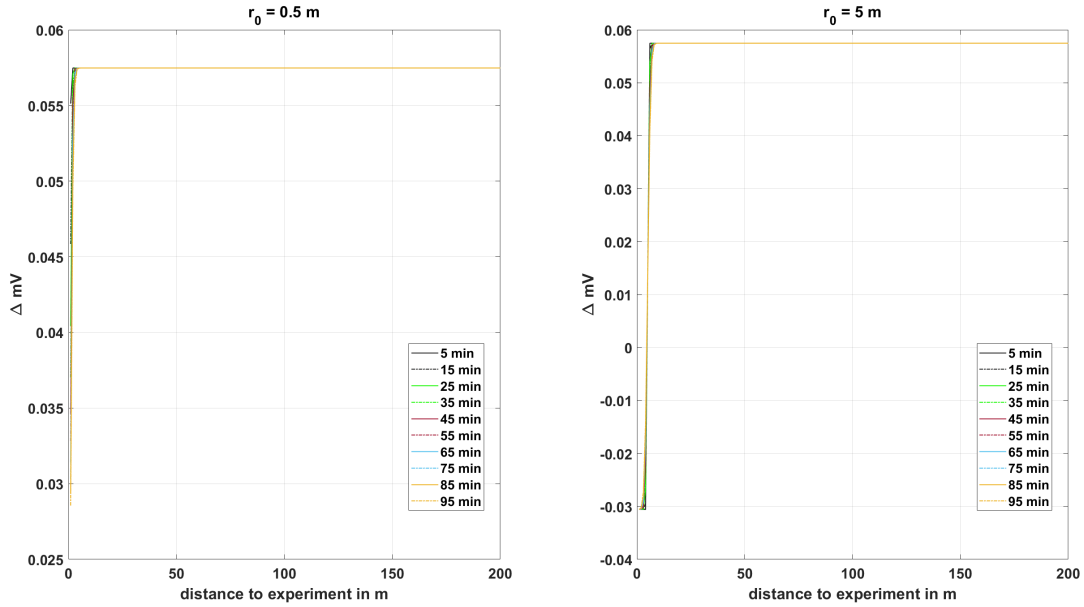

FIGURE C.1: Electrochemical potentials for $r_0 = 0.5\,m$ and $r_0 = 5\,m$. The potentials are calculated for several time steps starting by 5 minutes.